2-26-2016

Intermetallic Compounds and Their Effects on the Mechanical Performance of Micro Scale Solder Bonds

Soud F. Choudhury
University of Connecticut - Storrs, soud.choudhury@uconn.edu

Intermetallic Compounds and Their Effects on the Mechanical Performance of Micro Scale Solder Bonds

Soud F. Choudhury, Ph.D.

University of Connecticut, 2016

Interconnects in microelectronic packages and devices serve as the mechanical and electrical connections as well as thermal paths for heat dissipation. Miniaturization of electronic devices demands very high density interconnects and solder bonds with only few microns of stand-off height. Although Intermetallic compounds (IMCs) are essential to form a reliable joint, large volume ratios of IMCs can be degrading to long term reliability. At very small joints, the volume of IMCs becomes significant, and in some cases, joints may completely transform to IMCs. Furthermore, small joints experience anisotropy due to the fact that all compositions may only contain a few grains. However, very few studies have been conducted to analyze the effect of the IMCs thickness and anisotropy on the mechanical behavior of solder bonds. In this work, these effects are studied through a combination of experiments and finite element simulations. Traditionally, regular finite element (FE) modeling techniques have been used to simulate the solder joints. However, in order to evaluate joint with only few grains, a more sophisticated modeling of elastic and plastic behavior of grains is needed through crystal plasticity finite element (CPFE) modeling. In this study, CPFE is used to model all materials including solder, IMCs, and Cu in joints with different IMC thicknesses. Nanoindentation experiment on single grains of IMCs and CPFE simulation of the same were combined to obtain slip system parameters of IMCs that are necessary constants for CPFE modeling. Furthermore, electron backscatter diffraction (EBSD) analysis was used to determine the preferred grain growth orientation of Cu_6Sn_5 IMC on polycrystalline Cu substrate.

A lap-shear experiment was designed and conducted to investigate the effects of different volume fraction of IMCs on the shear behavior of micro-scale solder joints with a 50μm stand-off height. Local strain was measured using a micro-scale Digital Image Correlation (DIC) technique. This experiment was used to determine the local and global stress-strain behavior of these joints. The joints were tested to failure, and fractography was conducted to determine the failure modes and failure sites.

Comparison between experiment and modeling shows that the CPFE models are successful in capturing the local mechanical behavior of the solder bonds. CPFE models are observed to be more efficient in predicting the local plastic deformation behavior of micro scale bonds with few grains than the regular FE analysis. Simulation results show that the overall stress distribution and shear deformation changes as the IMC thickness increases. Stiffer response and higher shear yield strength are seen as the IMC thickness increases for both simulation and experiment results. Also, the stress-strain distributions observed in the CPFE analysis performed to mimic the experiment gave a clear idea on the locations of the possible failure sites. Fractography shows failure mode changing from ductile to brittle where crack propagation path is modulated by the different volume fraction of IMCs. A significant influence of Cu_3Sn/Cu_6Sn_5 interfacial morphology on the ultimate shear strength at higher volume fraction of IMC samples was observed during the lap-shear experiment where planar interfacial morphology promoted lower ultimate shear strength. The effect of different interfacial morphologies on the shear behavior was verified using CPFE simulation. Calculation of the fatigue life indicates that high volume fractions of IMCs could degrade fatigue life of the solder bonds.

Intermetallic Compounds and Their Effects on the Mechanical Performance of Micro Scale Solder Bonds

Soud F. Choudhury

B.S., Bangladesh University of Engineering and Technology, 2011

A Dissertation

Submitted in Partial Fulfillment of the
Requirements for the Degree of
Doctor of Philosophy
at the
University of Connecticut

2016

APPROVAL PAGE

Doctor of Philosophy Dissertation

Intermetallic Compounds and Their Effects on the Mechanical Performance of Micro Scale Solder Bonds

Presented by

Soud F. Choudhury

Major Advisor _____

Leila Ladani

Associate Advisor _____

Horea Ilies

Associate Advisor _____

Harris Marcus

Associate Advisor _____

Jafar Razmi

Associate Advisor _____

Jiong Tang

University of Connecticut
2016

DEDICATION

To all freedom fighters of Bangladesh Liberation war in **1971**, for their sacrifices to give me my own country, **Bangladesh**

ACKNOWLEDGMENTS

Most of all, I would like to convey sincere thanks to my advisor and mentor Prof. Leila Ladani for her valuable guidance, and her heartfelt care during my graduate studies.

I would especially like to thank my committee members for their valuable times, and suggestions. They have helped and guided me to enrich my PhD research work.

My sincere acknowledgement goes to National Science Foundation (NSF), USA for their financial support. This work has been funded from CMMI Grant No. 1416682.

I am thankful to my father Bazlul Mazid Choudhury, and my mother Munmun Choudhury for the sacrifices in life they made for me. Their life is dedicated to me. I am grateful to them.

I would like to sincerely thank my wife Tanjila Ahmed for all her patience and encouragements during my graduate study. She went through a lot to encourage and support me when I was frustrated or having troubles. Without her, it would not be possible. My forever thanks and acknowledgements go to her.

Special thanks go to my brothers, Rubaiat Islam and Saniat Islam. They have taught me to be creative, strong and grew my confidence over the years.

I am thankful to all my lab mates for their continuous support. Special thanks to Mr. Adam Wentworth and Mr. Mark Biron for providing support in fabricating test specimens.

ABBREVIATIONS AND SYMBOLS

Abbreviations:

APDL	ANSYS parametric design language
CPFEM	Crystal plasticity finite element method
CRSS	Critical resolved shear stress
CTE	Co-efficient of thermal expansion
DoE	Design of experiments
DOF	Degree of freedom
EBSD	Electron backscatter diffraction
FEA	Finite element analysis
FLI	First level interconnect
HCP	Hexagonal close packed
IMC:	Intermetallic compound
IPF	Inverse pole figure
SAC	Sn-Cu-Ag solder alloy
SDV	Solution dependent variable
SEM	Scanning electron microscopy
SLI	Second level interconnect
SLID	Solid-liquid inter diffusion
UMAT	User material subroutine

Symbols:

Scalar values are represented in italics such as *E*.Vectors are represented by bold letter such as **F.**

T	Absolute temperature
Q	Activation energy
l	Average IMC thickness
β	Correlation factor
$\mathbf{C_{ijkl}}$	Components of elastic stiffness tensor
A	Contact Area
$\boldsymbol{\tau_{crss}}$	Critical resolved shear stress
⊗	Dyadic product of two tensors or vectors
$\mathbf{F^e}$	Elastic deformation gradient
ε_e	Elastic strain
n	Hardening constant
H	Hardness
K	IMC growth rate constant
h_f	Indentation contact depth
h^0	Initial hardening modulus
$q^{\alpha\beta}$	Latent hardening constant
h_m	Maximum indentation depth
N_f	Number of cycles to failure
$\mathbf{F^p}$	Plastic deformation gradient
$\dot{\gamma}^{\alpha}$	Plastic shearing rate
$\boldsymbol{L^p}$	Plastic velocity gradient
ϑ	Poisson's ratio
ε_{cr}	Rate-dependent inelastic or creep strain
ε_p	Rate-independent inelastic strain
E_r	Reduced Young's modulus
$\widetilde{\dot{\gamma}}$	Reference shearing rate
$\boldsymbol{\varepsilon_r}$	Representative strain

τ^{α}	Resolved shear stress
τ^{s}	Saturation stress
$\boldsymbol{s^{\alpha}}$	Schmid tensor
$h^{\alpha\beta}$	Slip hardening moduli
$\Delta\varepsilon_{acc,eqv}^{cr}$	Total accumulated equivalent creep strain per cycle
$\Delta\varepsilon_{acc,eqv}^{in}$	Total accumulated equivalent inelastic strain per cycle
F	Total deformation gradient
ε	Total strain
R	Universal gas constant
S	Unloading stiffness
λ	Wavelength
Y *or* σ_y	Yield strength
E	Young's modulus

LIST OF TABLES

LIST OF FIGURES

Table of Contents

CHAPTER 1 : Introduction and Background

1.1 Background and motivation

Microelectronic packaging is a multi-disciplinary area consists of mechanical, electrical and industrial engineering, and physics. Semiconductor (silicon) die and other important components in a microelectronic system need to be connected with each other and also to the outer world. Microelectronic packaging comprises of housing and interconnections of integrated circuits (ICs) which form the inter/intra-network necessary to connect the whole microelectronic system. It also provides protection to the system from mechanical and chemical damages, heating, and electrostatic discharge. A microelectronic package contains interconnections at different levels such as *Level-0*: gate-to-gate interconnection on silicon die, *Level-1(first level interconnect-FLI)*: connection from the die to its packages, *Level-2 (second level interconnect-SLI)*: connection from packages to the printed wire board (PWB) or printed circuit board (PCB), *Level-3*: connection between PCBs. Underfill epoxy is usually used to provide stability and flexibility to the Level 1 interconnects. Often, there is a mold cage protecting the whole microelectronic system from mechanical damages and as well as

providing the heat dissipation path. Representative microelectronic packaging components are shown Figure 1-1.

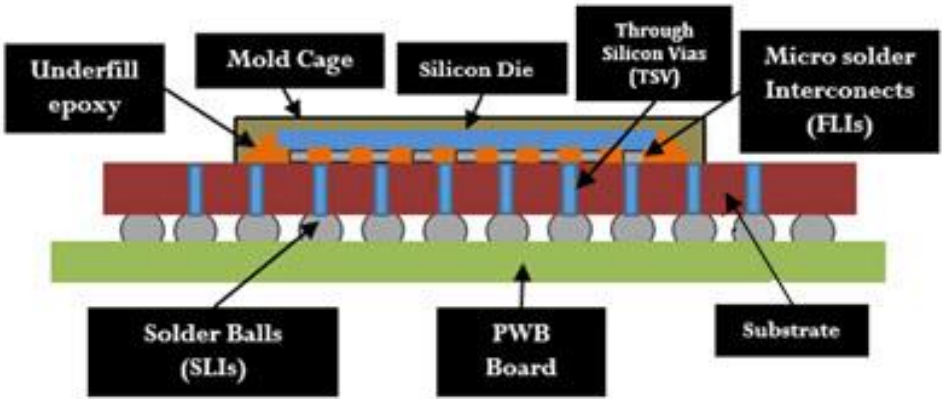

Figure 1-1: Basic components in a microelectronic packaging system

Research and development of microelectronic industries are driven by component miniaturization and by a growing demand of smaller, efficient and cheaper devices. Many small components are now packaged in a small space, and the component density is increasing day by day. Various kinds of interconnects are being used as the mechanical and electrical connections such as solder interconnects, through silicon-via (TSV), interposer, etc. Among them, solder joint is the most common and largely found interconnect type in the electronic system. With the increase in packaging density, the number of solder interconnects is increasing and the interconnect size is diminishing. Due to the scaling effect, many new problems related to the mechanical and electrical reliability are arising.

1.1.1 Solder Joints in Microelectronic Packaging

Solder alloys are most frequently used to fabricate *level 1* and *2* interconnects. Solder joints in electronic packages and devices serve as the mechanical and electrical connections as well as

thermal paths for heat dissipation. With the continuous progress in microelectronic packaging, solder alloys have been serving as a primary material for creating interconnections. Traditionally, eutectic or near eutectic tin-lead (Sn-Pb) alloys have been widely used as solder material in microelectronics fabrication [1,2]. These Sn-Pb alloys were very popular due to their lower melting temperature of 183°C, superior wettability, excellent ductility, good reliability, and lastly compatibility with different substrates [3]. However, due to the toxic and harmful effect of Pb on human health, there was an urgency to ban usage of Pb in electronics. The Restriction of Hazardous Substrate Directive (RoHS) specifically bans usage of Pb from electrical and electronic components manufactured after July 1, 2006, which forcefully shifted the industry and research community's focus towards developing environmental friendly electronics with Pb-free solders. To find compatible candidates to replace Sn-Pb solder alloys, the following characteristics have been taken into consideration [4]:

- melting temperature similar to eutectic Sn-Pb for a similar reflow profile
- satisfactory wettability for the good metallization process
- better electrical properties for transmitting electrical signals
- strong and reliable mechanical properties for good fatigue resistance and reliability
- cheap and easier manufacturability

In recent years, researchers have proposed binary, ternary, even quaternary solder alloys to replace Sn-Pb solders in the microelectronic industry [5]. They have suggested Sn-rich binary alloys such as Sn-Cu, Sn-Ag, Sn-Zn, Sn-Bi, Sn-In system; the ternary system such as Sn-Ag-Cu; and even higher order alloys [5]. A small amount of dopant has also been utilized to achieve the desired electrical and mechanical properties of the solder alloys. The proposed

doping element candidates include Bi, Ni, Co, Zn, La, Mn, Ce, Ti, In, B, etc. For example, an addition of Ni in Sn-Ag-Cu solder alloy system has been reported to produce finer solder microstructure; thus improving the mechanical properties [6]. In addition, doping the solder alloy with rare earth (RE) elements tend to enhance wettability, improve ductility, and refine microstructure of SAC alloy system [7,8]. However, still microelectronic industries are using binary and/or ternary solder alloys in their components due to the high cost of rare earth elements.

1.1.2 Pb-free solder alloys

Among different solder alloys, Sn-3.5Ag, Sn-0.7Cu, and eutectic or near eutectic Sn-Cu-Ag (SAC) alloys are the leading candidates due to their high compatibility with current fabrication processes and comparable properties with Sn-Pb solders. A market survey of 2006, published by European lead-free soldering network reported that the larger part of the electronic products industries are using SAC and Sn-3.5Ag solder alloys in their systems (Figure 1-2). A variety of SAC alloys with different composition have been proposed in recent years such as SAC105 (98.5Sn-1.0Ag-0.5Cu), SAC205 (97.5Sn-2.0Ag-0.5Cu), SAC305 (96.5Sn-3.0Ag-0.5Cu), and SAC405 (95.5Sn-4.0Ag-0.5Cu), known as the SACN05 series; SAC387 (95.5Sn-3.8Ag-0.7Cu), SAC396 (95.5Sn-3.9Ag-0.6Cu), and SAC357 (95.2Sn-3.5Ag-0.7Cu) and so on. Overall, different solder alloys have been proposed over the time to concentrate on some of the specific properties needed in the respective applications.

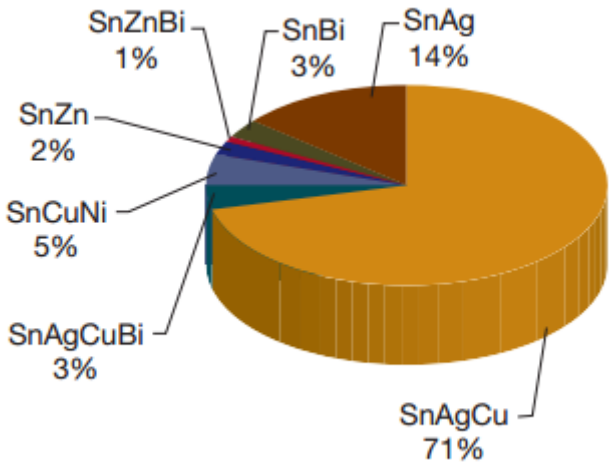

Figure 1-2: Lead-free solder alloys status survey, 2006 [9]

1.1.3 Intermetallics (IMCs) in Pb-free solder alloys

SA/SAC candidates are mostly Sn-rich alloys with slight additions of Ag and/or Cu. The bulk of the Sn-based alloy containing Ag or Cu consists of Sn-rich dendrites surrounded by a eutectic mixture of Cu_6Sn_5, Cu_3Sn and Ag_3Sn. These compounds are called Intermetallic compounds (IMCs). Figure 1-3 shows the IMCs formed in a typical solder joint. The formation of IMCs can be described from the Sn-rich part of Sn-Ag-Cu phase diagram provided in Figure 1-4.

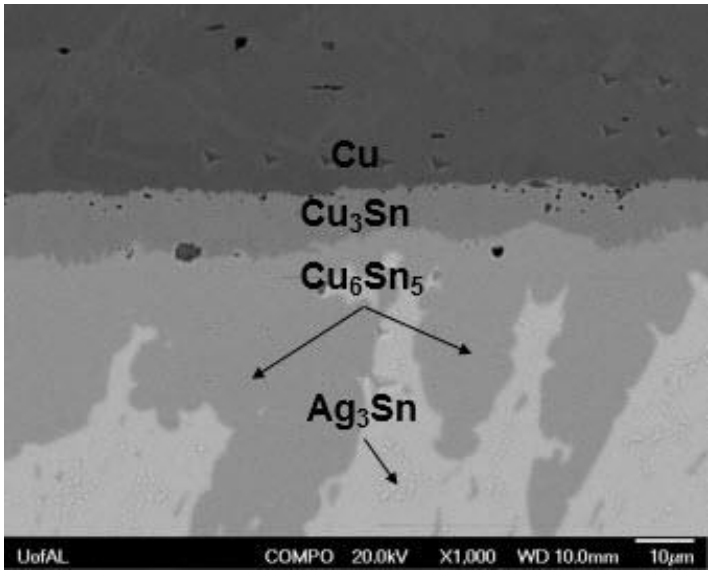

Figure 1-3: IMCs formed in a typical solder joint

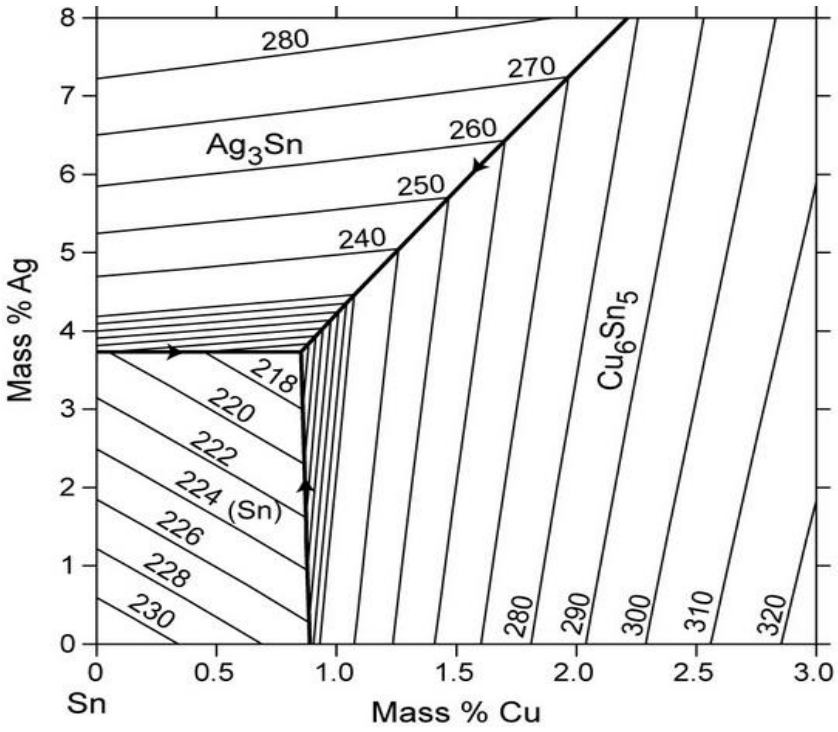

Figure 1-4: Sn rich part of Sn-Ag-Cu phase diagram [10]

Ag_3Sn IMC forms when there are substantial amount of Ag content in the alloy and Sn reacts with Ag at a higher temperature. Sn and Cu reacts with each other and forms Cu_6Sn_5. Cu_6Sn_5 is usually observed in between solder/substrate interface when the substrate is Cu. Cu_3Sn will not form at the eutectic point except the Cu content is sufficient for the formation of Cu_3Sn at higher temperature, so in bulk specimen, Cu_3Sn is not presented. However, when Cu_6Sn_5 is formed in solder/substrate interface, due to the less supply of Sn towards Cu substrate, Cu_6Sn_5 reacts with Cu and forms Cu_3Sn in substrate/Cu_6Sn_5 interface.

IMC layer (Cu_6Sn_5 and/or Cu_3Sn) is an essential component of a good metallurgical bond. However, the mechanical and physical properties of IMC layers significantly differ from the solder and substrate. Excessive IMC layers can lower the reliability of solder joints due to their hard and brittle nature. Continuous miniaturization of packages and joints has increased the volume fraction of IMCs to such an extent where smaller joints could be completely composed of IMCs (Figure 1-5).

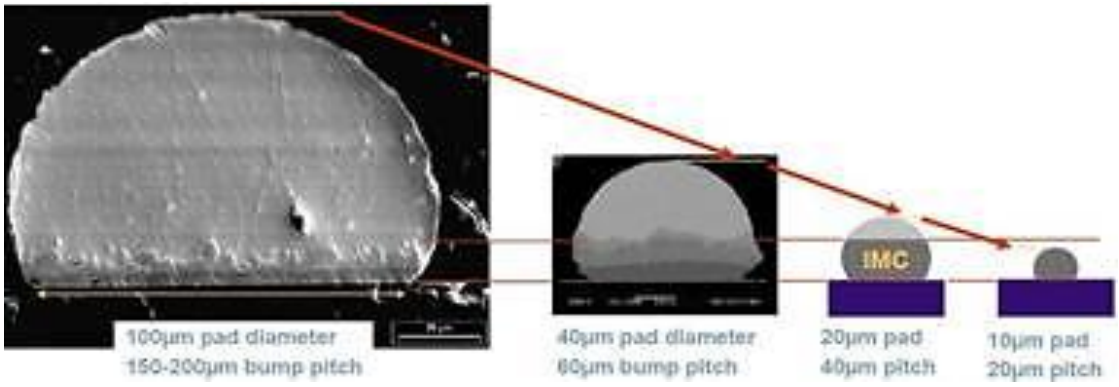

Figure 1-5: Volume fraction of IMCs increases as solder joint size decreases [4]

It was shown by Islam and Sharif that the mean thickness of IMC layers in smaller joints is much larger than that of the bigger joints [11]. Abdelhadi et al. [12] investigated solder joints with thicknesses of 15-25 µm and observed that with longer soldering time and higher temperature, solder joints transform completely into IMCs. Although the time and temperature used in their experiment are not conventional in the electronic industry, it is suspected that if the joint thickness is reduced to below 10 µm, it is very likely that the whole joint will transform to IMCs. It was hypothesized by Chawla et al. [13] that solder joint strength was controlled by bulk solder strength up to a certain strain rate and then by IMC strength at higher strain rates (Figure 1-6). This has been verified over a wide range of strain rates (10^{-3} -12 s^{-1}) [14]. This behavior applies when IMC layer thickness is less than 15µm. With higher IMC layer thicknesses, solder strength is completely controlled by the IMC layer [14].

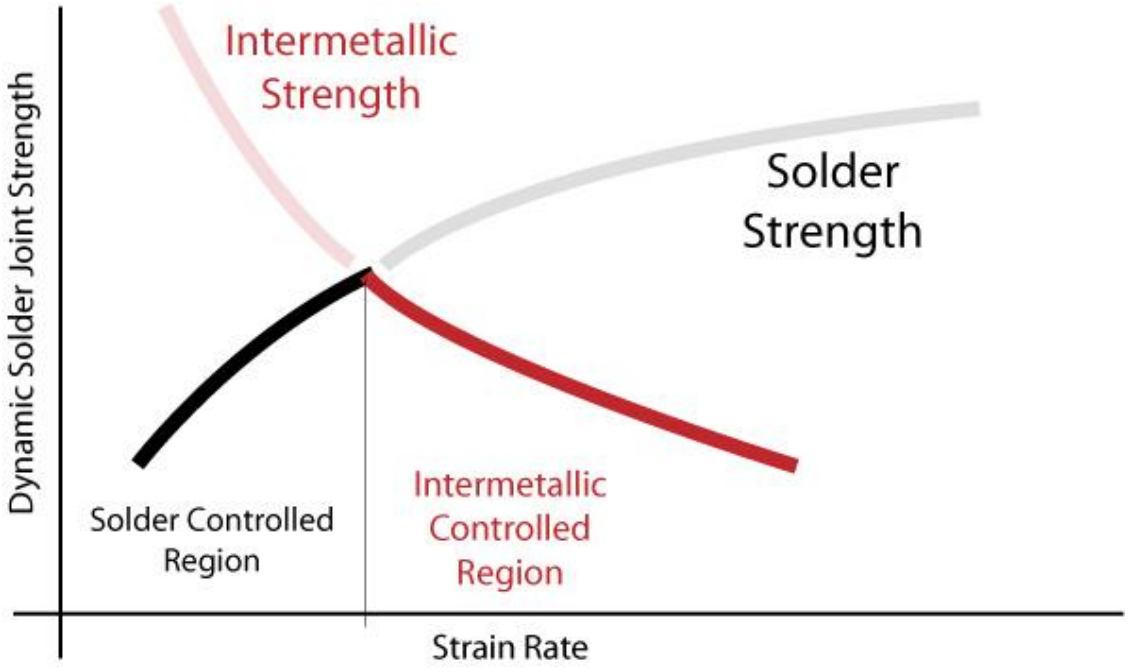

Figure 1-6: Dynamic solder joint strength as a function of strain rate (Redrawn) [13]

1.1.4 Cu_6Sn_5 IMC

Cu_6Sn_5 is the main effective IMC found in almost all solder/substrate system and it also possesses the maximum volume fraction compared to Cu_3Sn and Ag_3Sn in a solder joint. Thus, it can be assumed that Cu_6Sn_5 is the main compound that controls the effect of IMCs on the mechanical behavior of solder joint.

1.1.4.1 Crystal structure of Cu_6Sn_5 IMC

Two different crystal structures are reported for Cu_6Sn_5 in literature: hexagonal and monoclinic. According to the phase diagram of Cu-Sn, allotropic transformation occurs at 187.6^0 C where the monoclinic crystal structure transforms completely into a hexagonal structure [15].

η- Cu_6Sn_5 (Hexagonal) -> ή- Cu_6Sn_5 (Monoclinic) at 187.6°C

However, researchers suggested that during soldering and subsequent cooling, there is not sufficient time for the transformation into the low-temperature monoclinic structure, and Cu_6Sn_5 remains as a metastable high-temperature hexagonal phase [16,17]. Due to the strain constraints, transformation does not occur within a reasonable amount of time if the temperature is near room temperature [31]. Also, addition of alloying elements such as Ni/Au/Ag may stabilize the crystal structure and it remains hexagonal at room temperature [18].

HCP crystal structure generally contains 3 slip modes – basal {0001} <11$\bar{2}$0>, prismatic {10$\bar{1}$0} <11$\bar{2}$0>, and pyramidal <a> {10$\bar{1}$1} <11$\bar{2}$0> which provides deformation to <a> direction only. Furthermore, 1st order pyramidal <c+a> {10$\bar{1}$1} <11$\bar{2}$3> and 2nd order

pyramidal <c+a> {$10\bar{2}2$} <$11\bar{2}3$> slip modes along with deformation twinning (DT) provide an additional mechanism to accommodate *c-axis* deformation (Figure 1-7) [19].

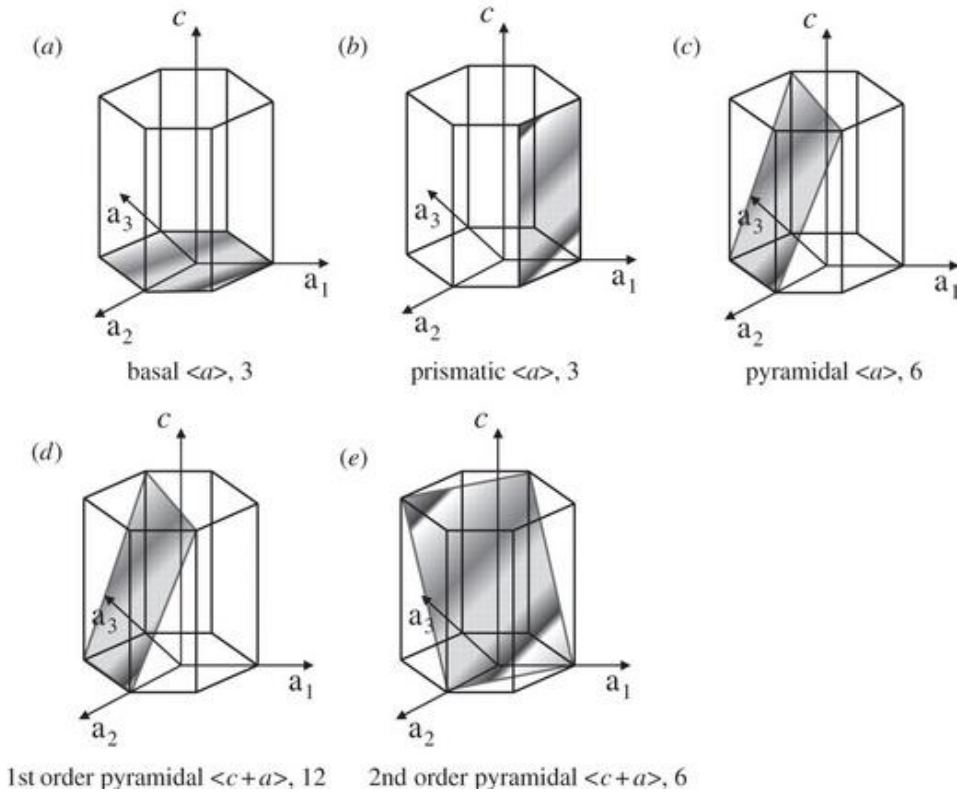

Figure 1-7: Different slip planes and directions in Cu_6Sn_5 crystal [20]

1.1.4.2 Anisotropy of Cu_6Sn_5 IMC

η- Cu_6Sn_5 has a hexagonal crystal structure, with a unit cell parameters of c= 5.103 and a= 4.197 [21]. With c/a ratio of 1.215, it has been reported previously that Cu_6Sn_5 shows mechanical anisotropy [16,22]. Due to the differences in inter-plane distance between crystallographic basal, prismatic, and pyramidal planes; and also, for the differences in atomic densities in between planes, hardness and elastic modulus tend to show anisotropy [16,18,22]. Song et al. [16], Jiang et al. [22]and Mu et al. [18] researched the elastic modulus and hardness

anisotropic effects of Cu_6Sn_5 IMC. They observed changes in mechanical properties with the crystallographic orientation. They examined the mechanical properties of grains with the *c-axis* oriented perpendicular and parallel to the loading direction and observed higher elastic properties when the *c-axis* was parallel to the loading direction. Further theoretical studies conducted by Zhou et al. [23] using monoclinic Cu_6Sn_5 also showed the directional dependency of the elastic modulus of Cu_6Sn_5. Yang et al. [24] observed no anisotropic effect on the mechanical properties of Cu_6Sn_5 as there was no orientation dependency observed in their experiment. Research on the mechanical anisotropy of Cu_6Sn_5 IMC is still in progress.

The elastic and plastic properties of Cu_6Sn_5 IMC cannot be determined properly with typical mechanical tests because bulk IMCs fabricated by casting and annealing contain porosities and/or oxides [25]. Furthermore, grain size and crystallographic orientation may differ in bulk Cu_6Sn_5 IMC than Cu_6Sn_5 IMC formed in the solder joint. Some researchers have reported the mechanical characterization of Cu_6Sn_5; however the properties reported by these studies vary over a large range. Discrepancies among published values can be primarily attributed to the differences in sample preparation and experimental techniques. The findings from the literature are summarized in Table 1-1.

Table 1-1: Summary of literature on elastic-plastic properties of Cu_6Sn_5 IMC

Elastic properties (GPa) (E= Young's modulus H= Hardness)	**Plastic properties (Y= Yield strength n= Hardening exp.)**	**Sample preparation process**	**Testing process**	**Source**
E= 130± 9 (at 25°C) H= 6.67± .43 (at 25°C)	-----	Sn-3Ag-0.5Cu, BGA reflowed at 245°C	Nanoindentation	Marques et al. (2013) [24]
E=106.25 ± 2.86 (⊥to c-axis) 120.75±2.12 (∥ to c-axis) H=5.74 ± 0.15 (⊥to c-axis) 6.22±0.26 (∥ to c-axis)	----- -----	Sn-4Cu, directionally solidified at 440°C	Nanoindentation	Mu et al. (2012) [18]
E=114.7 ± 2.8 (⊥to c-axis) 123±2.5 (∥ to c-axis) H=6.42 ± 0.05 (⊥to c-axis) 6.1±0.3 (∥ to c-axis)	----- -----	Sn-3.9Ag-0.7Cu/Cu Joint annealed at 300°C	Micro Pillar Compression Test, Nanoindentation	Jiang et al. (2012) [22]
E= 127 ± 4.841 [Top] 114 ± 5.189 [Lateral] H= 6.47 ± 0.156 [Top] 6.562 ± 0.141 [Lateral]	Y= 1850.6±124 MPa n= 0.105±0.01	Sn-1.0Ag-0.5Cu, current stressed, reflowed at 400°C	Nanoindentation	Song et al. (2012) [16]
E= 116.89± 2.04 [Top] 118.97 ± 1.93 [Lateral] H= 6.35 ± 0.20 [Top] 6.45 ± 0.14 [Lateral]	-----	Annealing Sn-Cu diffusion couples	Nanoindentation	Yang et al. (2007) [24]
E= 125 ± 6.8 H= 6.10 ± 0.53	-----	Sn-3.5Ag joint annealed at 240° C	Nanoindentation	Jang et al. (2004) [26]
E= 114.9 ± 1.5 H= 6.27 ± 0.30	-----	Bulk specimen, Casting	Nanoindentation	Jang et al. (2004) [26]
E= 119 ± 6 H= 6.5 ± 0.3	-----	Sn-4Ag-.5Cu joint, solid state aging of diffusion couple	Nanoindentation	Chromik et al. (2004) [27]
E= 112.3±5.0 H= 6.38±.21	Y= 2009±63 MPa n= 0	Sn-3.5Ag/Cu joint annealed at 240°C	Nanoindentation	Deng et al. (2004) [28]

Clearly, to evaluate the reliability of solder joints, accurate prediction of the effective macroscopic material behavior, understanding of the localized damage mechanisms, and local

(nano- and/or micro scale) mechanical properties of the Cu_6Sn_5 IMC in the solder joint are necessary.

1.1.5 IMC Growth Behavior

After the reflow process, a small scale solder joint contains a large volume fraction of IMCs. However, not only IMCs grow during the reflow process, the IMC volume fraction tends to develop with the service application of the solder joints too. Due to high-temperature, continuous applications such as electronic data servers running continuously and dissipating heat, solid-state aging occurs, and IMCs grow with volume diffusion mechanism. On the other hand, electronics in automotive, aerospace and military applications have to go through a large number of cyclic temperature loading. During the cyclic temperature loading, IMCs tend to grow slower than the isothermal aging condition [29]. Overall, it is worthy to note that volume fraction of IMCs in solder joints continue to increase after the fabrication process. These phenomena highly raise the necessity to study the growth behavior of IMCs in the solder joint.

IMC growth during the reflow process, cyclic temperature loading, and isothermal aging has been studied by several researchers. From the literature review, it was clear that the growth behavior trend was similar for all different solder alloys irrespective of their different compositions, although the growth rate was different for different compositions [30]. Overall, IMC thickness increases with the increase in reflow time and temperature [31–34], and aging time and temperature [12,35,36]. IMC thickness growth is also largely affected by the cooling rate where slow cooling in furnace provides larger IMC thickness than the faster cooling by water quenching [37].

1.1.6 Effect of IMCs on the Mechanical Strength

Intrinsic mechanical properties of IMCs are completely different than bulk solder alloy. Bulk solder alloys are known for their ductility and flow behavior, where IMCs are highly recognized as hard and brittle materials. When solder joint has a major volume fraction of bulk soft solder, the material behavior of the joint is observed to be fully controlled by bulk solder properties. However, the joint behavior becomes quite complex when a significant presence of IMCs is witnessed.

1.1.6.1 Shear Behavior

The effect of IMC thickness on the shear behavior of the solder joints is explored in some studies [31,32,38–46]. Liu et al. [32] investigated the effect of different IMC thickness that were achieved during multiple reflows on the shear performance of the solder joint. IMC growth and thickness was found to have an insignificant effect on the shear strength of SnAgCu solder joints in their study. However, Bhat et al. [44] found an increase in shear strength of SAC387/Cu joint with the increase in reflow temperature that was attributed to the increase in thickness of Cu_6Sn_5 and Ag_3Sn IMC phases at higher reflow temperatures. On the contrary, Deng et al. [40] observed a decrease in shear strength with the increase in IMC thickness after the reflow and thermal aging processes. However, the decrease in shear strength during thermal aging was attributed to solder microstructure coarsening. The failure surface showed a ductile fracture in all test cases which suggested that the failure was occurring at the bulk solder region, and the shear strength was not sensitive to the thickness and morphology of IMCs. Lee et al. [43] also investigated the effect of solder microstructure coarsening, Ni addition, and IMC

growth during reflow and thermal aging process on the shear behavior of the solder joint. They observed a decrease in shear strength with the increase in reflow and thermal aging time.

All these analyses were conducted on solder joints with the thickness range of 0.20 mm - 2 mm [32,40,43] and the joints had a lower volume fraction of IMCs. Recently, a study conducted by Chen et al. [41] showed a major influence of IMC presence and thickness on the shear strength. They conducted a single ball shear test on thermally aged micro scale solder bumps with about 35 µm thickness that had a range of different IMC thicknesses due to different aging times. Shear strength was observed to decrease with the increase in IMC thickness. They also observed the failure mode transforming from ductile mode to the quasi-brittle mode with the increasing aging times.

Joint thickness also showed a major impact on the shear strength and failure mode of the solder joint [42,47]. It was found that decrease in joint thickness results in a decrease in shear strength [42]. This trend was associated with the presence of Cu_6Sn_5 precipitates in the thicker joint, which was absent in the thinner joints [42]. Some limited studies used modeling to evaluate the impact of IMC thickness on the mechanical behavior of solder joint [40,48]. However, due to differences in intrinsic material behavior from the bulk material behavior, these models were not able to successfully predict the actual behavior of small-scale joints.

1.1.6.2 Thermo-mechanical Fatigue Behavior

Numerous studies were conducted to understand the effects of IMCs on the thermo-mechanical fatigue behavior which is one of the most important failure mechanisms for both FLIs and SLIs. Both computational and experimental investigations have been conducted on a large scale.

Several researchers have developed thermo-mechanical fatigue life model for solder joints of SLIs that has a standoff height in the range of 100-500µm [49–54]. Solder joint of this height range contains a large volume fraction of bulk solder alloys. At this scale, not considering the IMCs in the model may not affect the fatigue life prediction as IMCs have negligible volume fraction compared to bulk solder. However, micro-bumps in between two silicon substrate in 3D ICs are of 10-60µm standoff height that contain a large volume of IMCs [55]. Model without the inclusion of IMCs may not be able to predict the fatigue life of micro-bumps properly. The effect of IMC compound growth on the thermo-mechanical fatigue reliability of the microelectronic packaging has been investigated computationally by some scholars [56–61]. Chiou et al. [59] presented a finite element based fatigue life prediction model of Sn-Pb and Sn-3.5Ag alloy solder bumps with a height of 100µm and a pitch of 360µm. They reported a decrease in the fatigue life of the solder bumps with the increase of IMC thickness. The trend was more noticeable in Sn-Pb alloy rather than Sn-3.5Ag alloy. Moreover, they concluded that the influence of IMC thickness on the fatigue life prediction of lead-free solder joints was negligible. Changes in IMC thickness considered by the authors was not significant compared to the higher volume fraction of bulk solder in the model. However, recently, Chen et al. [57] reported the opposite phenomenon where they observed an increase in the fatigue life of the micro solder bump with the increase in IMC thickness. They analyzed 22 µm bump with different thickness of $NiSn_4$ IMC and observed that the effect of IMC inclusion is negligible for thinner IMC layers, but fatigue life tends to increase dramatically with thicker IMC layers. They hypothesized the case was due to the hard nature of the IMC materials. From the literature survey, conflicting results have been reported and still there are confusions on the effects of IMC compounds on the thermo-mechanical fatigue reliability of micro scale solder joint.

It can be easily understood that the volume fraction of the IMCs in a bond has a great impact on the fatigue reliability. However, very few studies were conducted and reported in the literature where small micro-bumps were taken into consideration. Furthermore, the effects of IMCs on the micro-bump's thermo-mechanical fatigue behavior are not studied although the larger volume fraction of IMCs in micro-bumps is considered to have a greater impact on the fatigue reliability.

1.1.7 Computational Modeling of Micro-Mechanical Behavior of Solder

Computational modeling of the micro-mechanical behavior of the solder joint is one of the most common analyzing techniques utilized globally by the industries and academia. However, it is a challenging task to capture the anisotropic micro-mechanical behavior precisely with traditional finite element (FE) modeling. Conventionally, researchers utilize FE modeling to capture the mechanical behavior of solder bonds, and it is successful when the solder bond size scale is large [42,49,52,62,63]. At a larger scale, the anisotropic mechanical effect tends to diminish, and materials in solder bond demonstrate the isotropic behavior. Thus, FE modeling application is observed to be effective at the larger scale. However, smaller solder joints have few number of grains, and anisotropy due to the large microstructure and crystallographic orientation comes into consideration. In this condition, traditional FE modeling becomes less effective in portraying the overall micro-mechanical behavior of the miniaturized solder joints. Literature survey provides many examples where generated FE model fails to provide an accurate prediction of the micro-mechanical performance [28,64–66]. As the deformation mechanisms are modulated by crystallographic slip behaviors in these miniaturized solder joints, to understand the behavior completely and to optimally design such microstructures

with anisotropy, it is important to develop computational tools that assist their detailed understanding. Researchers have used the crystal plasticity finite element (CPFE) method to model the deformation mechanism of single crystals [67–70]. The CPFE method takes into account the effects of anisotropy and slip system behavior in modeling materials. Deformation of a slip system of a single crystal largely rests on the slip parameters such as critical resolved shear stress (CRSS), initial hardening modulus, and saturation stress (Stage I stress when large plastic flow occurs). CPFE modeling needs these crystallographic parameters to model the anisotropic elastic-plastic behavior of a single crystal. These crystallographic parameters are available for Sn in the literature [71,72]. However, no efforts have been made to capture the slip parameters of Cu_6Sn_5 or any IMC experimentally or analytically because of the difficulties of using conventional mechanical testing methods to measure the slip parameters of HCP single crystals. Due to a wide range of CRSS values, it becomes difficult to isolate a specific slip system in testing without activating the other slip systems. Very few studies used CPFE approach in modeling the anisotropy effect in solder joints [71–73]. Darbandi et al. [71] have utilized Sn crystal plasticity material parameters to observe the deformation of lead-free solder joints' microstructure, but they did not consider IMCs in their model. If the crystallographic slip parameters of IMCs can be established, then modeling the solder joint mechanical behavior with CPFE modeling can be a very promising approach. Details on the crystal plasticity theory has been provided in Chapter 3.

1.2 Objectives

Based on the literature review conducted, several critical issues are observed in the area of Pb-free solder bonds that are still needed to be addressed. Thus, the primary objectives of this research work are set to:

1. Characterization of microstructural and mechanical anisotropy of single grain Cu_6Sn_5 IMC.
    a. Investigate preferred grain growth orientation of Cu_6Sn_5 IMC.
    b. Determination of single grain elastic-plastic properties such as Young's modulus, hardness, yield strength and strain hardening exponent, and correlate them with the crystallographic orientation to investigate the anisotropic effects.
2. Develop CPFE model to capture the micro-mechanical anisotropic behavior of solder bonds.
    a. Predict the crystallographic slip parameters of Cu_6Sn_5 IMC.
    b. Develop a complete CPFE model with the substrate, solder, and IMCs to capture the overall micro-mechanical anisotropic behavior of solder bonds.
3. Experimentally investigate the effects of high volume fraction of IMCs on the local shear behavior of micro-scale solder bonds.
    a. Fabricate solder bonds with 50 μm joint thickness and investigate the shear stress-strain behavior with different IMC volume fraction.
    b. Conduct CPFE computational study to investigate IMC thickness effects on the local shear behavior of solder bonds.
4. Computationally investigate the effects of IMCs on the thermo-mechanical fatigue reliability of micro scale solder bonds.

1.3 Dissertation Organization

This dissertation is organized based on the articles that have been already published or under review at this time.

In Chapter 2, microstructural and anisotropic mechanical characterization were discussed for IMCs found in the solder joints. Especially, the mechanical anisotropy of single grain Cu_6Sn_5 was extensively investigated and discussed.

Chapter 3 focused on a novel combined experiment and computational approach in predicting the crystallographic slip parameters of Cu_6Sn_5 IMC. The chapter discusses the method to use nanoindentation experiments combined with the CPFE modeling to acquire the slip parameters for three major slip systems of Cu_6Sn_5, which are not available in the literature.

Chapter 4 presents a fully developed CPFE model to capture the micro-mechanics of major materials found in solder joints such as Cu substrate, bulk solder and Cu_6Sn_5 IMC. The developed model was validated with the experimental results found in literature and utilized to investigate the effect of IMC presence on the shear behavior of micro-scale solder bonds. The findings in this computational investigation were comprehensively discussed in this chapter.

Chapter 5 discusses the single lap-shear experiments used to investigate the effect of IMC thickness variation on the local shear stress-strain behavior of micro-scale bonds of 50 μm stand-off height. It describes the experimental setup and the technique developed to measure the local shear displacements of the solder bonds. The tests were conducted on specimens with different IMC thickness. Overall, the chapter provides an idea on how the shear strength and failure strain change with the change in IMC thickness.

The effect of IMC thickness on the thermo-mechanical fatigue life of micro solder bonds was investigated computationally using FE analysis. Chapter 6 presents the results and recommendations on how the presence of IMCs can largely deviate the overall thermo-mechanical fatigue behavior of solder bonds.

The last chapter, Chapter 7, summarizes the primary results, contributions of the studies conducted and as well as the recommendations for the future directions of this research.

CHAPTER 2 : Microstructural and Micro-mechanical Characterization of Cu_6Sn_5 IMC: Nanoindentation & EBSD Analysis

2.1 Introduction

Miniaturized solder joints may contain very few grains of Cu_6Sn_5 which could introduce the anisotropic behavior in system. On the other hand, assessment on microstructure of IMCs found in solder joint is also important. In this study, two characterization technique, scanning electron microscopy (SEM) and Electron backscatter diffraction (EBSD) analysis have been used to investigate the microstructure of the IMCs in the solder joint. Grain growth texture was of particular interest owing to the anisotropic property variation observed in Cu_6Sn_5 IMC. Experiments have been conducted to understand if there was any preferred grain growth orientation of Cu_6Sn_5 IMC.

Elastic-plastic properties of single grain Cu_6Sn_5 IMC were investigated in this section through nanoindentation. Elastic properties such as elastic modulus and hardness were determined from

the nanoindentation load-depth curve. The reverse analysis model described by Dao et al. [74] was used to extract plastic properties such as yield strength and strain hardening exponent from nanoindentation data. Care was taken to achieve indentation of single grains with sufficient accuracy and repeatability. Electron backscatter diffraction (EBSD) mapping was used to determine the orientation of Cu_6Sn_5 grains and to relate the orientation with the load-depth curve results of nanoindentation and the corresponding elastic-plastic properties.

2.1.1 Scanning Electron Microscopy (SEM)

The scanning electron microscope (SEM) uses a focused high-energy electron beam to produce a variety of signals at the surface of solid specimen or target sample. These signals are then collected by the detectors and used to analyze for imaging, quantitative and semi-quantitative information of the target sample.

2.1.1.1 Theory

Electron source or gun produces high energy electron beam which goes through several stages inside the beam chamber. The incident electron beam energy can be controlled by regulating the beam current, voltage, etc. Accelerated electrons can pass through the sample without interaction, or undergo elastic scattering, and can also be inelastically scattered when it hits the surface of the target sample. The inelastically scattered beams are then collected by the corresponding detectors and analyzed. Typical signals used for imaging include secondary electrons (SE), backscattered electrons (BSE), diffracted backscatter electron (EBSD), characteristic X-ray signals such as X-ray diffraction (XRD) and X-ray fluorescence (Figure 2-1).

The incident beam raster through the target surface continuously, and generates the characteristic inelastic beams for every point. When an inelastic beam is generated, specific detector receives a certain signal which is transmitted to the computer system for analysis. The received signal has its characteristics that can then be processed to create images or to acquire quantitative (compositional) and semi-quantitative (topological) information.

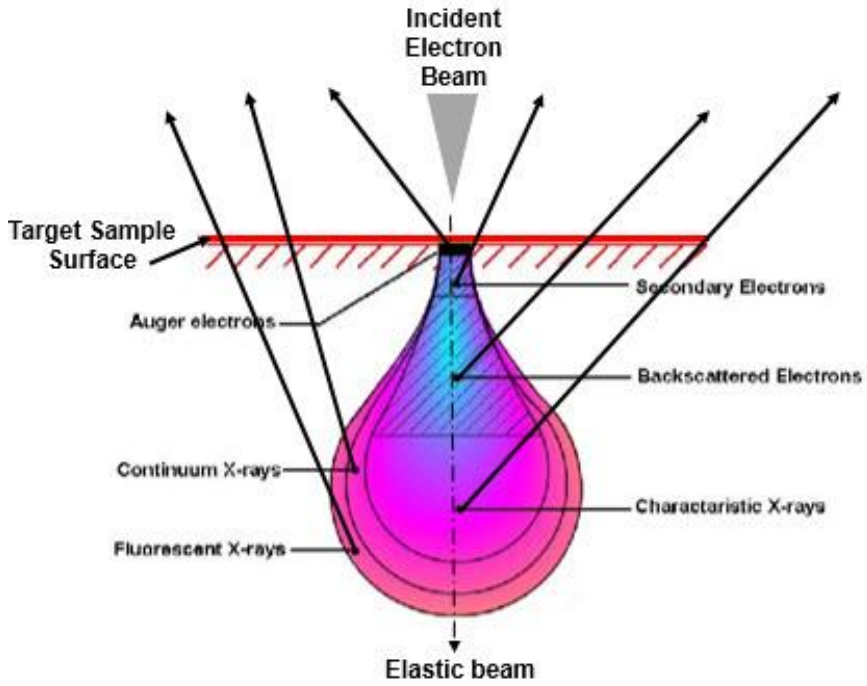

Figure 2-1: Incident electron beam and sample interaction diagram [75]

2.1.2 Electron Backscatter Diffraction (EBSD)

Electron backscatter diffraction (EBSD) is an effective and mostly used microstructural-crystallographic technique to understand the grain properties; especially grain orientation. It can also provide information such as grain size, misorientation, preferred grain growth orientation, grain boundary information, slip system activity, phase distribution and many more.

2.1.2.1 Theory

The EBSD system is also known as backscatter kikuchi diffraction (BKD) as this technique utilizes Kikuchi patterns to determine grain properties. In 1928, Nishikawa and Kikuchi [76] first observed an electron diffraction pattern containing a band feature, and regarded the formation of the pattern as the inelastic and elastic scattering of electrons within the sample. The mechanism by which the diffraction patterns are formed is complex. However, to understand the principal features, knowledge regarding Bragg's principle is important.

Bragg's diffraction principle was first proposed by William Lawrence Bragg and William Henry Bragg in 1914 [77]. They observed that with a specific wavelength and incident angle, if an electron hits an atom and scatters as a constructive interference, then a characteristic diffraction pattern is formed. For a crystalline solid, the electrons are scattered from lattice planes separated by the inter-planar distance, *d.* The path difference between two diffracted waves undergoing interference is given by $2dsin\theta$, where θ is the scattering angle. This leads to Bragg's condition that depends on θ for the condition of constructive interference which is,

$$2dsin\theta = n\lambda \quad \textbf{(2.1)}$$

Here, *n* is positive integer, λ is incident wavelength. A diagram showing the Bragg's law representation is given in Figure 2-2. A pattern of diffraction is obtained by measuring the intensity of scattered waves as a function of the scattering angle. Very strong intensities known as Bragg peaks are obtained in the diffraction pattern at the points where the scattering angles satisfy Bragg condition.

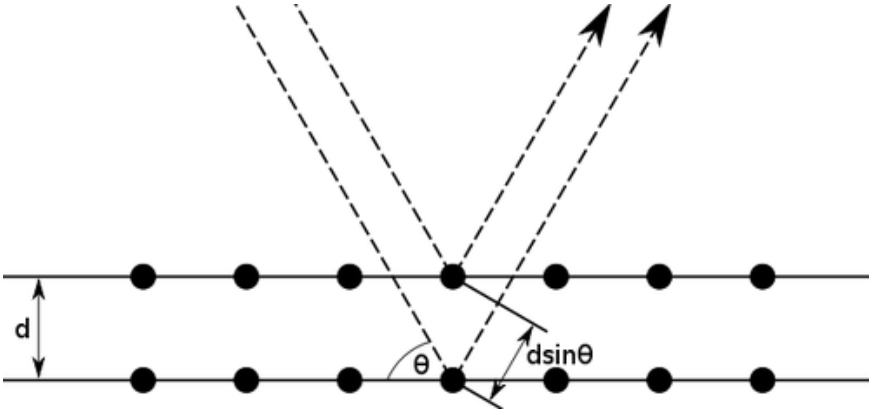

Figure 2-2: Representative diagram of Bragg's law

The locations of the array of atoms in a crystal of a material are commonly known. When electron hits the atoms of the crystal, it inelastically scatters a fraction of the electrons with a small loss of energy to form a divergent source of electrons close to the surface of the sample. The electrons that are diffracted form a set of paired large angle cones that correspond to each diffracting plane (Figure 2-3-a). The regions of enhanced electron intensity between the cones produce the characteristic Kikuchi bands or patterns of the electron backscatter diffraction pattern when it is imaged on the fluorescent screen (Figure 2-3-a).

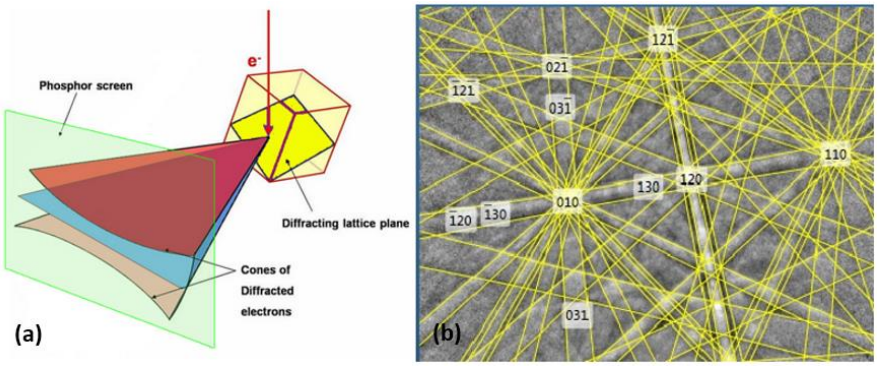

Figure 2-3:(a) Schematic showing the generation of kikuchi patterns [78], (b) Generated actual kikuchi pattern for a particular Cu_6Sn_5 crystal

The formed kikuchi pattern or electron backscatter diffraction pattern (EBSP) can be indexed and compared with the previously known patterns to predict possible information regarding the crystalline structure, atomic plane location and crystallographic orientation (Figure 2-3-b). In modern days, powerful computation makes it possible to get accurate results from EBSP.

2.1.2.2 EBSD technique

To determine the microstructural properties using EBSD technique, sample preparation is very important. To create a clear kikuchi pattern, the surface of the region of interest needs to be scratch and impurities free. The sample is set in a tilting position to create a larger angle (~70°) about the normal electron beam incidence to optimize both the contrast in the diffraction pattern and the fraction of the electrons scattered from the sample [113]. A brief flow diagram of the EBSD imaging technique has been provided in Figure 2-4. When the electrons from the electron gun hit the tilted sample, the inelastically scattered electrons can be elastically scattered when the Bragg's condition is met for some crystallographic planes and created kikuchi bands on the EBSP detector. The width of the Kikuchi bands corresponds to the *d*-spacing of a particular crystallographic plane via the Bragg's law. The pattern is then recorded by charge-coupled device (CCD) camera and is sent to a computer program. This program performs indexation that follows three processing steps: 1) diffraction pattern image processing and detection of the bands, 2) zone axes indexing, and 3) crystal orientation determination based on the inter-planar and inter-zone angles [79]. In the present, most commonly used algorithm to analyze the kikuchi pattern is Hough transformation [80].

When the bands are detected, the widths and the angles between the bands (at least three bands are required) can thus be measured and compared with standard sets of inter-zone axes angles

derived from the known crystal structure and its lattice parameters. All possible combinations of zone axis indices are examined by the program. A possible solution is taken to be the one that appears most frequently in the solution sets and matches between the measured and theoretical calculated inter-zone axes angles [79].

Crystallographic orientation information is provided by the Euler angle for individual grains. The analyzed data can be used further to generate other microstructural information such as grain size, grain boundary misorientation, local texture, etc.

There are many different ways to present the data such as pole figure, inverse pole figure, texture mapping, grain boundary mapping, and inverse pole figure contouring (IPF contouring). This information can be gathered in post-processing and can be utilized to understand the microstructural properties of a material.

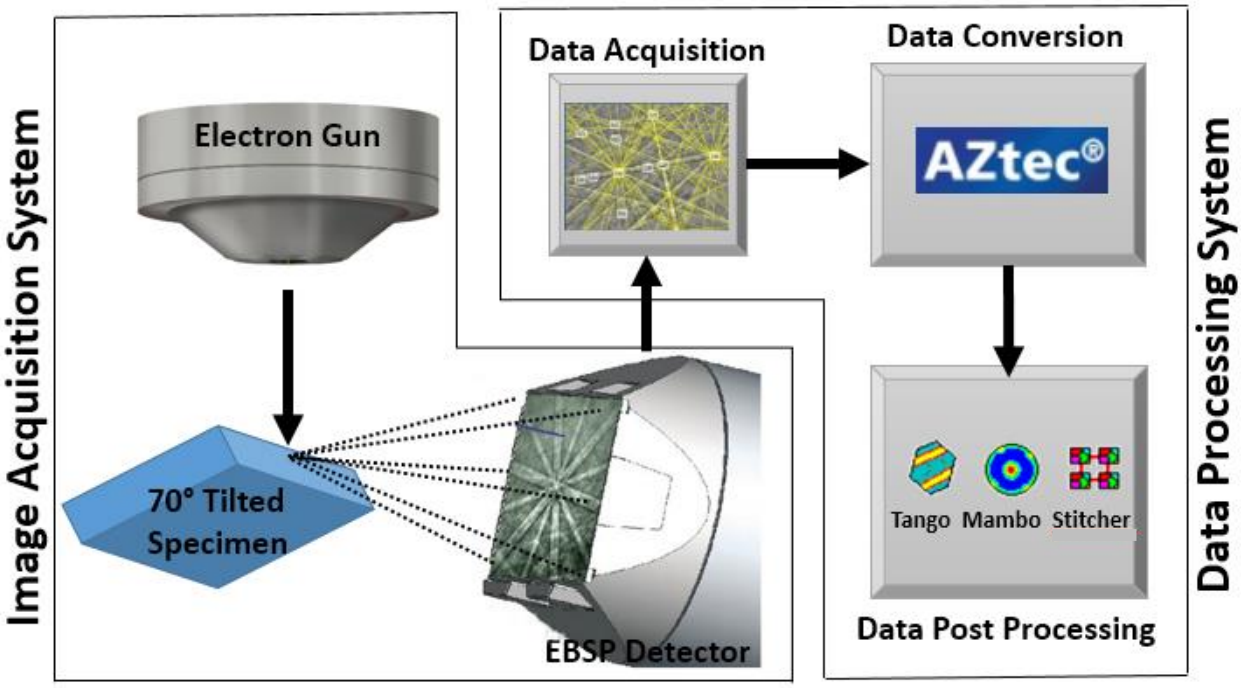

Figure 2-4: Flow chart of image acquisition and data processing procedure in EBSD analysis

2.2 Sample Preparation

The soldering technique selected for this study was reflow soldering. Most solder joints, especially Sn-3.5Ag/Cu system, exhibit two distinct microstructural features. The first is a eutectic structure consisting of IMC particles such as Ag_3Sn or Cu_6Sn_5 embedded in a β-Sn phase. The second is Cu–Sn IMC layer that consists of a Cu_6Sn_5 layer at the solder/Cu interface. Under particular conditions, Cu_3Sn could co-exist at Cu_6Sn_5/Cu interface. Short soldering time (2-3 minutes) and lower temperature (260°C) resulted in the formation of only Cu_6Sn_5. The dominant reactive species and products of the reaction between Sn and Cu vary greatly with temperature [81]. Cu_6Sn_5 could grow at all temperatures by diffusion of Cu through the Cu_6Sn_5 phase which also depends on the availability of bulk solder [12]. Reduced or absent Cu_3Sn at low temperature can be considered to be due to the limited diffusion of Sn

atoms through Cu_6Sn_5 IMC to the Cu substrate [81]. As soldering time and temperature increases, diffusion of Sn increases and both Cu_6Sn_5 and Cu diffuse in Cu_3Sn phase. At higher temperature, the diffusion of Cu becomes faster than that of Sn and Cu_3Sn grows faster on the Cu side [81]. For this study, soldering temperature of 360°C and soldering time of 240 minutes had been selected. This soldering time and temperature were selected in such a way that all types of IMC phases could be observed in a sample.

Two layers of Cu substrates were soldered together with Sn-3.5Ag alloy with joints about 450 µm thick (Figure 2-5). First, Cu surfaces were polished up to 1200 grit SiC using standard methods followed by cleaning with isopropyl alcohol. Solder paste was then deposited on the Cu surface. The chemical reaction was enhanced by an activation agent during the soldering process. The two Cu surfaces were then placed in an intimate contact in a thermal chamber at 360°C for 240 minutes and cooled it in the open air. A very good surface preparation is needed to conduct EBSD imaging experiment. Specimens were prepared for SEM and EBSD imaging using mechanical grinding from 240 grit to up to 1200 grit SiC, and polishing up to 0.05µm alumina solution, and vibratory polishing using 0.05µm colloidal silica. This sample preparation technique has been proved to be effective for EBSD experiment, especially for solder joint specimen [82].

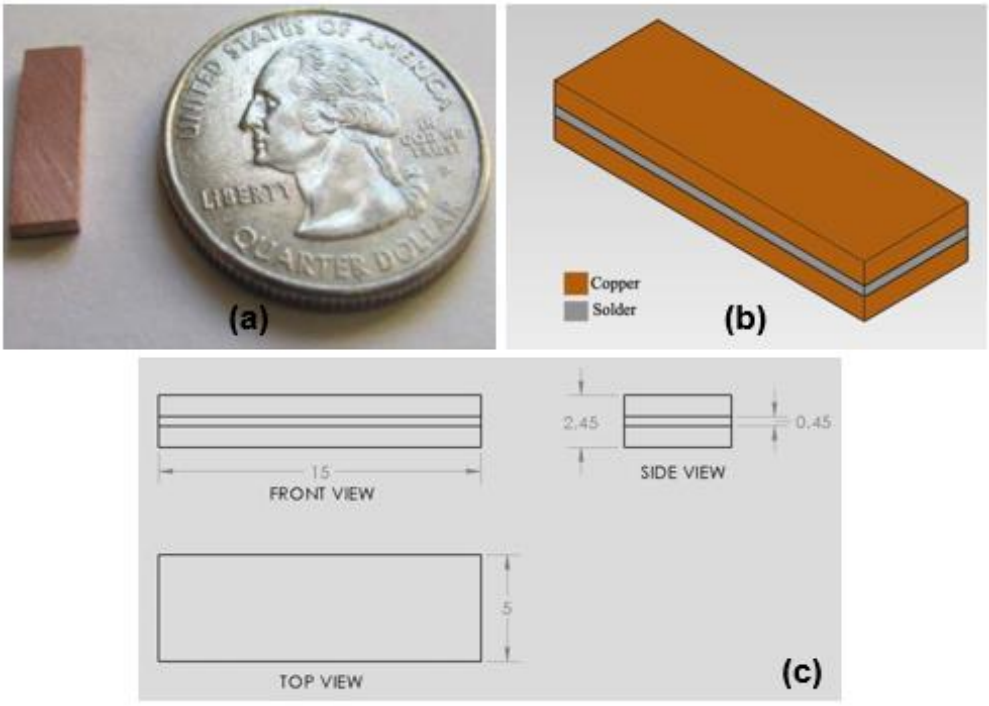

Figure 2-5: (a) Actual specimen design, (b) & (c) Schematic drawing of specimen. All dimensions are in mm.

2.3 Microstructural Investigation

The microstructure of the reflowed solder joint depends largely on the solder composition, reflow profile, cooling condition. The microstructure of a specimen reflowed at 360°C for 240 minutes is shown in Figure 2-6. It has been observed that during the interfacial reaction between solder alloy and Cu substrate, three different IMCs were formed. Cu_6Sn_5 has the highest volume fraction among all the IMCs in the joint. It is created due to the reaction between Cu substrate and Sn. Cu_6Sn_5 grains showed a scalloped type morphology between the Cu_3Sn and bulk solder. Cu_3Sn was formed in between Cu_6Sn_5/Cu interface region and uniformly formed along the substrate. This IMC was formed due to the increase in Cu dissolution with time and less interfacial reaction between Cu substrate and bulk solder alloy.

The barrier created by Cu_6Sn_5 IMC between Cu substrate and bulk solder reduces Sn delivery towards the substrate. Thus, Cu_6Sn_5 reacts with excess Cu and forms Cu_3Sn.

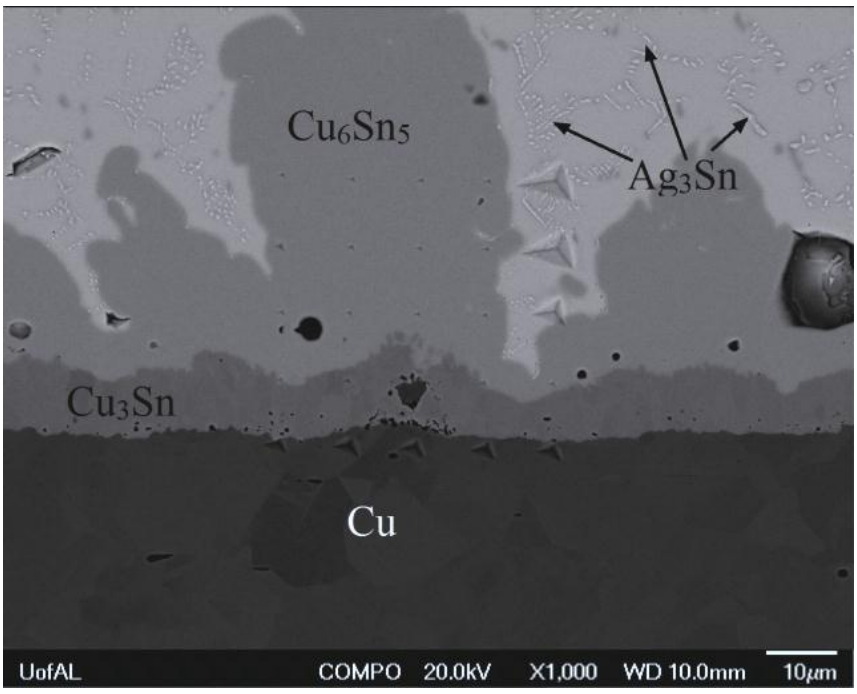

Figure 2-6: SEM image of Sn-3.5Ag/Cu substrate system with IMCs

Ag_3Sn was observed as particles, occupying random positions in bulk solder region. In our study, the average thickness of Cu_6Sn_5 layer was found to be around 25µm and about 8 µm for Cu_3Sn.

We have used EBSD analysis to determine the crystallographic structure of Cu_6Sn_5. For indexing, monoclinic and hexagonal Cu_6Sn_5 of lattice parameters 11.033×7.294×9.83˚A (JCPDS No.: 045-1488) and 4.2062×4.2062×5.0974˚A (JCPDS No.: 047-1575) respectively have been used [83] to verify crystal structure of Cu_6Sn_5 IMC. In EBSD imaging, Cu_6Sn_5 exhibited Kikuchi bands similar to the hexagonal crystal structure (HCP) and was indexed

accordingly. Others have also found Cu_6Sn_5 to have a hexagonal structure at room temperature through X-ray diffraction [16,18,22].

2.4 Investigation of Preferred Grain Growth Orientation

The scalloping of Cu_6Sn_5 grains in polycrystalline Cu indicates a preferred orientation along the growth axis as reported by some studies [20, 22]. Song et al. [16] provided X-ray diffraction mapping, which showed a strong orientation dependency of Cu_6Sn_5 IMC along the growth axis. EBSD mapping provides reliable information on the grain orientation. EBSD analysis shows that Cu_6Sn_5 grows along the *c-axis* of the hexagonal unit cell though there was some exceptions observed. Orientation perpendicular to the growth axis was random. This suggests that there is a strongly preferred grain growth direction along the *c-axis*. Similar findings have been reported in the literature [18], although the addition of Ni can affect the growth orientation [44]. On the other hand, the grain growth direction of Cu_6Sn_5 dramatically changes if the Cu substrate is a single crystal. Cu_6Sn_5 tends to elongate along the two low misfit directions between Cu_6Sn_5 and Cu atoms [84]. This suggests that the nucleation and growth of Cu_6Sn_5 is largely controlled by the substrate condition. Figure 2-7 shows an EBSD image with Euler angles of the individual grains. This figure clearly shows preferred crystallographic orientation of Cu_6Sn_5 grains.

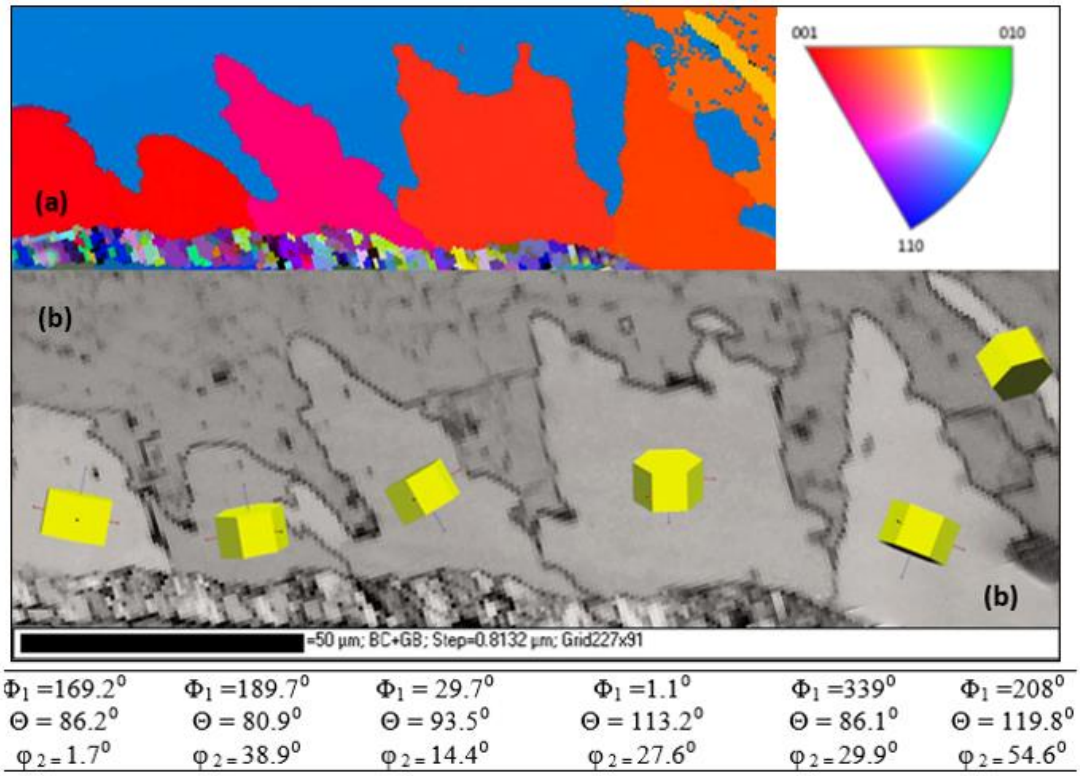

Figure 2-7: EBSD image showing (a) IPF contouring along transverse direction. (b) Illustration of orientation of Cu_6 Sn_5 unit cells with Euler angles

2.5 Nanoindentation

Local properties of materials can be obtained using nanoindentation, a widely used technique to determine local elastic properties directly. Some studies have shown that small-scale indentation may introduce complexities that arise from the complicated boundary and kinematic conditions, microstructural size effects, anisotropy as well as from the corresponding dislocation arrangements that are created at and around an indent. However, nanoindentation has been accepted as an accurate technique for measuring elastic properties in uniform homogeneous materials.

A nanoindenter, especially made with the diamond is indented on a material at a loading rate. The test can be displacement or load controlled. Occasionally, at maximum load, the indenter is kept indented for a certain dwell time. Then, the indenter is unloaded at a certain unloading rate. The indentation keeps a certain surface profile that has key parameters (Figure 2-8-a). The main information obtained from the nanoindentation experiment is the indent load vs. penetration depth curve. A typical curve is shown in Figure 2-8-b. There are vital features of the curve those are of interest: the maximum applied load, P_{max}; the maximum depth of penetration, h_{max}; the vertical distance along which contact is made (contact depth after load removal), h_c; and the unloading slope (contact stiffness) measured at maximum load, S.

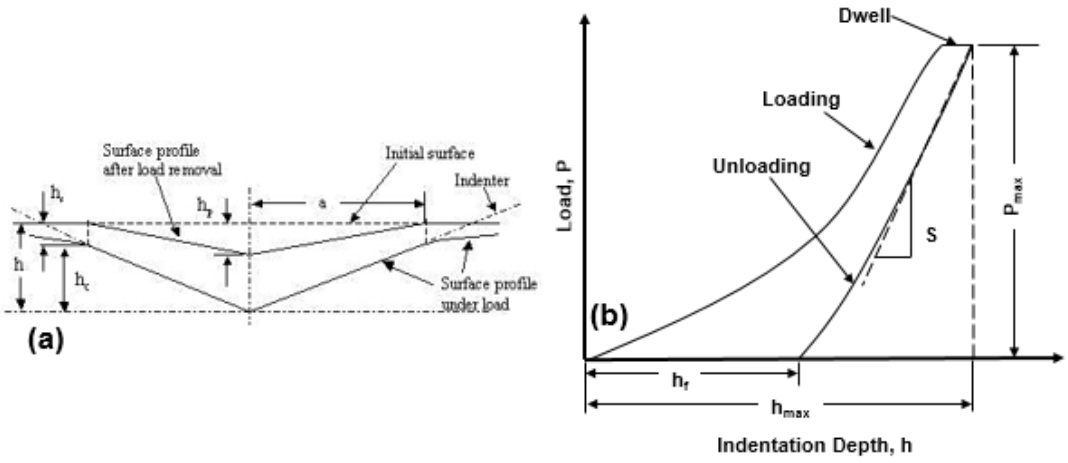

Figure 2-8: (a) A schematic diagram of an indenter at maximum load providing the surface profile, and (b) representative load vs. indentation depth curve with important annotation [85]

A major disadvantage of nanoindentation is the absence of quality imaging method to determine the phase of the indented area. Also, in many cases, if the grain size is significantly larger than the indent size, the individual tests yield the properties of single grains. These properties are functions of grain orientation due to the anisotropy of the crystal. The

crystallographic orientation of the grains and nanoindentation results must be used together to determine the local mechanical properties [86]. To overcome these concerns, nanoindentation can be used with scanning electron microscopy (SEM) and electron backscatter diffraction (EBSD) imaging.

2.5.1 Theory and Experimental Technique

The theory of nanoindentation is based on Hertz's work in the late 19th century that was focused on investigating the mechanics of contacting bodies [87]. However, the fundamental principles of nanoindentation tests were first postulated by Love et al. [88] who studied the problem of a linearly isotropic elastic half-space impressed by a rigid axisymmetric conical indenter. Sneddon [89] later provided a solution to the more general problem of a linearly isotropic elastic half-space indented by a rigid axisymmetric punch of an arbitrary profile.

Love et al. derived the contact pressure, *p(r)* and the relation between pressure, P and displacement or penetration depth, *h* which follows [88]:

$$p(r) = \frac{P}{\pi a^2}\cosh^{-1}\left(\frac{a}{r}\right) \text{ and } P = \frac{2E^* \tan\alpha}{\pi}h^2 \qquad \textbf{(2.2)}$$

Here, h is the penetration depth, E_r is the reduced elastic modulus of the indented material which depends on the indenter material too. Usually, the indenter material is diamond which has strong resistant to deformation but cannot be treated as ultimately rigid. When the indenter is deformable, the reduced modulus can be expressed using the following relation from contact mechanics:

$$\frac{1}{E_r} = \frac{1-\vartheta^2}{E} + \frac{1-\vartheta_i^2}{E_i} \qquad \textbf{(2.3)}$$

Here E and E_i is the elastic modulus of the indented material and indenter material respectively. $\vartheta \; and \; \vartheta_i$ denote the Poisson's ratio for indented and indenter material respectively.

For widely used three-sided berkovich indenter tip,α is the face semi-angle which is about 65.27°. Projected contact area for a berkovich indenter can be expressed in terms of contact depth by:

$$A = 3\sqrt{3}h_c^2 \tan^2 \alpha \qquad \textbf{(2.4)}$$

It follows from Equation 2.2 that the tangent stiffness or the slope of *P-h* curve, is given by:

$$\frac{dP}{dh} = \frac{4E_r tan\alpha}{\pi} h \qquad \textbf{(2.5)}$$

From this equation, E_r can be calculated from the experimental results of tangent stiffness. This value can then be used in equation 2.3 to calculate the actual elastic modulus of the indented material.

To calculate the hardness, maximum load, P_{max} is taken into account. Calculated contact area can be used to measure the hardness, H by dividing the maximum load by the contact area at maximum indent depth. The equation is as follows:

$$H = \frac{P_{max}}{A} \qquad \textbf{(2.6)}$$

2.5.2 Plastic Properties Determination Procedure

Plastic properties such as hardening exponent and yield strength were determined using the reverse analysis described by Dao et al. [74] . This method is proved to predict accurate values for a wide range of metals. Nanoindentation load vs. depth curve information is used in a set of dimensionless functions to determine yield point and strain hardening exponent. A more extensive discussion on the plastic properties determination by Dao et al. procedure is provided in **Appendix A**.

The indenter tip is generally made of diamond which has $\boldsymbol{E}$ of 1141 GPa and $\boldsymbol{\nu}$ of 0.07 [38]. Poisson's ratio of Cu_6Sn_5 has been measured by some researchers [39, 40] and it falls in the range of 0.30 to 0.36. For this study, a Poisson's ratio of 0.31 was assumed. SEM and EBSD were then conducted first to identify the location of the impressions and then determine the crystal orientation of the grains.

2.6 Nanoindentation Experimental Procedure

Nanoindentation was performed to determine the elastic and plastic properties of Cu_6Sn_5 IMC. A Hysitron Triboindenter (TI 900) machine (Figure 2-9-a) with a berkovich tip (Figure 2-9-b) was used to conduct the nanoindentation. This tip has an included angle (plane to edge) of 142.3° and radius of curvature of around 150 nm.

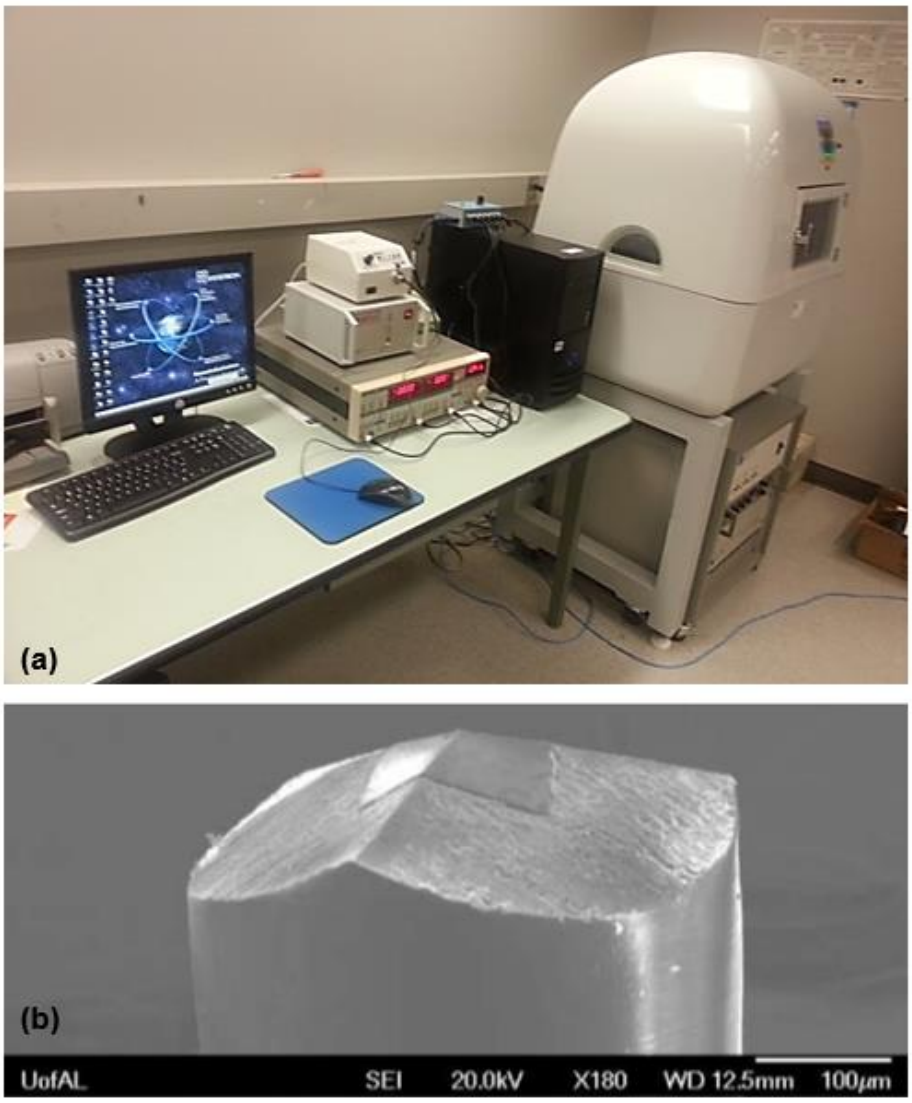

Figure 2-9: (a) Hysitron triboindenter machine system which is used to conduct nonoindentation experiments, (b) SEM image of a berkovich tip.

To achieve statistically significant number of indents in the Cu_6Sn_5, each test consisted of an array of 5 x 5 indents with 10 µm spacing. A maximum load of 5000 µN at a 1000µN/s loading rate was applied. Trapezoidal loading-unloading pattern with 5s load- 5s hold- 5s unload was utilized (Figure 2-10). Each test location was set in such a way that maximum number of indents could be placed at Cu_6Sn_5 phase.

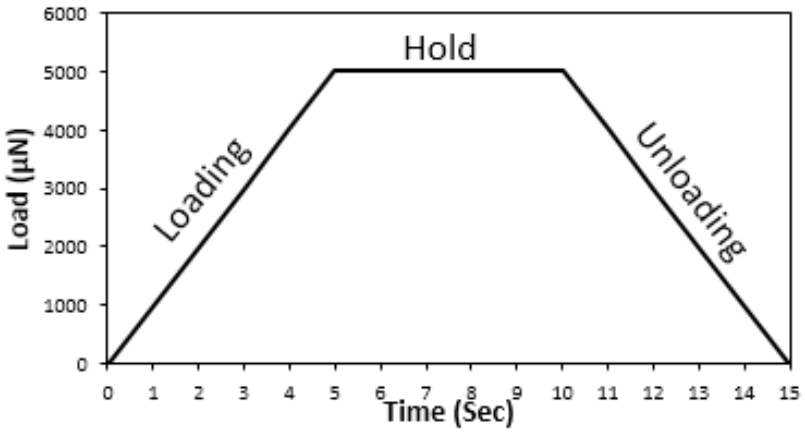

Figure 2-10: Loading pattern used in nanoindentation experiment

Reduced elastic modulus and hardness values were directly extracted from the nanoindentation software for each indent. To confirm the accuracy of the results, indentation curve data and the Oliver and Pharr method [85] were utilized to recalculate these properties. Loading curvature, C; maximum depth, h_m; contact depth, h_f and unloading stiffness, S, were used in the calculation. Depth has been used to calculate the contact area while a relation among unloading stiffness, reduced elastic modulus, E_r, contact area, A, and correlation factor, β, has been utilized to determine the reduced elastic modulus. The relation is of the form:

$$\mathbf{S = \beta \frac{2}{\sqrt{\pi}} E_r \sqrt{A}} \qquad \textbf{(2.7)}$$

SEM imaging was used to determine the exact locations of the impressions. Impressions on Cu_6Sn_5 were then marked on the SEM images and each impression was linked to its respective indentation load-displacement curve.

2.7 Results and Discussions

Nanoindentation was done at the area of solder IMCs in such a way that maximizes the number of indents occurring on the Cu_6Sn_5 region. The indents were numbered according to their indentation sequence. A representative load-displacement curve produced by nanoindentation for indents in Cu_6Sn_5 is shown in Figure 2-11c.

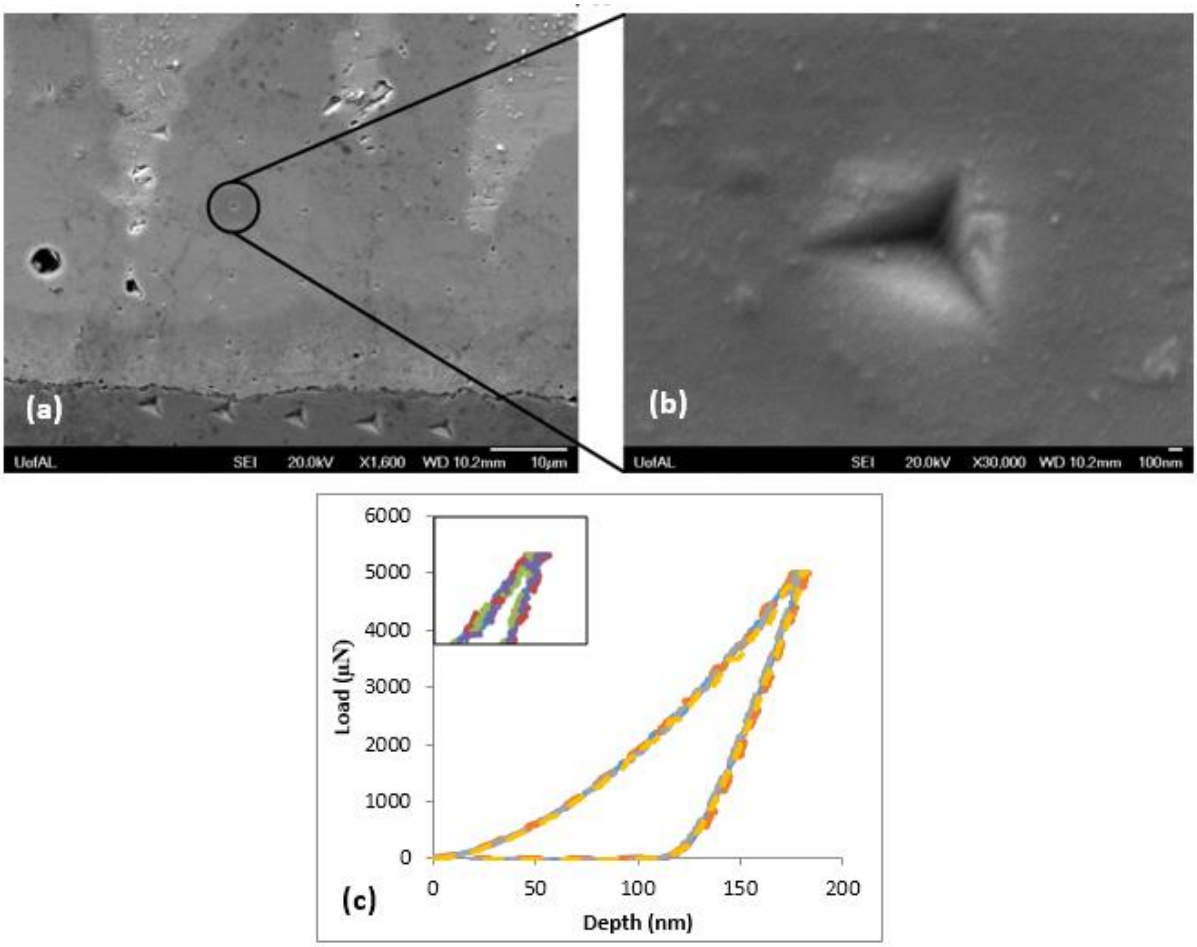

Figure 2-11 : (a) SEM image of indentations (b) SEM image of a single indent at Cu_6Sn_5 IMC (30,000X magnification) (c) Representative load-depth curves of Cu_6Sn_5 indents (inset figure is the magnified view of hold period of the curve).

2.7.1 Load-depth curve

Indentation was performed on various phases of the Sn-3.5 Ag/Cu soldering system such as the Cu substrate, Cu_3Sn and Cu_6Sn_5 IMCs, Sn-Ag solder that containing Ag_3Sn IMC and in pure Sn. All phases exhibited unique load-depth curves due to large differences in hardness and elastic-plastic proeprties. Representative load-depth curve for each area can be seen in Figure 2-12.

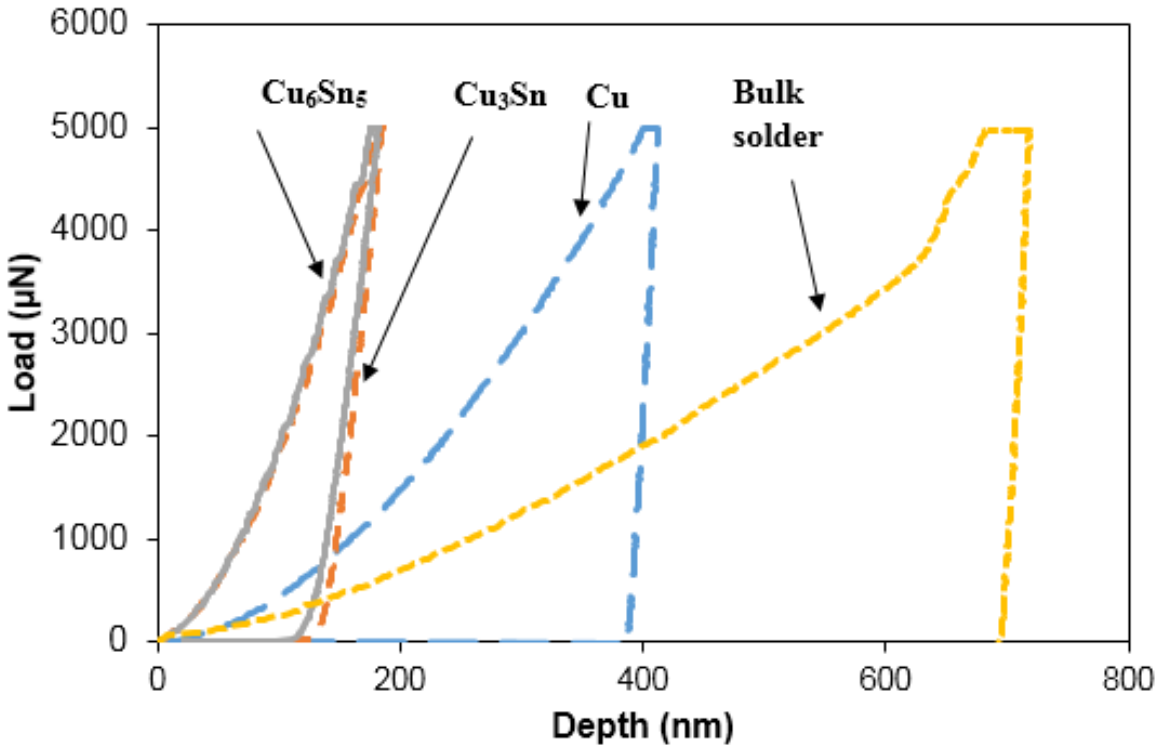

Figure 2-12: Representative load-depth curve for Cu_6Sn_5 and Cu_3Sn IMCs, Cu substrate and bulk solder alloy

Maximum penetration depth varies largely in different areas. Bulk solder shows highest penetration depth at maximum load and poor elastic recovery is observed in the unloading portion. Cu_3Sn and Cu_6Sn_5 IMCs have lower penetration depth along with moderate elastic

recovery. This can be attributed to the higher hardness of IMCs which was previously observed [27,28]. Bulk solder shows noticeable creep during the holding period.

As expected, the load-depth curve for all Cu_6Sn_5 indents followed the same trend irrespective of the region. A holding period was introduced to minimize any adverse effect on the unloading portion of the curve due to creep. Creep behavior during hold time at maximum load has an effect on the measured hardness and elastic modulus values during indentation [90]. Tests conducted on a wide range of materials showed that the length of hold time has great potential to influence measured values of hardness and elastic modulus. In this study, Cu_6Sn_5 showed low tendency to creep. During all indentation tests, average creep was around 3-4 nm during hold time. Average maximum penetration depth was found to be around 178 nm. Pile up at the indentations could potentially increase actual contact area that can lead to an under or over estimation of hardness and elastic modulus [91]. To investigate any pile up during indentation, SEM images of the indent impression were obtained. No pile up was observed for Cu_6Sn_5 indents.

2.7.2 Mechanical properties

Indentation was performed normal to the growth axis of Cu_6Sn_5 grains. Figure 2-13 shows a schematic illustration of the indentation direction on a Cu_6Sn_5 hexagonal unit cell.

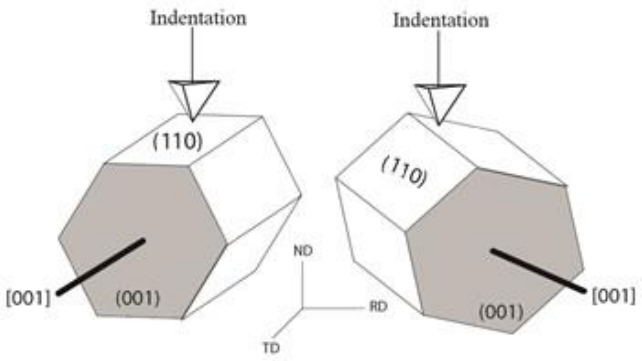

Figure 2-13: Schematic illustration of indentation direction on Cu_6Sn_5 IMC.

In this analysis, each grain contained an average of six indents. The indents that were closer than 4μm from the grain boundaries or at defects were excluded due to the possible edge effects [24].

EBSD imaging was done to observe grain features. Five grains of different crystallographic orientation along normal to the growth axis were taken into consideration to observe local mechanical properties of Cu_6Sn_5. Euler angles and inverse pole figures were obtained from EBSD imaging as shown in Figure 2-14. Euler angles obtained from EBSD imaging for each grain are given in Table 2-1.

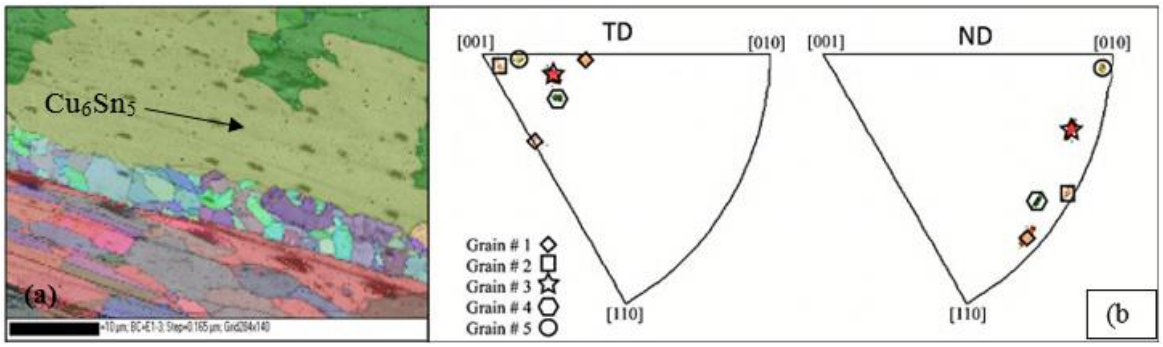

Figure 2-14: (a) EBSD image of Cu_6Sn_5 grain, (b) Inverse pole figure for five grains.

Table 2-1: Euler angles for five observed grains

Angle	Grain# 1	Grain# 2	Grain# 3	Grain# 4	Grain# 5
φ_1	332.11^0	353.81^0	161.77^0	22.44^0	190.66^0
Θ	95.2^0	92.82^0	101.13^0	100.78^0	84.4^0
φ_2	43.35^0	29.12^0	16.62^0	34.28^0	2.87^0

Table 2-2: Local mechanical properties of five grains

Properties	Grain# 1	Grain# 2	Grain# 3	Grain# 4	Grain# 5
Avg. elastic modulus (GPa)	115.787±0.93	116.97±1.18	116.31±1.31	116.53±0.95	111.985±1.32
Avg. hardness (GPa)	7.77±0.085	7.862±0.11	7.801±0.116	7.926±0.099	7.87±0.064
Avg. yield strength (MPa)	2737.15±87.71	2691.43±174.81	2853.60±123.01	2914.98±174.94	2921.613±158
Avg. strain hardening exponent	0.123±0.0124	0.136±0.0322	0.108±0.0241	.098±0.0397	0.10342±0.0281

Local elastic-plastic properties of Cu_6Sn_5 for five grains are listed in Table 2-2. Note that the first four grains show statistically indistinguishable values of elastic modulus. A relatively low elastic modulus was observed for grain #5 which had its [010] direction parallel to the loading direction (Figure 2-14 b). Our finding seems to support that of Mu et al. [18]. This can be attributed to the anisotropic effect of Cu_6Sn_5 IMC grains. According to ICDD (International Center of Diffraction Data) JCPDS number 047-1575 (for hexagonal, $p6_3/mmc$) [40] and lattice structure of Cu_6Sn_5 IMC [23], the inter plane distance is greater between prism planes than any other plane distances, and thus has a less densely packed atomic structure. Therefore, the indenter had to displace fewer atoms in the lattice which resulted in lower interatomic stress generation. Indentation in other planes would generate higher interatomic stress due to densely packed atoms in the lattice structure.

All five grains exhibit almost same hardness value. Average hardness reported in previous studies fall nicely within the range of our test results (Table 2-2). Relatively lower yield strength was observed for grain #2 which has its (0001) plane almost parallel to the loading

direction. This can be attributed to the slip system activity of hexagonally packed Cu_6Sn_5. In HCP crystal, slip occurs most readily on (0001) plane. As indentation loading in grain #2 was almost parallel to a (0001) plane, it created a direct shear stress along this plane. As a result, slip between the (0001) plane occurred more easily and contributed to the lower yield strength of the grain. Average yield strength reported in this study was higher than the values published in other references. Deng et al. [28] and Song et al. [92] used Dao's model to investigate plastic properties of Cu_6Sn_5 and obtained lower yield strength than our findings. It can be assumed that this is due to variations in sample fabrication and testing techniques. Also, Song et al. [92] used samples with Cu_6Sn_5 thickness of only 9µm which increases the likelihood of having edge effects. They also did not take grain orientation and size into consideration. Strain hardening behavior was almost constant for all five grains in this study. Deng et al. did not observe any strain hardening exponent for Cu_6Sn_5 and Cu_3Sn IMCs. Average strain hardening exponent found in this study correlates well with the values obtained in Song's work.

2.8 Summary and Conclusions

Mechanical characterization of Cu_6Sn_5 IMC was done using a combination of nanoindentation and SEM-EBSD imaging. Effect of crystallographic orientation on mechanical properties of Cu_6Sn_5 was also taken into consideration.

SEM and EBSD data shows that on polycrystalline Cu, Cu_6Sn_5 grain growth occurs mostly along the *c-axis* of the hexagonal unit cell. No crystallographic preferred orientation was observed normal to the growth axis.

Elastic-plastic properties of Cu_6Sn_5 grains with different orientations along the normal to the growth axis were determined. Results indicate that the hardness for Cu_6Sn_5 grains with

different orientation along normal to growth axis is statistically indistinguishable. Lower elastic modulus was observed for grain with [010] direction parallel to the loading direction. The yield strength of a grain with (0001) plane parallel to the loading direction was slightly lower than other grain orientations. Overall, obtained experimental results were found to be within the range of literature.

CHAPTER 3 : Development of Single Crystal Plasticity Finite Element (CPFE) Model of Cu_6Sn_5 IMC

3.1 Introduction

As the size of the joints become closer to the grain size, joints may only contain a few number of grains of Cu_6Sn_5. This manifest itself in statistical grain size effects, as well as anisotropy. Modeling these joints using bulk properties of Cu_6Sn_5 does not capture the actual behavior of these joints, especially when plastic deformation is involved. Plastic deformation, starting at yield point happens to be associated with the activation of slip systems. However, the crystallographic slip parameters needed to model the single crystal behavior of Cu_6Sn_5 is not available in the literature. This work uses a combined strategy based upon experiments, modeling, and comparative analysis to obtain slip system parameters that could predict the slip process of Cu_6Sn_5.

3.2 Crystal Plasticity Theory

Single crystal plasticity theory [93] assumes that plastic deformation is the sum of the crystalline slip in all activated slip systems. Plastic slip in a slip plane occurs when the resolved shear stress on a crystallographic plane in the direction of slip reaches a critical value [94]. Rice and Hill [95] and Rice [96] formulated the precise theory to understand the plastic behavior of single crystal and polycrystalline. In this model, crystal deformation results from a combination of the elastic stretching and rotation of the lattice and plastic slip on the different slip systems. The essential constitutive relations are briefly described in the following sections. A more detailed explanation is given in Huang et al. [97].

Total deformation gradient can be expressed using the multiplicative decomposition of the deformation gradient into elastic and plastic part [98] (Figure 3-1). Three configurations have been proposed to explain the deformation process. The elastic deformation is the reversible response of the lattice due to the external loads and displacements, and plastic deformation is an irreversible permanent deformation. According to the multiplicative decomposition method, first, there is a plastic flow of material, starting at zero stress, from the initial configuration to the intermediate configuration where lattice orientation and spacing are same as the reference configuration followed by elastic deformation that contains stretching and rotation of the lattice [98].

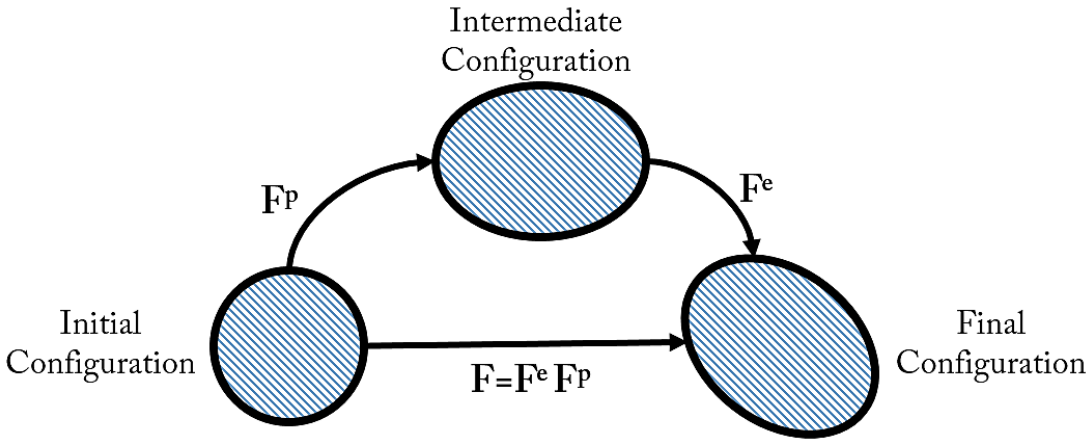

Figure 3-1: Elastic-plastic deformation expressed using multiplicative decomposition of the deformation gradient [98]

Lee's decomposition law [98] provides a sound kinematic and kinetic basis for elastoplastic constitutive analysis of single crystals. Total deformation gradient, **F** can be described with the following expression:

$$\mathbf{F} = \mathbf{F^e F^p} \tag{3.1}$$

Here, $\mathbf{F^e}$=elastic deformation gradient which includes stretching and rotation, and $\mathbf{F^p}$= plastic deformation gradient that includes crystallographic slip on the slip systems, where det$\mathbf{F^e}$ >0 and with incompressibility constraint det$\mathbf{F^p}$ =1.

Stress-strain relation is used in terms of 2nd Piola- Kirchhof stress tensor ($\mathbf{S}$= det$\mathbf{F^e F^{e-1} \sigma F^{e-T}}$) and Lagrange Green strain tensor ($\mathbf{E^c}$= (1/2) $\mathbf{\{F^{eT} F^e - I\}}$) such as:

$$\boldsymbol{S_{ij} = C_{ijkl} E^e_{kl}} \tag{3.2}$$

Here, $\mathbf{C_{ijkl}}$ is the components of elastic stiffness tensor when a material is oriented along its undeformed configuration, and can fully describe the anisotropic elastic behavior of a material.

Plastic deformation gradient rate is stated in terms of plastic velocity gradient and can be presented by:

$$\dot{\mathrm{F}}^{\boldsymbol{P}} = \boldsymbol{L^p F^p} \tag{3.3}$$

It is assumed during shearing, the plastic deformation occurs only due to the crystalline slip. Therefore, plastic velocity gradient can be described as:

$$\boldsymbol{L^p} = \sum_{\propto} \dot{\gamma}^{\alpha} \boldsymbol{s^{\alpha}} \tag{3.4}$$

Here, $\boldsymbol{s^{\alpha}}$ is the schmid tensor, which can be described as $\boldsymbol{s^{\alpha}} = \boldsymbol{s_i^{\alpha}} \otimes \boldsymbol{m_j^{\alpha}}$. Here, $\boldsymbol{s_i^{\alpha}}$ and $\boldsymbol{m_j^{\alpha}}$ is slip direction and slip plane normal in the reference configuration. . $\otimes$ Indicates the dyadic product of two tensors or vectors.

Plastic shearing rate or slipping rate, $\dot{\gamma}^{\alpha}$ in a rate dependent crystalline solid can be expressed with the help of viscoplastic flow rule. The flow rule gives an advantage of not using an iterative procedure to identify active slip systems. $\dot{\gamma}^{\alpha}$ can be presented in terms of corresponding resolved shear stress, τ^{α} [99] as

$$\dot{\gamma}^{\alpha} = \tilde{\gamma} \left| \frac{\tau^{\alpha}}{\tau^{o}} \right|^{\frac{1}{m}} sgn(\tau^{\alpha}) \tag{3.5}$$

Where $\tilde{\gamma}$ is reference shearing rate, τ^{α}= α^{th} slip system resolved shear stress, τ^{o}= αth slip system initial critical resolved shear stress and *m*= strain rate sensitivity exponent. $\tilde{\gamma}$, and m are material properties. The impact of any set of slip system, β, on the hardening behavior of a fixed slip system, α, can be expressed as slip system resistance or strain hardening through an incremental relation, which can be expressed by the following relation:

$$\dot{\tau}^{\alpha} = \sum_{\beta=1}^{n\ slip} h^{\alpha\beta} \left|\dot{\gamma}^{\beta}\right| \quad \textbf{(3.6)}$$

Here, $h^{\alpha\beta}$ are slip hardening moduli, the sum ranges over all activated slip systems. $h^{\alpha\alpha}$ and $h^{\alpha\beta}$ are self and latent-hardening modulus respectively. Latent hardening moduli can be calculated from the self-hardening moduli with the inclusion of a latent hardening constant. The expression can be portrayed as:

$$h^{\alpha\beta} = q^{\alpha\beta} h^{\alpha\alpha} \quad \textbf{(3.7)}$$

Where $q^{\alpha\beta}$ is the latent hardening constant which is the ratio of Latent hardening to self-hardening rate, $q^{\alpha\beta}$ can be assumed as the following for a coplanar slip system [100]:

$$q^{\alpha\beta} = \begin{cases} 1\ when\ \alpha = \beta \\ q\ when\ \alpha \neq \beta \end{cases}$$

Hyper secant law, provided by Peirce, Asaro and Needleman [101] has been utilized here to calculate self-hardening moduli for the slip systems:

$$h^{\alpha\alpha} = h^{0} sech^{2} \left|\frac{h^{0}\gamma}{\tau^{s} - \tau^{0}}\right| \quad \textbf{(3.8)}$$

In this formulation, h^0=initial hardening modulus**,** γ= cumulative shear strain for all slip systems, and τ^s= saturation stress.

3.3 Slip Model Parameters of Cu_6Sn_5

A lot of modeling approaches have been developed to describe the deformation mechanism of Tin (Sn) and bulk solder in soldering alloy system [72,73]. To completely model the behavior of solder joints, it is necessary to study the slip deformation of Cu_6Sn_5 crystal. HCP crystal slip system CRSS is typically different for each slip system which depends on the atomic density,

precipitates as well as temperature [102,103]. Basal slip system tends to show a very low CRSS while the other slip systems may show a large variation.

Nanoindentation combined with CPFE simulations provides an alternative opportunity to study the behavior of single crystals in a polycrystalline environment [70,104,105]. Bieler and his group [104] have utilized nanoindentation test results to optimize the CPFE parameter. They have conducted nanoindentation and EBSD experiments on a single crystal of titanium and performed crystal plasticity analysis to obtain the unknown CRSS of titanium single crystal by fitting the experimental nanoindentation load-depth curve with simulated curve. Ling Li [70] fitted the stress-strain curve obtained from tensile tests with CPFE simulated results to obtain the model parameters for polycrystalline aluminum alloys. As, indentation size is much smaller than the grain size, nanoindentation tests can be assumed as the deformation of a constrained single crystal. Such experiments allow the separation of the influence of intrinsic grain properties such as grain orientations, from the influence of polycrystallinity such as grain boundaries and neighboring grain orientations. Previously, a study of mechanical properties of Cu_6Sn_5 single crystal was conducted by combination of nanoindentation and EBSD analysis [106]. Due to preferred grain orientation, <c> direction of Cu_6Sn_5 is found to be perpendicular to the shear loading direction in joints, where, <a> direction happens to be parallel to loading direction (Figure 3-2). So, it is hypothesized that slips occur readily at <a> direction. Slip systems activation information for Cu_6Sn_5 has not been studied yet and there is no information of the sequence of activation of slip systems in literature. However, it is widely accepted that <c+a> type pyramidal slip system has 2-3 times higher CRSS than <a> type slip systems [107,108]. On the other hand, when the *c-axis* of a crystal grain is oriented parallel to the

uniaxial applied stress, non-basal <c+a> pyramidal slip and twinning are needed for the grain to deform [109]. As, Cu_6Sn_5 has a preferred grain growth orientation along *c-axis* in solder joint, the applied stress has lower probability of being parallel to the *c-axis* of the crystal. In this case, there is a very low likelihood of activating <c+a> pyramidal and twinning. For simplicity in modeling, slips that works at <a> direction i.e. basal, prismatic, and pyramidal slip systems have been taken into consideration in this study.

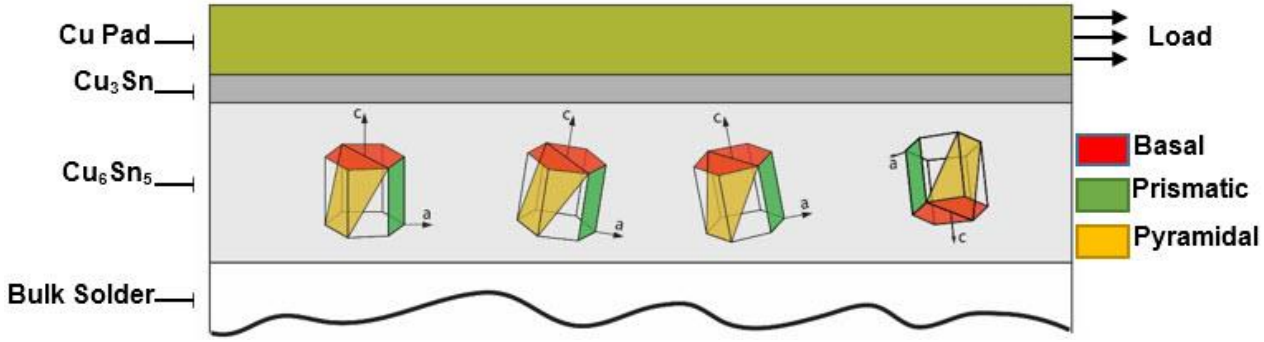

Figure 3-2: Schematic view of preferred crystallographic orientation of Cu_6Sn_5 where <a> direction of the crystal is parallel to the shear loading direction.

A study to extract the yield strength and strain hardening exponent of Cu_6Sn_5 IMC has been performed before [106] and described in the previous section. Yielding in a single crystal begins when the resolved shear stress on slip plane along the slip direction exceeds a critical value. Critical resolved shear stress of a α^{th} slip system can be computed from yield stress, σ_{ij}^{y} by:

$$\tau_{crss}^{\alpha} = \sigma_{ij}^{y} \boldsymbol{s_i^{\alpha}} \otimes \boldsymbol{m_j^{\alpha}} \qquad \textbf{(3.9)}$$

Schmid factor, ($m = \boldsymbol{s_i^{\alpha}} \otimes \boldsymbol{m_j^{\alpha}}$) is frequently applied to analyze the possibility of the activation of slip systems. Many studies have been performed to calculate the Schmid factor of FCC, BCC [110] and HCP [111] single crystals. Researchers have used Schmid factor to predict the

CRSS of slip systems from single crystal yield strength and vice versa [112–114]. They have used the assumption that as yield occurs, all the primary slip systems are being activated together. Both Schmid factor and CRSS of Cu_6Sn_5 are not available in the literature. Thus, due to the similarities in crystal structure ($P6_3/mmc$) [115], Schmid factor for HCP structured Mg derived by Nan et al. [111] has been utilized in our study to predict the CRSS of basal, prismatic, and pyramidal slip systems.

Nanoindentation tests performed in the previous section was used to predict the CRSS of three slip systems. Indentations performed in a single grain was used to extract yield strength of that grain. The single grain had an Euler angle ($\varphi_1 = 353.81°, \theta = 92.81°, \varphi_2 = 29.12°$) as determined using EBSD analysis.

Euler angle information of this indented grain provides the necessary information on how the grain is oriented with respect to the loading direction. Using the crystal structure and slip system information of HCP crystal, the corresponding angle of 87.19° between the loading direction and *c-axis* were obtained. Nan et al. [111] provided Schmid factors of basal, prismatic and pyramidal slip systems with respect to the angle between *c-axis* and loading direction. With this information, the Schmid factor for these three primary slip systems were calculated. Yield stress obtained in the single grain nanoindentation test, happens to be the critical stress, when the slips start to occur in the crystal and introduce plastic deformation. As, the nanoindentation test was conducted on a single grain, the yield stress obtained from the test was utilized as the yield stress of the single crystal for the corresponding orientation. However, for the sake of the missing information on the slip system activation of Cu_6Sn_5 in literature, it

was assumed that all primary slip systems start to deform when the yielding starts to occur in the crystal.

Equation 3.9 was used to predict the CRSS of the slip systems using the yield stress obtained through the nanoindentation test and the Schmid factor calculated from the angle of loading direction and *c-axis* of the HCP crystal. Multiplying yield stress and Schmid factor value, according to Equation 3.9, we achieved the CRSS of the slip systems as 260 MPa, 1500 MPa and 1310 MPa for basal, prismatic and pyramidal slip systems respectively. Initial hardening modulus was considered identical for all slip systems [72].

3.4 Crystal Plasticity Finite Element (CPFE) Model Description

Commercially available finite element software ABAQUS in combination with an extended user material subroutine **(UMAT)** was used for the finite element simulation. One of the major challenges faced during this study was to prepare the ABAQUS software to handle the UMAT feature. The performed procedure to enable the task is documented in details in **Appendix B**.

A series of simulation of nanoindentation analysis have been performed to simulate the similar indentation behavior in the single crystal. A square block, (5 x 5 x 5 μm) assigned with single crystal properties using custom user material (UMAT) feature in Abaqus was utilized (Figure 3-3). The length and width of the sample block are bigger enough as the stress contour never reaches the surrounding surface. Two crystallographic directions provide complete orientation information of the crystal. [0001] (*c-axis*) and $[1\bar{1}20]$ direction of the crystal were oriented about the global Y-axis and X axis respectively. Indentation direction was set along the global Z- axis of the model (Figure 3-3b). Berkovich indenter with a radius of curvature of 150 nm

was designed to perform nanoindentation simulation and it was constrained as a rigid body. We assumed a rigid indenter penetrating a homogeneous anisotropic single crystal. Friction is known to have a minor effect on load-displacement response of indentation [116]. Friction coefficient of 0.1 has been used for the contact interaction between the indenter and the sample.

A three dimensional finite element mesh with 8-node linear brick elements (C3D8R) with reduced integration and hourglass control is used for the discretization of the sample. The lower surface of the sample is fixed in all directions and the side and top surfaces are free to deform in any direction. Biased meshing criteria was utilized to refine the mesh at indentation area. It allows to have good resolution of the contact area and at the same time requires less computational time. Mesh sensitivity analysis was performed to calculate optimum mesh resolution. Loading conditions were kept similar to experiments described in the experiment section to compare the simulation results with the experiment. Creep was not modeled in the simulation. In experiments, creep of 3~5nm was observed which is considered insignificant.

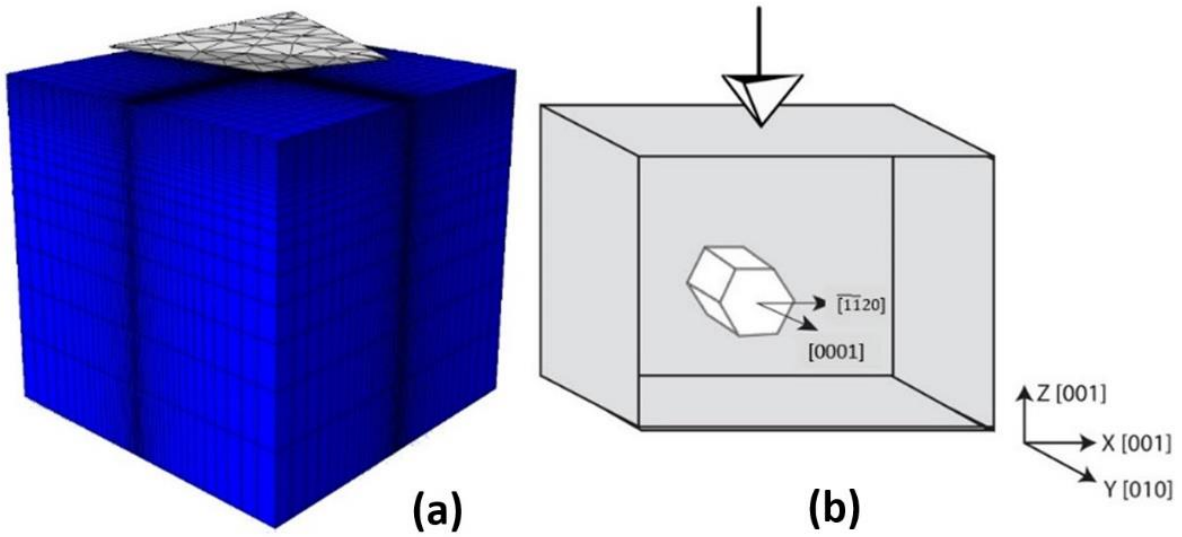

Figure 3-3: (a) Nanoindentation FE model, (b) Schematic of crystal orientation used in the model.

The material parameters used in the calculations are shown in Table 3-1. To introduce elastic anisotropy, stiffness matrix calculated using first principle calculation rule by Lee et al. [117] has been used. There is no information available on the self and latent hardening behavior of Cu_6Sn_5. Effect of self and latent hardening of slip systems were assumed to be equal and thus, latent hardening constant is taken as 1 [118]. A small reference shearing rate of $0.001sec^{-1}$ was assumed in this approach as a quasi-static reference. This assumption is a convenient fitting method where reference values can be taken from quasi-static test process [119].

Table 3-1: Material properties and slip parameters of Cu_6Sn_5 crystal

Stiffness Matrix (MPa) [117]	m [92]	$\dot{\tilde{\gamma}}$ sec^{-1}	$q^{\alpha\beta}$ [118]
D_{1111}=156400, D_{1122}=62200, D_{2222}=165200, D_{1133}=69400, D_{2233}=60600, D_{3333}=155800, D_{1112}=0, D_{2212}=0, D_{3312}=0, D_{1212}=42300, D_{1113}=-11300, D_{2213}=16800, D_{3313}=5600, D_{1213}=0, D_{1313}=51900, D_{1123}=0, D_{2223}=0, D_{3323}=0, D_{1223}=7400, D_{1323}=0, D_{2323}=4800	0.08	.001	1

Following parameters are used for the description of the flow behavior: critical resolved shear stress, τ_{crss}; saturation stress, τ_s; initial hardening modulus parameter h^o which determines the initial hardening slope. These crystal plasticity constitutive parameters are not available in literature. Calibration of these parameters were needed to be carried out using CPFE simulation. To calibrate and optimize these parameters, first we were required to understand their roles and effects on the load-displacement behavior. A numerical experiment was designed to investigate the effects of initial hardening modulus and saturation stress on the load-displacement curve (Table 3-2). These values are selected in such a way that the effects of the parameters on load-displacement curves can be observed. For each case, load-displacement curves are extracted from the simulation and plotted.

Table 3-2 : Numerical design of experiment (NDoE)

Saturation Stress	Initial hardening modulus
1.5 τ_{crss}	8000
	12000
	16000
2 τ_{crss}	8000
	12000
	16000
2.5 τ_{crss}	8000
	12000
	16000

Following Figure 3-4a shows a series of load-displacement curve when the saturation stress, τ_s is constant ($2\tau_{crss}$) and initial hardening modulus, h^o varies. Also, Figure 3-4b contains another series of load-displacement curve with constant h^o and varying τ_s.

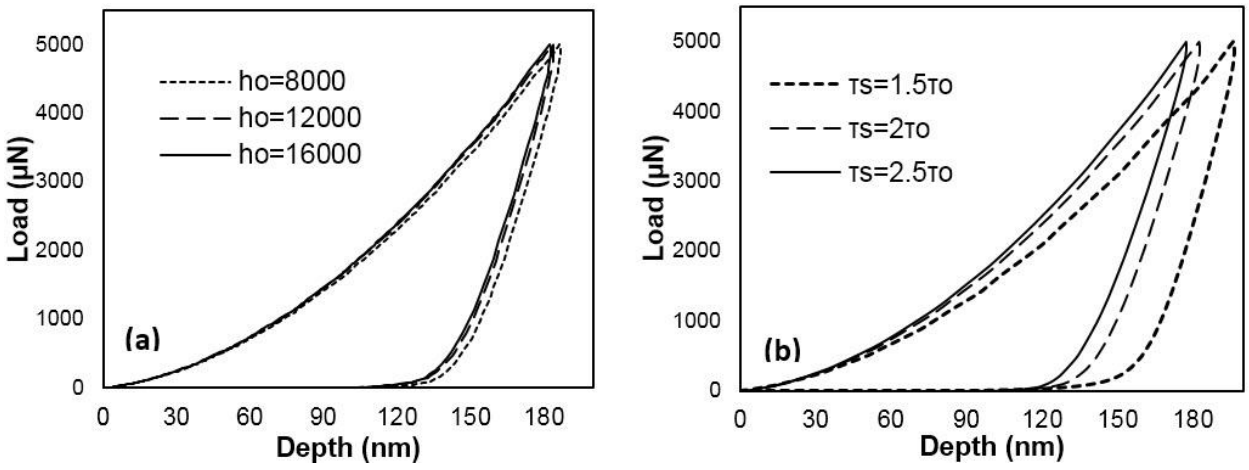

Figure 3-4 : (a) Representative load-displacement curve with constant saturation stress ($2\tau_{crss}$) while ho varies (b) Representative load-displacement curve with constant ho (12000 MPa) while τ_s varies.

Changes in Initial hardening modulus, h^o does not have significant effect on final indent depth when the saturation stress, τ_s is kept constant (Figure 3-4a). Maximum drop of 1.8% has been observed when the τ_s is $2.5\tau_{crss}$ and h^o changes from 8000 MPa to 12000 MPa which is negligible. Similar observation has been reported by Liu et al. [120]. They observed negligible effect of initial hardening modulus on the final indent depth. Residual indent depth tends to decrease with the increase of h^o due to the increasing material recovery (Figure 3-4b). The opposite scenario is seen when an increase in residual indent depth is observed with the increase in τ_s (Figure 3-4b) as increasing saturation stress induces more plastic deformation in material and thus reduces material recovery. However, at h^o of 16000 MPa, no noticeable

changes occur with the changes in τ_s (Figure 3-5b, Figure 3-6b). Higher initial hardening modulus may neutralize the effect of changing saturation stress.

Unloading portion of load-displacement curve can be described by the penetration depth ratio, h_f / h_{max} (ratio of residual indent depth to maximum indent depth). It has been used by several researchers to describe the elastic recovery influence [121]. Penetration depth ratio seems to decrease with the increase in h^o while τ_s is constant and increases with the increase in τ_s while h^o is constant (Figure 3-7a, Figure 3-7b).

The effects of initial hardening modulus and saturation stress on load-displacement curve discussed here were utilized to calibrate the model parameters which could be used to generate similar load-displacement curve with the shape and properties i.e. final indent depth, residual depth, penetration depth ratio similar to the experimental curve. For initial hardening modulus, h^o of 12000 MPa and saturation stress, τ_s of $2.5\tau_{crss}$, a good fit between experimental and simulated load-displacement curve has been obtained (Figure 3-8a). Also, for these values, we have obtained similar final indent depth, residual depth, and penetration depth ratio. These similarities ensure similar mechanical behavior of Cu_6Sn_5 single crystal.

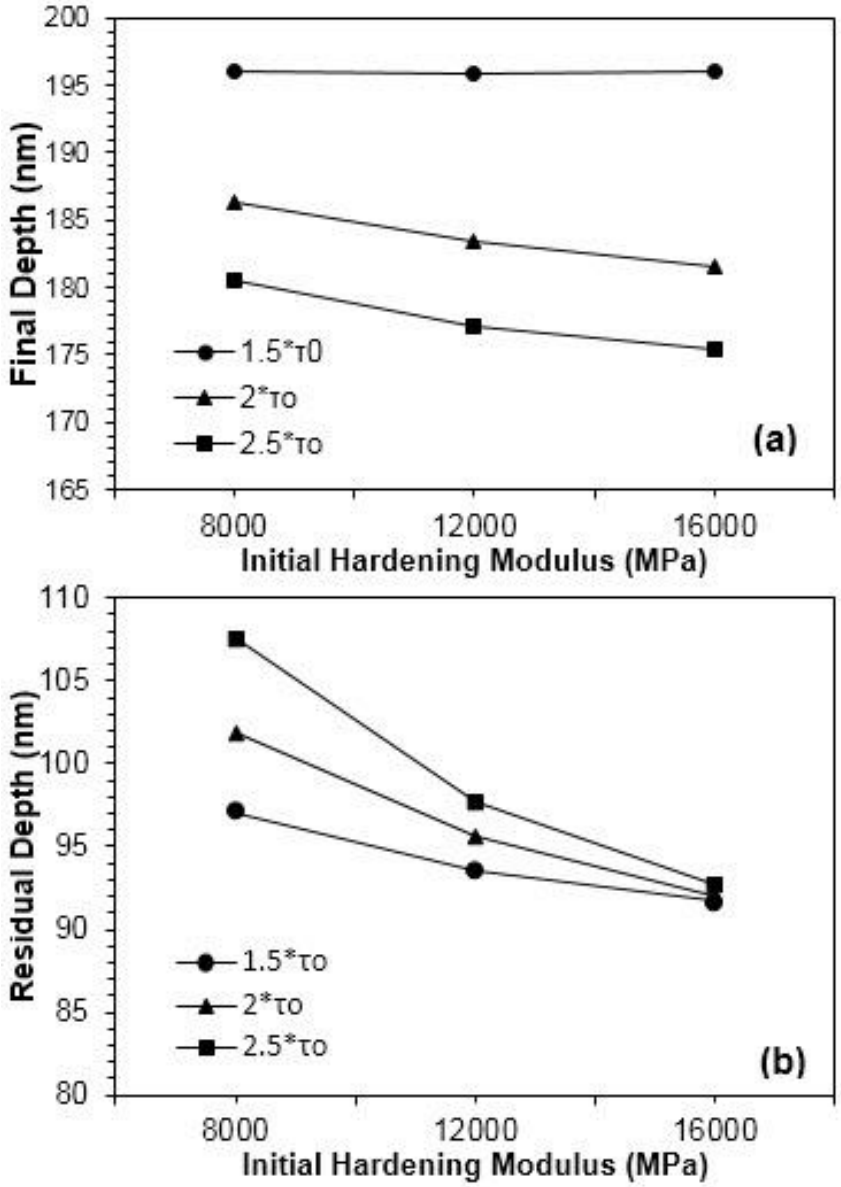

Figure 3-5 : Effects of initial hardening modulus on (a) final indent depth, and (b) residual indent depth of load-displacement curve.

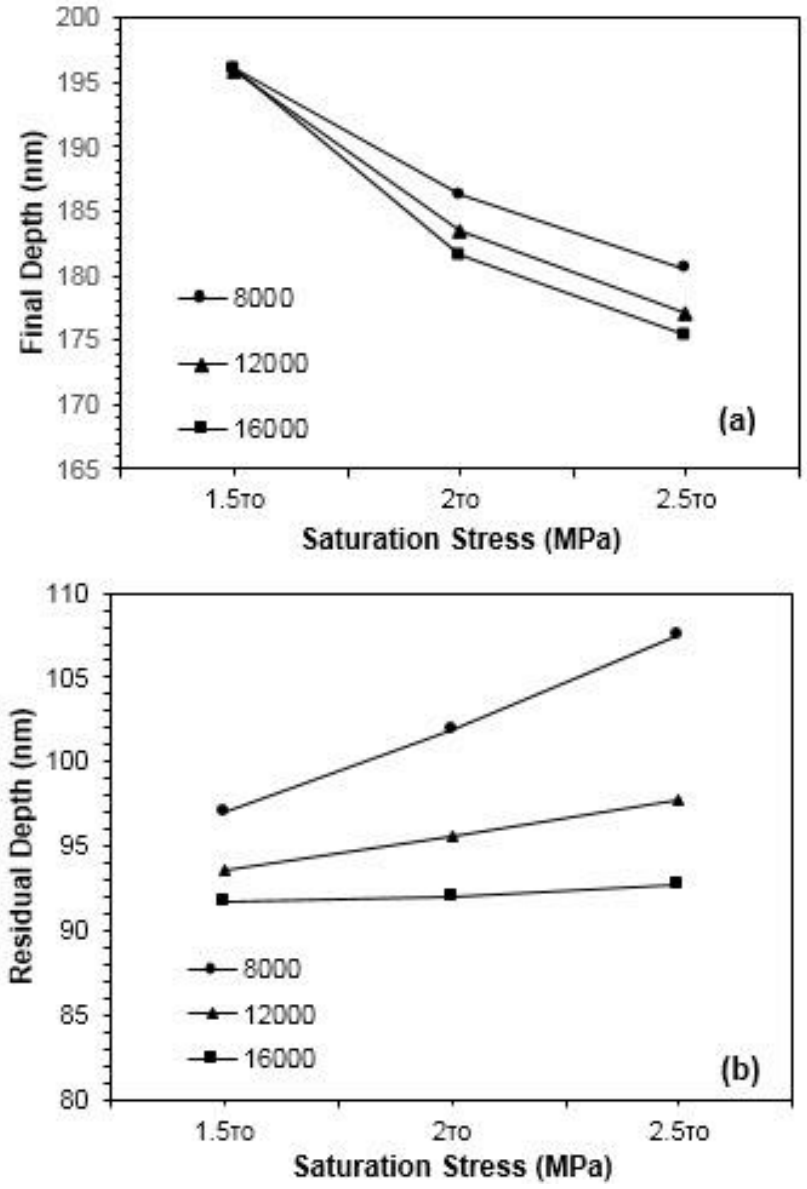

Figure 3-6 : Effects of saturation stress on (a) final indent depth, and (b) residual indent depth of load-displacement curve.

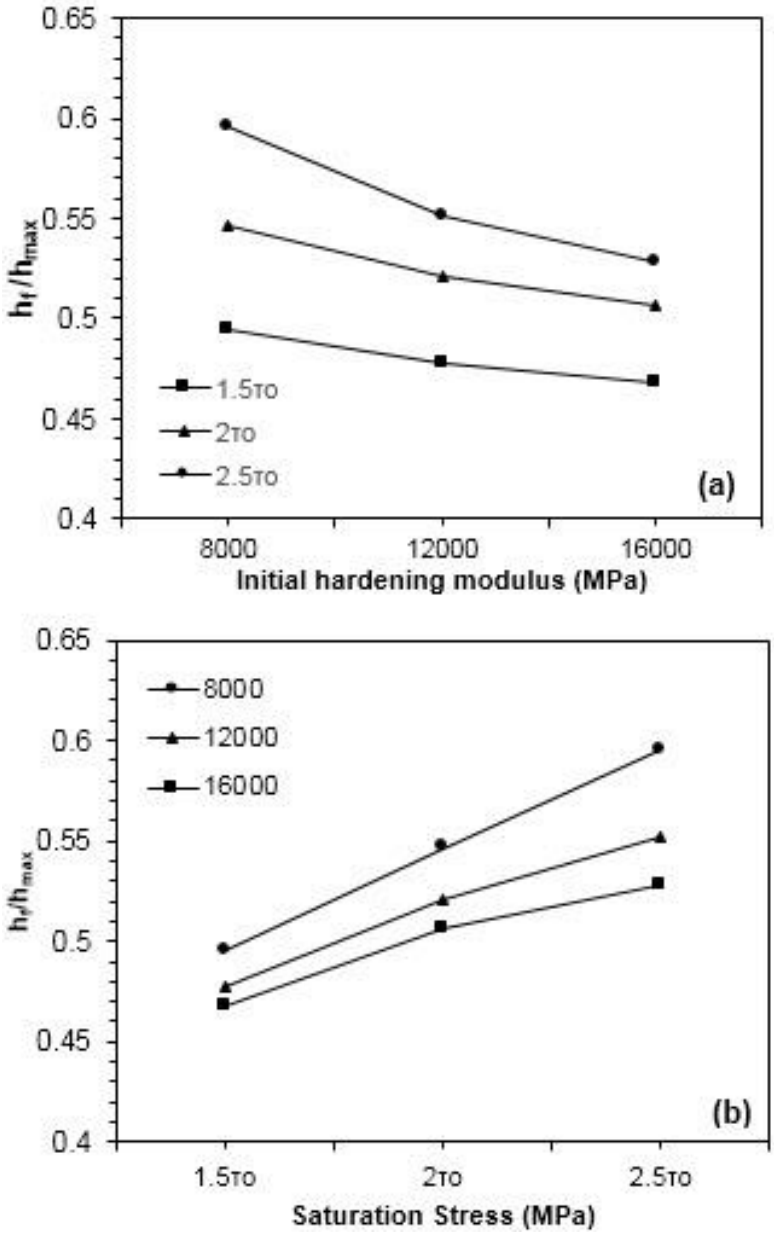

Figure 3-7 : Changes in penetration depth ratio (h_f / h_{max}) of load-displacement curves with respect to (a) initial hardening modulus,and (b) saturation Stress.

3.5 Results and Discussion

Crystal plasticity model parameters calibration were performed to fit the simulated nanoindentation load-displacement curve with the experimental average load-displacement curve. Table 3-3 contains the calibrated model parameters that have been utilized to generate similar load-displacement behavior of Cu_6Sn_5 single crystal.

Table 3-3 : Calibrated model parameters.

Critical resolved shear stress τ_{crss} (MPa)	**Initial hardening modulus h^o (MPa)**	**Saturation stress τ_s (MPa)**
Basal <a>= 260 Prismatic <a>= 1500 Pyramidal <a>= 1310	12000	$2.5\tau_{crss}$

CPFE results shows a good fit with the experimental curves at the loading portion. However, the simulation results give a higher unloading stiffness than the experimental results. It can be attributed to the differences in Young's modulus. Unloading curve depends on the elastic recovery of the indented material [91]. Lee [117] calculated the stiffness matrix of Cu_6Sn_5 using first principles calculation method which has been used in this model. These values result in average Young's modulus of 119 GPa which is higher than our experimental value (116.4 GPa).

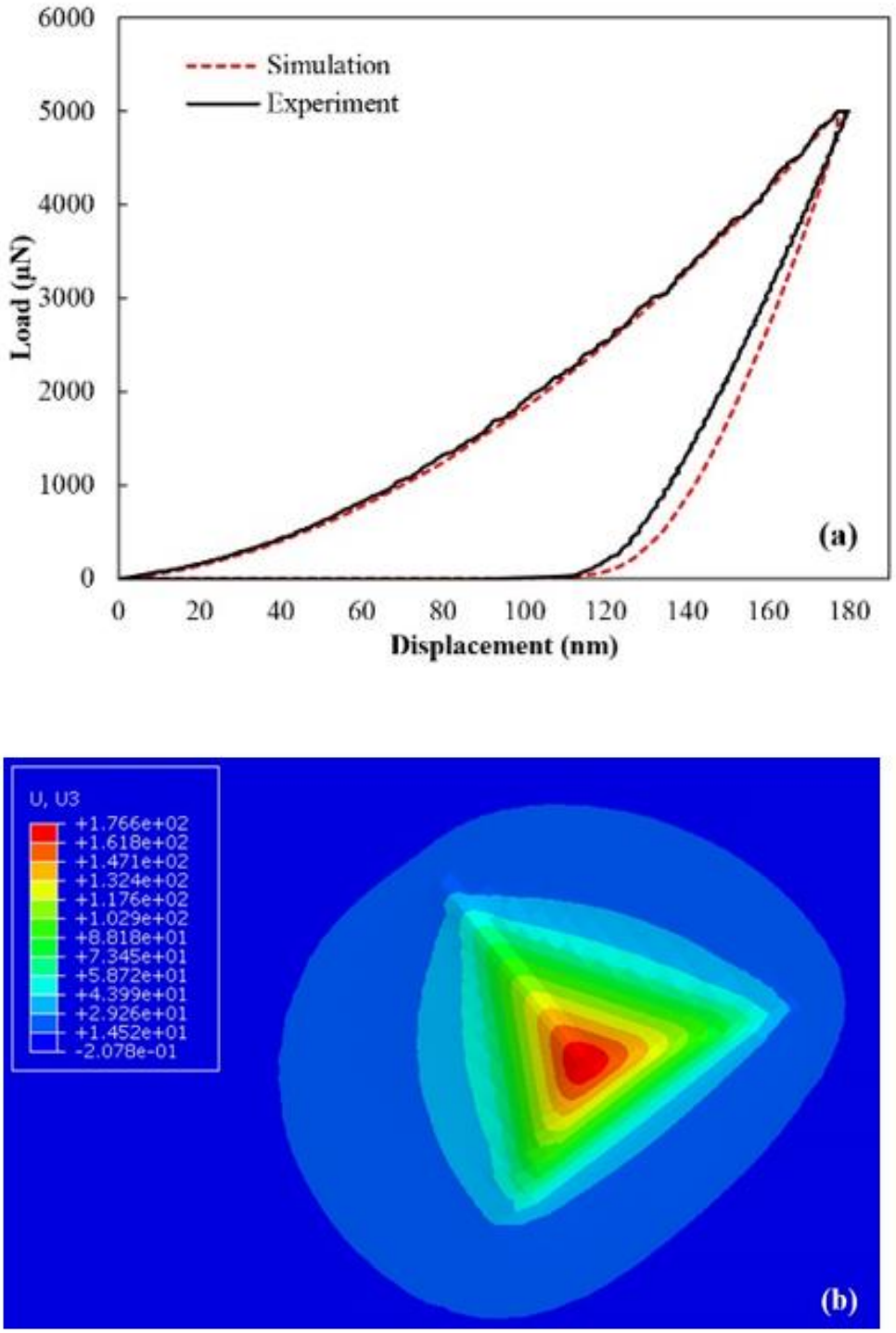

Figure 3-8 : (a) Comparison between load-displacement curves obtained through experiment and simulation, and (b) contour plot of displacement under the indenter at maximum load.

Figure 3-9 contains the von Mises contour plot at the maximum load. Maximum Mises stress was observed to be beneath the indented surface. It can be explained from the view of contact mechanics that maximum stress concentration occurs at a distance beneath the contact surface [122]. Also, the maximum stress area was shifted to right from the center of the indent axis. This is due to the anisotropy of the Cu_6Sn_5. Similar behavior was also reported for other anisotropic materials [123,124]. Maximum von Mises stress was observed to be 20.51 GPa at maximum load of 5000 µN.

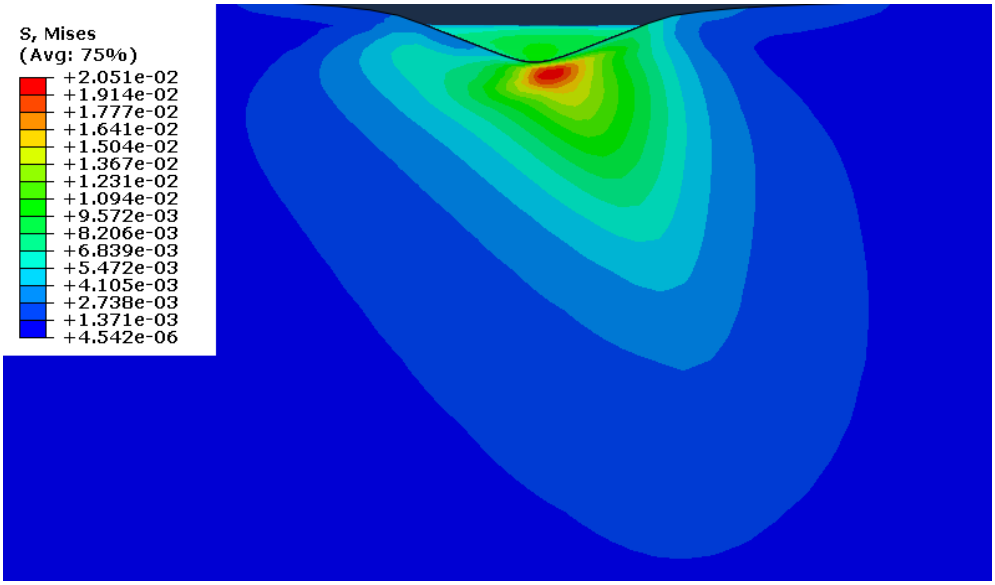

Figure 3-9 : Contour plot of von Mises stress at maximum load. Stresses are in $x10^{-3}$ GPa.

3.6 Validation of the Model

Very few experiments has been conducted on Cu_6Sn_5 single crystal. Ghosh [125] experimented with bulk Cu_6Sn_5 material and published the elastic and shear properties of the material. Zhang [126] experimented on Cu_6Sn_5 single crystal using nanoindentation to capture the shear strength. They removed the bulk solder by corrosion to expose Cu_6Sn_5 and conducted

nanoindentation experiment on Cu_6Sn_5 single grain. They reported the first stage of shear strength when the first strain burst occurred. Jiang [22] also investigated the compressive behavior of Cu_6Sn_5 single crystal by micro pillar compression testing. They observed the fracture behavior and concluded the compressive strength to be the stress at the first strain burst.

To validate our modeling results and the constants projected by our indentation model, a simple block shear test simulation was conducted to determine the shear yield strength and shear modulus of Cu_6Sn_5 single crystal using CPFE simulation. Shear load has been applied perpendicular and parallel to *c-axis* to capture the elastic-plastic anisotropy effects of the material. Values of shear yield strength and shear modulus have been obtained from the shear stress-strain curve generated from simple shear test (Figure 3-10). Simulation of load applied perpendicular to the *c-axis* showed higher shear modulus (33.2 GPa) but lower shear yield strength (410 MPa) compared to shear modulus and shear yield strength of 31.50 GPa and 450 MPa observed for load applied parallel to *c-axis*. The difference in shear modulus is due to the elastic anisotropy of the material. A shear modulus of 35.90 GPa was observed by Ghosh [125] experimentally in polycrystalline Cu_6Sn_5. Zhang [126] observed a shear strength of 670 MPa. Crystallographic orientation of the tested grains has not been reported by Zhang as it may considerably affected the shear strength. Also, in our model, we did not consider slip strength enhancement due to dislocation lock in the grain boundaries as well as other defects which effect the slip behavior significantly. Test conducted with loading direction perpendicular to the *c-axis* has the shear direction parallel to the basal slip direction which has lower critical resolved shear stress. Therefore, it shows lower shear yield strength as it activates the basal slip system readily.

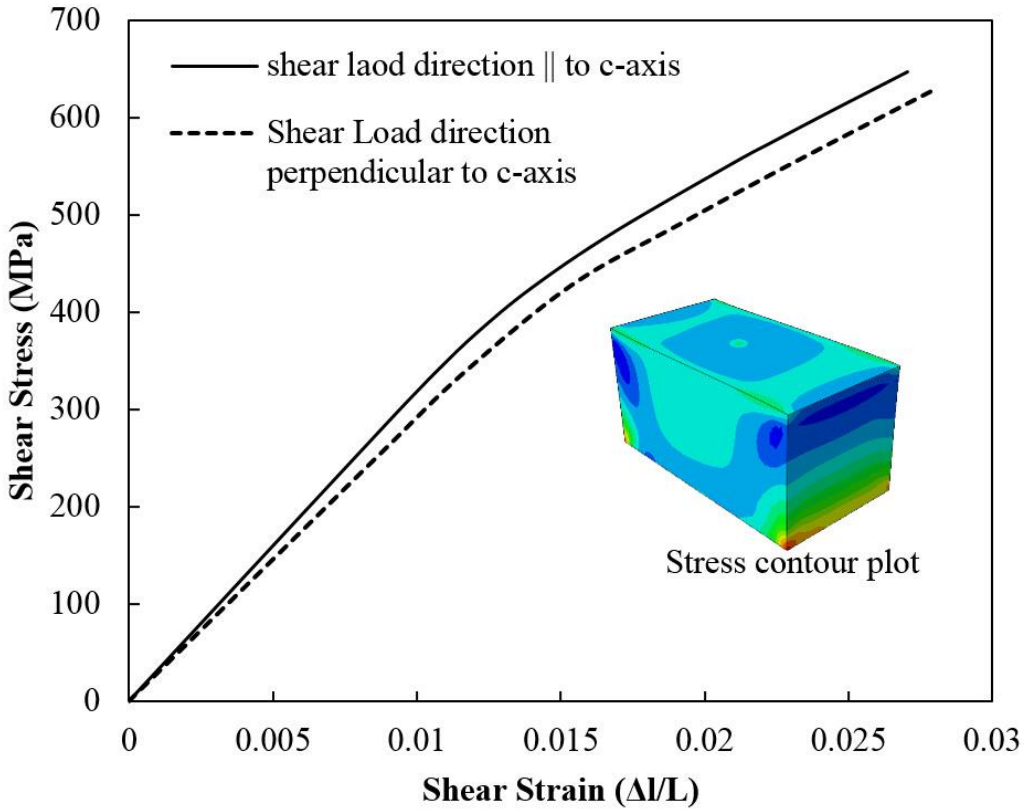

Figure 3-10 : Shear stress-strain curve of the simulation for two different shear load direction.

3.7 Summary and Conclusions

Single crystal plasticity finite element analysis, along with nanoindentation experiment was utilized to generate a set of crystal slip model parameters which can reflect the inelastic mechanical deformation of Cu_6Sn_5 single crystal. Using Schmid factor and yield strength of Cu_6Sn_5 single crystal, CRSS of the slip systems were found to be 260 MPa for basal, 1500 MPa for prismatic and 1310 MPa for pyramidal slip planes. A nanoindentation simulation model was established and curve fitting method was utilized to predict two unknown model parameters i.e., initial hardening modulus and saturation stress. It was observed that a value of

12000 MPa as initial hardening modulus and $2.5\tau_{crss}$ MPa as saturation stress can generate similar load-displacement curves.

Effects of initial hardening modulus and saturation stress on load-displacement curves of single crystal with *c-axis* perpendicular to the indentation loading direction have been described. The relationship between the slip parameters and final indent depth was also discussed. Furthermore, the effects of these parameters on unloading portion of the P-h curve were evaluated using penetration depth ratio.

To validate the values of initial hardening modulus and the saturation stress, a simple shear test model was built and conducted using CPFE. The values of shear modulus and shear strength obtained through this model were compared with values obtained through similar simple experiments in literature. Simulation tends to give a shear modulus of 33.20 GPa for loading direction perpendicular to the *c-axis* and a value of 31.50 GPa for shear loading direction parallel to the *c-axis* which are compared with the values published in literature. On the other hand, shear yielding starts to occur at 410 MPa for the single crystal with c- axis oriented perpendicular to the loading direction. Crystal with c- axis oriented parallel to the loading direction shows a shear yield strength of 450 MPa.

This study uses a constitutive model and presents a base to evaluate the anisotropy and inelastic deformation of Cu_6Sn_5 by reporting crystal plasticity model parameters and by predicting the slip behavior.

CHAPTER 4 : CPFE Model Generation for Whole Solder Joint: Application to Local Shear Behavior Analysis

4.1 Introduction

In this study, CPFE simulation technique is used to model the whole joint including Cu, Sn solder and Cu_6Sn_5 IMC material. Experimental lap-shear test results for solder joint from the literature are used to validate the models. A comparative analysis between traditional FE analysis, CPFE and experiment is conducted. It was found that CPFE model could correlate the experiment more closely compared to traditional FE analysis because of its ability to capture the micro-mechanical anisotropic behavior. Further analysis is conducted to evaluate the effects of IMC thickness on the stress distribution in micro-bumps using a systematic numerical experiment with IMC thickness ranging from 0% to 80%. The analysis is conducted on micro-bump with single crystal Sn and bicrystal Sn.

4.2 Materials Properties Parameters

In this study, both conventional FE and CPFE analyses were performed for different sections. Material properties for FE analysis were consistent with all FE analysis. Similarly, CPFE parameters were kept constant for all CPFE analysis.

4.2.1 FE model Parameters

To investigate the differences in conventional FE and CPFE analysis in predicting mechanical performance, the same geometrical model is used for both FE and CPFE analysis. In the regular FE model, Cu is assumed to be elastic and isotropic. The solder and Cu_6Sn_5 IMC are taken to be linearly isotropic up to the yield point. After the yield point, solder and IMC follow the plastic behavior described in Table 4-1. The elastic-plastic properties used in FE analysis are listed in Table 4-1. Commercially available finite element program ABAQUS [127] is utilized for both FE and CPFE analysis.

Table 4-1 : Material properties used in FE analysis

Material	**Elastic Modulus (GPa)**	**Poisson's ratio**
Cu [47]	114	0.31
Solder alloy [47]	48	0.36
Cu_6Sn_5 [106]	116	0.31

Material		**Plastic Constants**
Solder alloy	***Yield Strength*** 21.5 MPa	***Flow region*** Stress, $\tau = 37*\varepsilon^{0.075}$ where ε is the strain from 0.001 to 0.016. After this point, solder becomes perfect plastic [128]
Cu_6Sn_5	***Yield strength*** 2700 MPa	***Flow region*** Perfect Plastic

4.2.2 CPFE model Parameters

Cu_6Sn_5 is the main IMC component that must form in any successful joint. Previously, Cu_6Sn_5 elastic stiffness constants were calculated by resonant ultrasound spectroscopy (RUS) and published by Jiang et al. [129]. On the other hand, CPFE plastic model parameters for Cu_6Sn_5 IMC were previously computationally generated and reported by Choudhury et al. [130]. CPFE model parameters for bulk Sn were taken from the literature [72,97]. Mostly active slip systems for Sn and Cu_6Sn_5 that are taken into consideration in this analysis are shown in Table 4-2. The stiffness matrix for Sn and Cu_6Sn_5 are provided in

Table 4-3. A small reference shearing rate of $0.001sec^{-1}$ is assumed in this approach as a quasi-static reference. This assumption is a convenient fitting method where reference values can be taken from quasi-static test process [119]. All other parameters are listed in Table 4-4. Cu is assumed to be polycrystalline and taken as an isotropic material. Its properties are kept similar to that of FE analysis. Commercially available FE software ABAQUS in combination with an extended user material subroutine **(UMAT)** was used for the CPFE simulations.

Table 4-2: Slip system for considered materials

Set Number	**Slip System**	**# in family**
	Sn (Tin)	
1	{100) <001]	2
2	{110) <001]	2
3	{100) <010]	2
	Cu_6Sn_5 IMC	
1	Basal {0001} <11$\bar{2}$0>,	3
2	Prismatic {10$\bar{1}$0} <11$\bar{2}$0>	3
3	Pyramidal <a> {10$\bar{1}$1} <11$\bar{2}$0>	6
	Cu (Copper)	
1	{111} <110>	12

Table 4-3: Stiffness matrix for considered materials

Stiffness Matrix (MPa)
Cu_6Sn_5 IMC [129]
C_{11}=96500, C_{22}=96500, C_{33}=96500, C_{44}=32100, C_{55}=32100,C_{66}=32100, C_{12}=32400, C_{13}=32400, C_{23}=32400
Sn (Tin) [72]
C_{11}=72300, C_{22}=72300, C_{33}=88400, C_{44}=22000, C_{55}=22000, C_{66}=24000, C_{12}=59400, C_{13}=35800,C_{23}=35800

Table 4-4: CPFE model parameters

	τ_{crss} (MPa)	τ_s (MPa)	h^o (MPa)	n	q
Sn (Tin) [71]	23	40	100 [set 1,2] 150 [set 3]	10	1.4
Cu_6Sn_5 [130]	260 [set 1] 1500 [set 2] 1310 [set 3]	$2.5\tau_{crss}$	12000	12.2	1
Cu [97]	60.8	109.5	541.5	10	1

4.3 Model Validation

A lap-shear joint test experiment performed by Chawla and group [47,65] was selected to validate the CPFE model. They performed lap-shear tests on different solder joint thickness specimens, and also performed FE analysis to further analyze their results. The test was mimicked exactly to compare the FE responses with the shear test results. Two Cu substrates, with a width of 6.35 mm, a length of 8.175 mm and a height of 6.35mm were soldered with Sn-3.5Ag solder alloy with varying joint thicknesses. The solder region was of 6.35 mm x 6.35 mm. In the experiment performed by Chawla et al., shear responses were recorded at the far-field end using extensometer, and at solder joint region using a thin line created on the joint and tracking the displacements of the line. The tests were performed at ~0.001/s far-field shear strain rate. The described dimensions of the joint in the study were used to create a

computational model (Figure 4-1). Solder joints with a thickness of 520 μm and 120 μm were selected in this numerical experiment. Both models, 520 μm and 120 μm had the same shear strain that was achieved by applying different displacement load for the same time. Element type C3D8R was used to generate the FE mesh, where stress based mesh sensitivity analysis was performed to achieve an optimum model.

Solder and Cu_6Sn_5 IMC were considered as a single crystal in CPFE analysis for simplification without considering variation in crystallographic orientation in this validation model. The *c-axis* of Sn was considered to be oriented along the shear loading axis. Previously, it was observed that Cu_6Sn_5 grows along *c-axis* which is normal to the solder/Cu surface [106]. Similar orientation was considered for Cu_6Sn_5 where *c-axis* was oriented normal to the solder/Cu surface. Due to the large scale of the model, the inclusion of IMC roughness would arise complexity. Thus, for simplification and lack of computational time, the roughness of IMC morphology was not taken into consideration. CPFE analysis was performed with 20% IMC and without IMC to capture the effects of the presence of IMC on the shear behavior of solder joint.

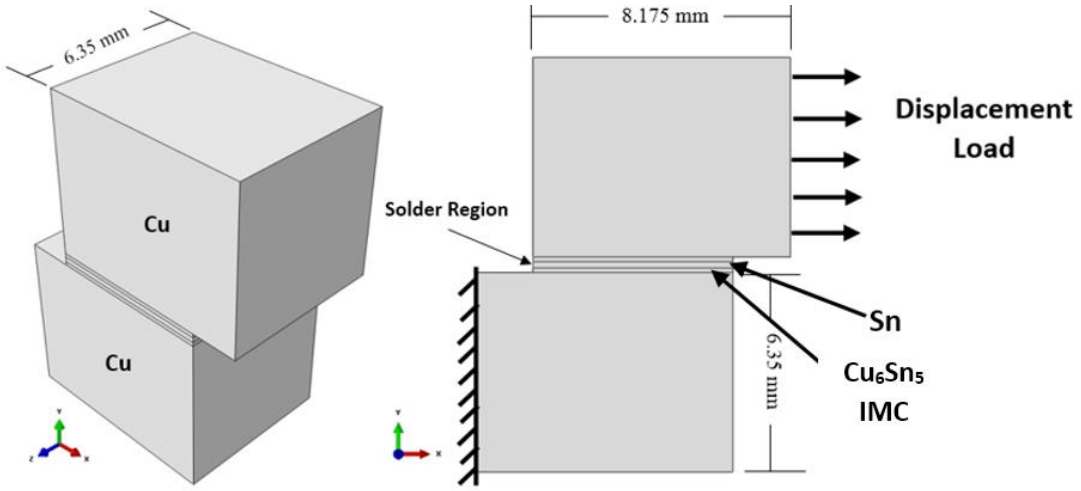

Figure 4-1 : Schematic model of the joint, with applied boundary conditions. Dimensions are not in scale.

4.3.1 Validation Results

Figure 4-2 shows a plot of shear strain vs. time. The far-field shear strain is almost linear with time, as prescribed by the applied shear strain rate. However, in the experiment, a lower non-linear shear strain was observed in the solder region. The divergence is due to the deformation associated with Cu and fixture, etc. In FE models, to measure the actual shear strain at the joint area, the displacements at the nodes in solder region area are taken into consideration and then averaged to get the average local shear strain. CPFE results show slightly higher values compared to the actual local shear strain measured optically *in situ*, although local shear strain accumulation rate is similar to both experiment and CPFE analysis. Initially, the slow buildup of shear strain is seen where solder behaves elastically. After a time, solder starts to deform plastically, and the local shear strain rate becomes higher. The smaller discrepancies between experimental and CPFE model may have been caused by several factors such as consideration of single crystal for both solder and IMC, variation in input parameters, etc. Cu substrate

dimension is large enough to have many grains that it may behave as an isotropic bulk material. To keep consistency with other analysis performed later in this study, all materials were modeled with CPFE material parameters presented in Table 4-2 to Table 4-4.

Local shear strain response extracted from the traditional FE analysis follows far-field shear strain response more closely. As, FE analysis is unable to capture the intrinsic material deformation mechanism, the shear strain response with respect to time is not able to predict the actual local shear strain behavior that was measured optically in the experiment.

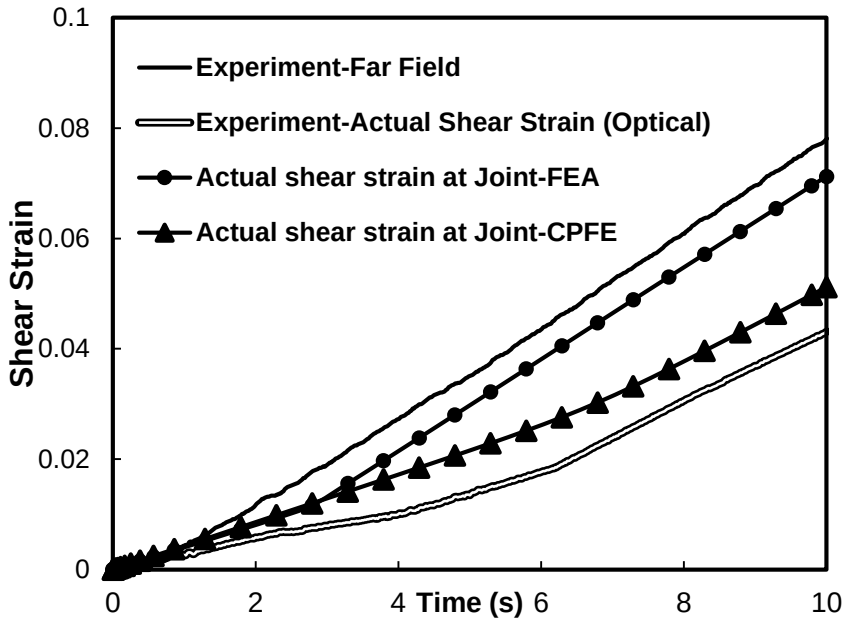

Figure 4-2 : Shear strain vs. time for 120μm solder joint. Data for experimental far field, and actual shear strain measured optically was reproduced. [47]

To compare the shear stress-strain response in experimental findings and finite element analysis, shear stress vs. far-field shear strain was plotted. Shear stress was calculated dividing the applied load by solder pad area. Figure 4-3 shows the shear stress-strain responses for 120

μm thickness joint. The simulation results show slightly different slope in the elastic region compared to the experimental results. The predicted shear yield strength in CPFE model shows similar values compared to experimental results. However, when 20% IMC was included in the model, the result showed a stiffer response. This phenomenon is due to the different mechanical properties of Cu_6Sn_5 IMC that has a relatively stiffer elastic response with higher yield strength. The analysis shows that overall hardening behavior of the joint increases with the inclusion of IMC in the model. However, CPFE model can predict the qualitative elastic-plastic behavior of the solder joint successfully.

Traditional FEA shows lower yield strength values than the apparent experimental yield strength. This is due to the differences in intrinsic material behavior of small-sized solder than bulk solder input material properties.

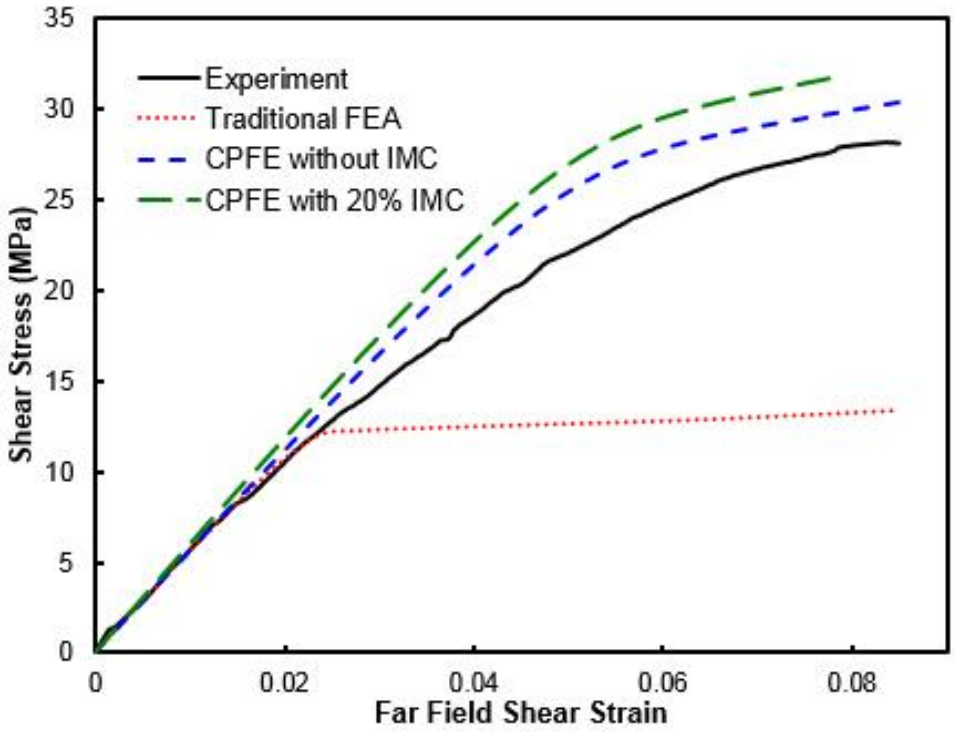

Figure 4-3 : Shear stress vs. far field shear strain for 120µm solder joint. Figure contains the shear response extracted during traditional FEA, CPFE modeling with and without IMC, and experimental finding. Experimental data was reproduced from reference [47]

Similar analysis has been conducted for 520 µm thickness joint, and Figure 4-4 contains the shear stress-shear strain response. The effects of 20% Cu_6Sn_5 IMC inclusion shows higher changes in apparent stiffness compared to the effects on 120 µm thickness joint. Chawla et al. did not provide any information regarding the IMC thickness in the solder joint. However, the model with 20% IMC shows the almost identical experimental response. Traditional FE provides less yield strength compared to the experiment.

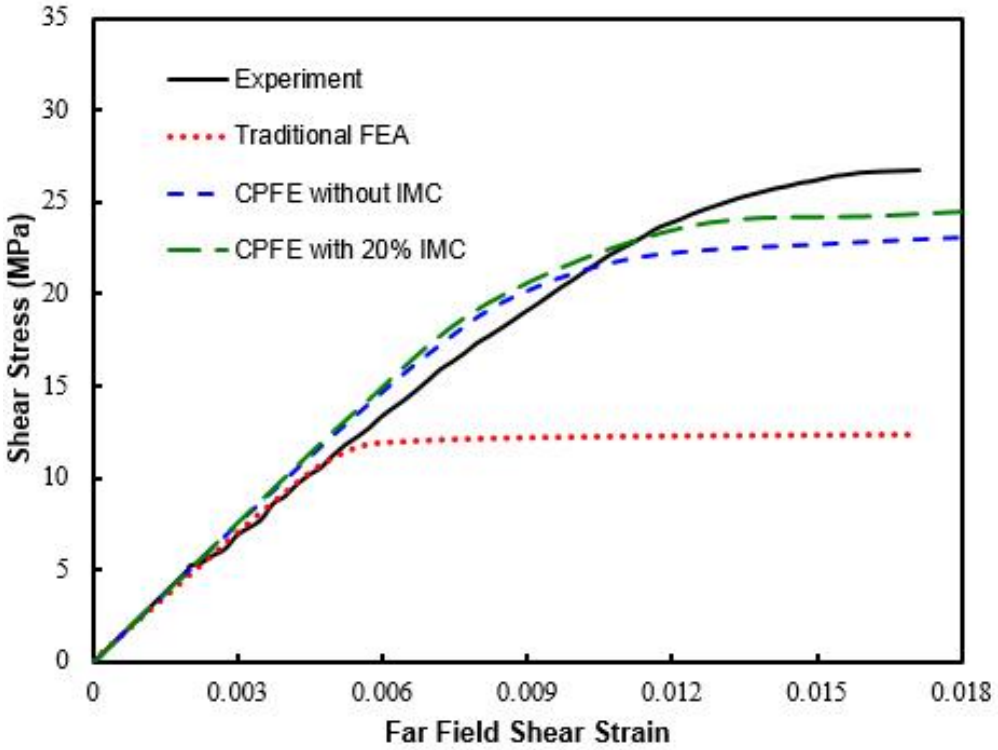

Figure 4-4 : Shear stress vs. far field shear strain for 520µm solder joint. Figure contains the shear response extracted during traditional FE, CPFE modeling with and without IMC, and experimental finding. Experimental data was reproduced from reference [47]

An important finding of Chawla et al. [65] was the shear behavior of solder joints with different joint thickness. With the increasing solder joint thickness, the joint shows higher apparent stiffness. It was concluded by Chawla and group that at the lower thickness, the deformation transmits through both normal and shear components. With the increase in joint thickness, the shear component becomes more dominant and provides a stiffer shear response. To investigate this finding, shear stress-strain response in CPFE analysis for both 120 µm and 520 µm thickness joint are plotted in Figure 4-5. As seen in this figure, CPFE shows a similar trend. Thicker solder joint provided stiffer shear response where thinner joint shows less stiff performance. Figure 4-6 shows the in-plane shear stress contour plot for these joints at a 0.020

far-field shear strain. It is evident in CPFE analysis that thicker solder joint shows higher shear stress at the solder area. On the other hand, in-plane shear stress at thin solder joint is almost continuously distributed with little higher in-plane shear stress at the corner. Thinner solder joint behaves as a Cu-solder-Cu assembly where the shear stress is distributed in the whole assembly. In-plane shear strain is large at the solder region at thicker solder joint, indicating that large deformation occurs at solder region for thicker solder joint. A relatively distributed in-plane logarithmic shear strain is found for thinner solder joint indicating mechanical load diffused through greatly constrained joint without inducing large shear strain in solder region. The findings in this model are supported by the numerical results published by Shen et al. [65] and Chawla et al. [47]. The model is able to capture the geometric effects where thicker joint shows higher stiffness and thin joint shows lower stiffness.

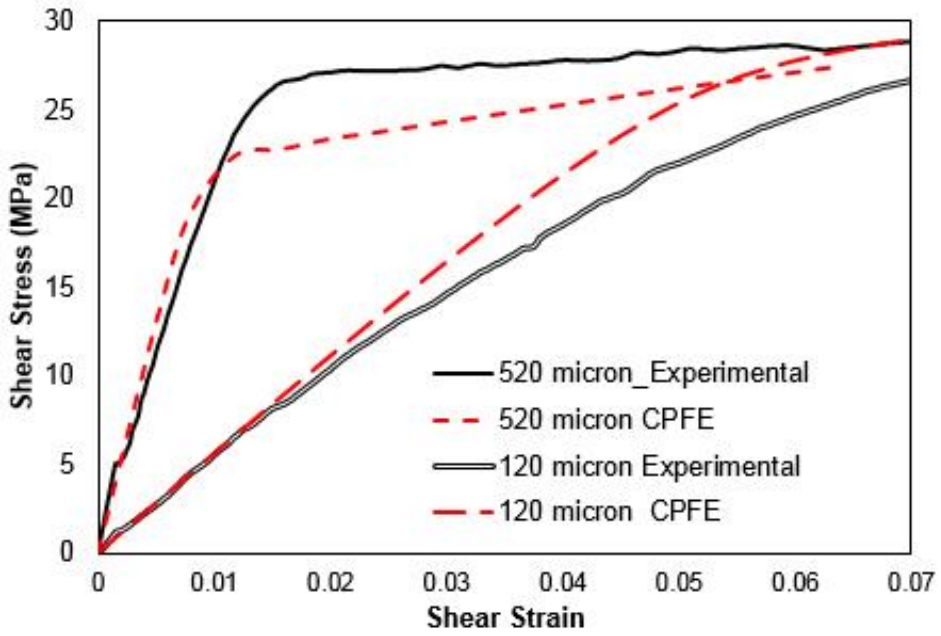

Figure 4-5 : Comparison of shear stress-strain responses for 520µm, and 120µm solder joint. CPFE model contains no IMC here for simplification. Experimental data was reproduced from reference [22]

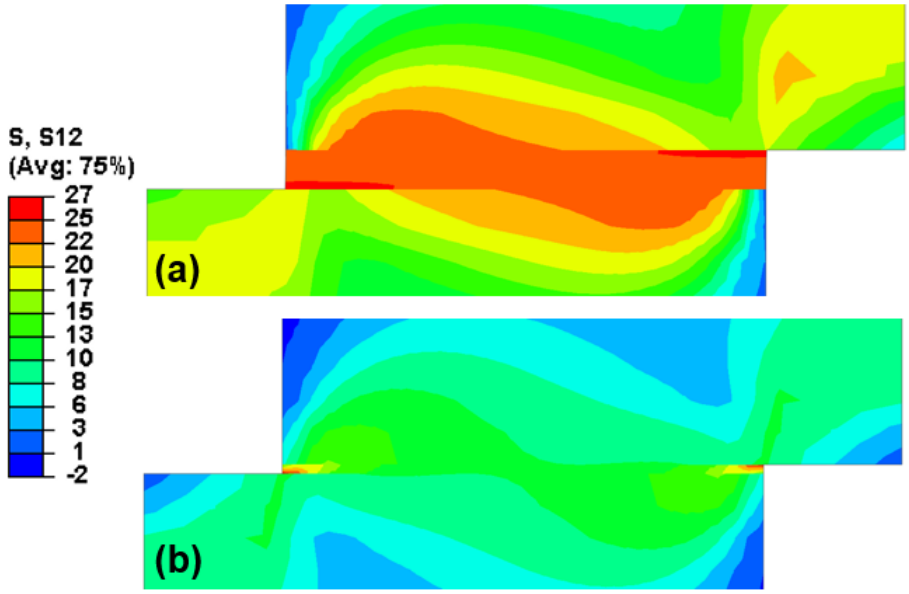

Figure 4-6 : In-plane shear stress (in MPa) contour plot for (a) 520µm and (b) 120µm solder joint, at a shear strain of 0.020. The contour plots are showing a portion of Cu substrate to focus largely on the joint.

4.4 Effects of IMC thickness through CPFE

4.4.1 Model Generation

A simple shear specimen was selected to conduct the CPFE analysis. A square block of 100 µm x 100 µm x 100 µm of solder material was sandwiched by two blocks of Cu material of 100 µm x 100 µm x 50 µm. (Figure 4-7). Upper and lower blocks were assigned to Cu material properties for CPFE analysis. Solder material properties were allocated to the middle block. Middle block was considered as one crystal for single crystal Sn analysis. To investigate bicrystal Sn, the middle block was divided into half, and different crystallographic orientations were assigned to two parts. Generally, Cu_6Sn_5 IMC exhibits scallop type microstructure. To take IMC into consideration and simplify the model, Cu_6Sn_5 IMC was modeled as three half cylinders. These half cylinders were grown at the solder/Cu interface to change the thickness

of IMC. Three different IMC thickness of 20 µm, 40 µm, and 80 µm were considered to analyze the effects of IMC thickness on the shear behavior of the solder joint.

The bottom surface of the model was fixed in all direction while the displacement load was assigned to the top surface to introduce the shear loading (Figure 4-7a). Same displacement load was assigned for all models to have similar shear strain rate so that a comparative analysis could be conducted. The whole assembly meshed with C3D8R element, and stress-based mesh sensitivity analysis was performed to find the optimum mesh size.

Shear stress for all analysis was calculated dividing the applied load by the solder pad area which is $0.01m^2$. Shear strain was obtained by the conventional relation of displacement divided by the joint thickness.

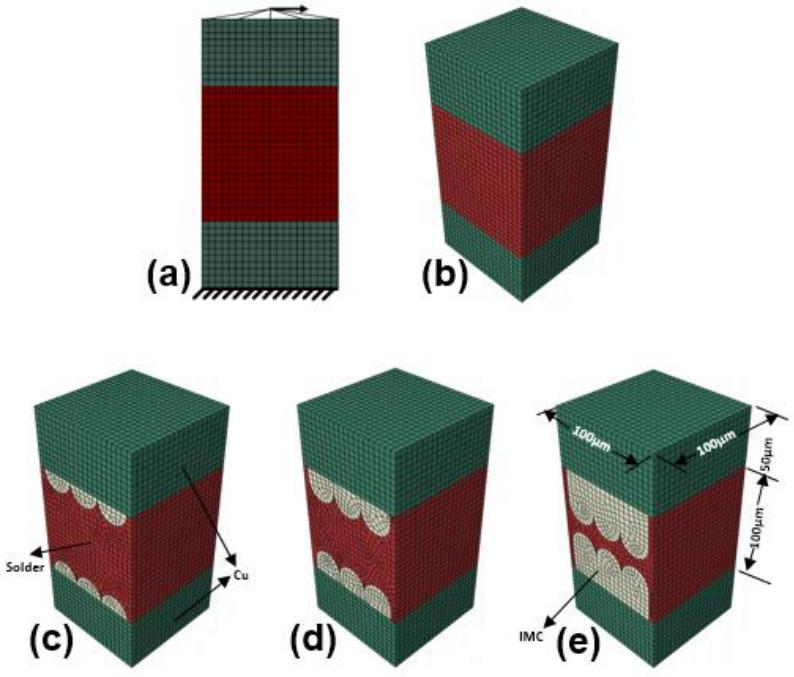

Figure 4-7 : Meshed model, showing (a) boundary conditions, and models with different IMC thicknesses such as (b) No IMC, (c) 20µm IMC, (d) 40µm IMC, and (e) 80µm IMC.

4.4.2 Model Results for Single Crystal Sn

For this analysis, single crystal Sn with *c-axis* oriented towards the loading direction is considered as, it is statistically the most common crystallographic orientation observed for single grain Sn in solder joints [131,132]. Sn crystal tends to grow along <110] direction which is the preferred grain growth direction [133]. When the heat flows from the substrate to substrate during the reflow process, <110] direction follows the heat flow direction which is perpendicular to the substrate. This phenomenon aligns the *c-axis* [001] parallel to the substrate normal which happens to be situated 90° to the <110] direction [134]. Cu_6Sn_5 IMC thicknesses were varied among 20µm, 40µm, and 80µm (Figure 4-7). Shear stress-strain was plotted in Figure 4-8 (solid lines). It has been observed that with the increase in IMC thickness, solder joint provides stiffer response and higher shear yield strength. Cu_6Sn_5 has much higher yield strength than Sn. Larger volume ratios of Cu_6Sn_5 has a dominant effect on shear yield strength and increase the overall shear yield strength of the joint. The rigid nature of Cu_6Sn_5 induces larger constraints on the joint and tends to introduce rigid body behavior. Apparently, increase in the presence of stiffer material in the solder joint causes the shear stress-strain behavior to change from "low stiffness-low strain hardening" to "high stiffness-high strain hardening". A Similar effect of IMC thickness on the experimental shear response was reported previously [40,135] although their reported effect was not significant as their specimens were larger. Effects of IMC thickness on the mechanical behavior will be more dominant when the size of the joint goes smaller. Recently, Choudhury et al. [136] performed single lap-shear test on different IMC thickness joints and observed similar behavior where higher IMC thickness contributed to the stiffer responses.

The in-plane shear stress contour plot is provided in Figure 4-9 for four models with different IMC thickness at a 0.02 shear strain. It can be noticed that models with IMC develop higher in-plane shear stress in the solder/Cu_6Sn_5 IMC interface. This could result in crack initiation and growth at the solder/Cu_6Sn_5 IMC interface. Failure in solder/IMC interface has been observed by several researchers [42,137,138]. On the other hand, accumulation of in-plane shear stress in Sn region increases with the increase in IMC thickness. At the same shear strain, the magnitude of shear stress at 80µm IMC thickness joint is two times higher than 20µm IMC thickness joint.

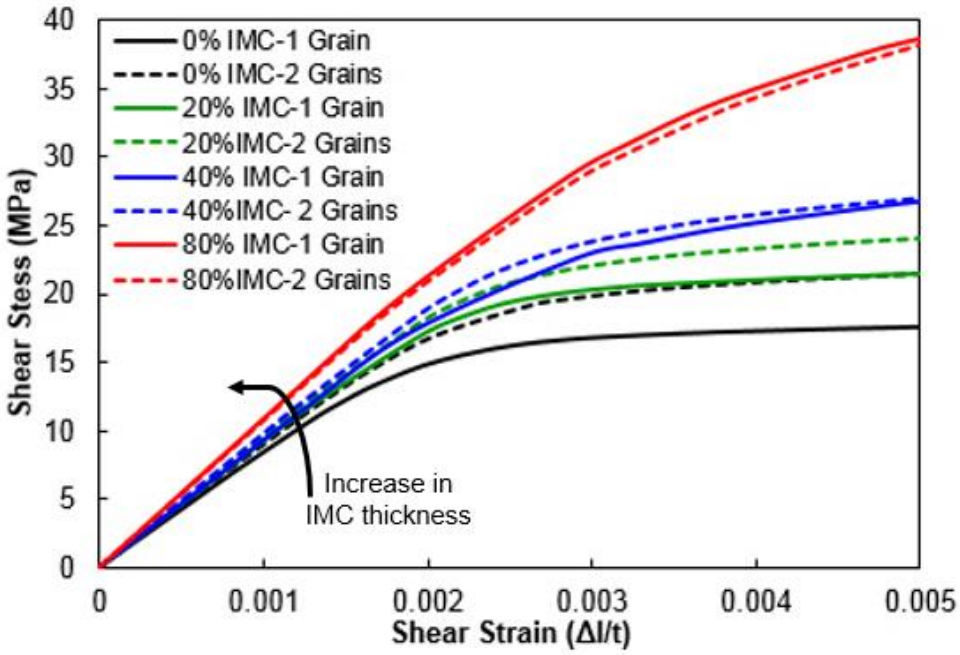

Figure 4-8 : Figure showing effects of IMC thickness on the shear stress-shear strain behavior of single crystal Sn solder joint (solid line), and bi-crystal Sn solder joint (dotted line).

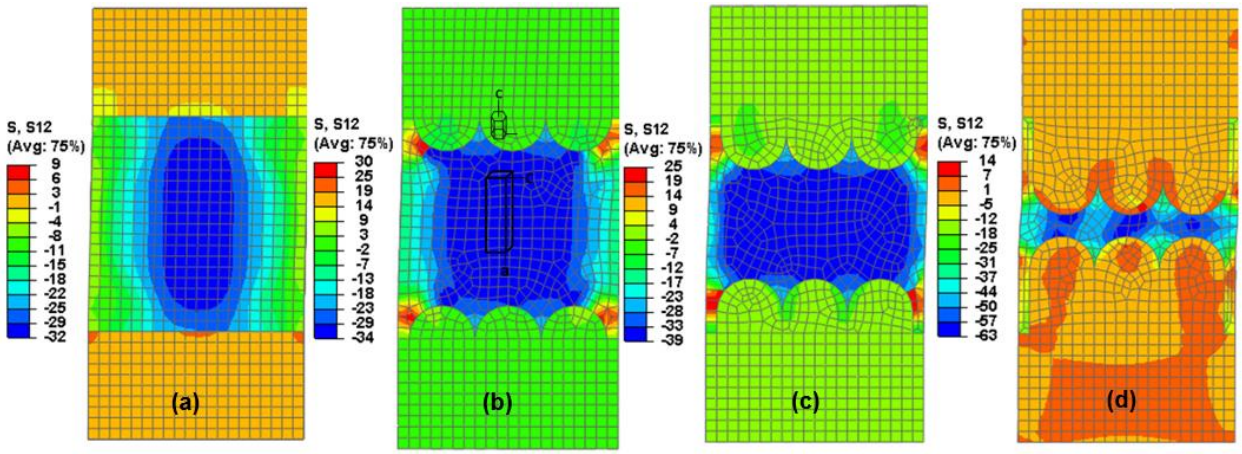

Figure 4-9 : In plane shear stress contour plot for IMC thickness of (a) No IMC, (b) 20µm, (c) 40µm, and (d) 80µm in single crystal solder joint model at 0.02 shear strain. The orientation of the crystals are given.

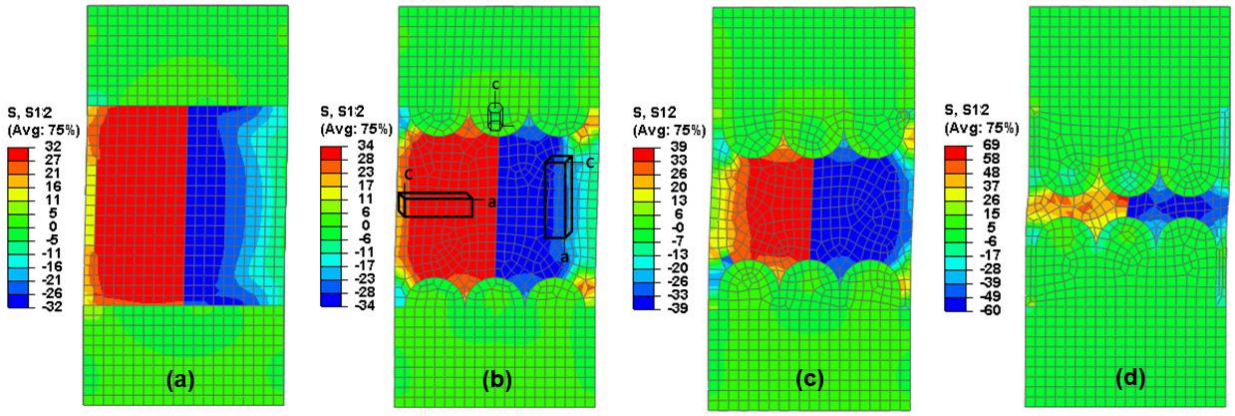

Figure 4-10: In plane shear stress contour plot for IMC thickness of (a) No IMC, (b) 20µm, (c) 40µm, and (d) 80µm in bicrystal solder joint model at 0.02 shear strain. The orientation of the crystals are given.

4.4.3 Model Results for Bicrystal Sn

Two orientations were selected to simulate the bicrystal Sn behavior in the joint. One crystal had its *c-axis* oriented parallel to the shear loading direction, and the other one was oriented in such a way that its *c-axis* was placed perpendicular to the loading direction. The orientation is shown in Figure 4-10. The shear stress-shear strain responses were recorded and provided in Figure 4-8 (dotted lines). It has been observed that bicrystal Sn model without Cu_6Sn_5 IMC

shows a noticeable difference compared to single crystal Sn. However, as the Cu_6Sn_5 IMC thickness increases, the effect seems to diminish, and the shear behavior becomes similar to the single crystal (Figure 4-8). Due to the geometric effects discussed earlier, stiffer response was observed for higher Cu_6Sn_5 IMC thickness joint. At higher Cu_6Sn_5 IMC thickness, the solder joint exhibits stiffer response with higher shear yield strength. The hardening behavior of the solder joint becomes dominated by Cu_6Sn_5 behavior where the plastic shear deformation is achieved at higher shear stresses. Small regions of stress concentrations were found on the hills of the IMCs. Other than that, no continuous higher stress concentration was observed in the solder joint. Overall response for the solder joint was similar to the single crystal solder joint.

4.5 Discussions

Sn has a body-centered tetragonal crystal structure where *c-axis* to *a-axis* lattice parameter ratio, c/a is 0.5456 [139]. The large discrepancy in lattice parameters and the large grain microstructure observed in solder alloys introduce anisotropy. The Young's modulus and coefficient of thermal expansion (CTE) are reported to vary largely with the crystallographic direction [71,73]. To understand the effect of Sn anisotropy on the modeled solder joint, two analysis were conducted on a single crystal Sn with loading direction keeping along *c-axis* and along *a-axis*. A simple cubic block was designed, and Sn crystal plasticity parameters were assigned to it. The crystallographic orientation was changed with respect to the shear loading direction. The shear stress-strain response shows noticeable anisotropic effects (Figure 4-11). The joint provides overall lower shear yield strength when the loading direction is along *c-axis*. Almost 40% increase in shear yield strength is observed when the crystal is rotated, and

a-axis is aligned along with the loading direction. Similar behavior was reported by Darbandi et al. [72] from their shear test simulation. Shear yield strength was lowest in their study when the *c-axis* of the crystal was oriented parallel to the loading direction. The phenomenon becomes clear when we look into the average shear strain in most active slip systems in Sn (Figure 4-12). The shear strain in the slip systems was averaged from the elements in Sn area. When the *a-axis* of Sn is aligned along the loading direction, (100) [010] is the most active slip system and other slip systems do not contribute significantly. Thus, the crystal shows higher stiffness and higher yield strength. On the other hand, in the case of *c-axis* of crystal oriented along the loading direction, multiple slip systems contribute towards the deformation, providing easy deformation. In this case, (100) [001] is the most active slip system and also (110) [001] slip system contribute noticeably.

Effects of the increase in IMC thickness are clearly observed when the elastic regime of the shear stress-strain curve and shear yield strength are compared (Figure 4-8). It is evident that solder joint shows stiffer elastic response when the volume fraction of IMC increases. If we compare the individual elastic stiffness matrices of both Sn and Cu_6Sn_5 given in

Table 4-3, we can see that the Cu_6Sn_5 IMC has a higher stiffness than Sn. Thus, due to the increase in Cu_6Sn_5 thickness, overall solder joint shear behavior tends to show a stiffer response. On the other hand, when joint has a larger volume of Cu_6Sn_5 IMC, shear deformation becomes tougher due to the higher slip yielding properties of Cu_6Sn_5 IMC, resulting overall higher shear yield strength. However, due to the absence of any failure criteria, the plastic regime of the shear stress-strain curve may not be practical. It has been observed in the literature that due to hard and brittleness of the IMCs, joint with a higher volume fraction of

IMCs tends to fail at a smaller strain while joint with thin IMCs provides larger strain to failure [140].

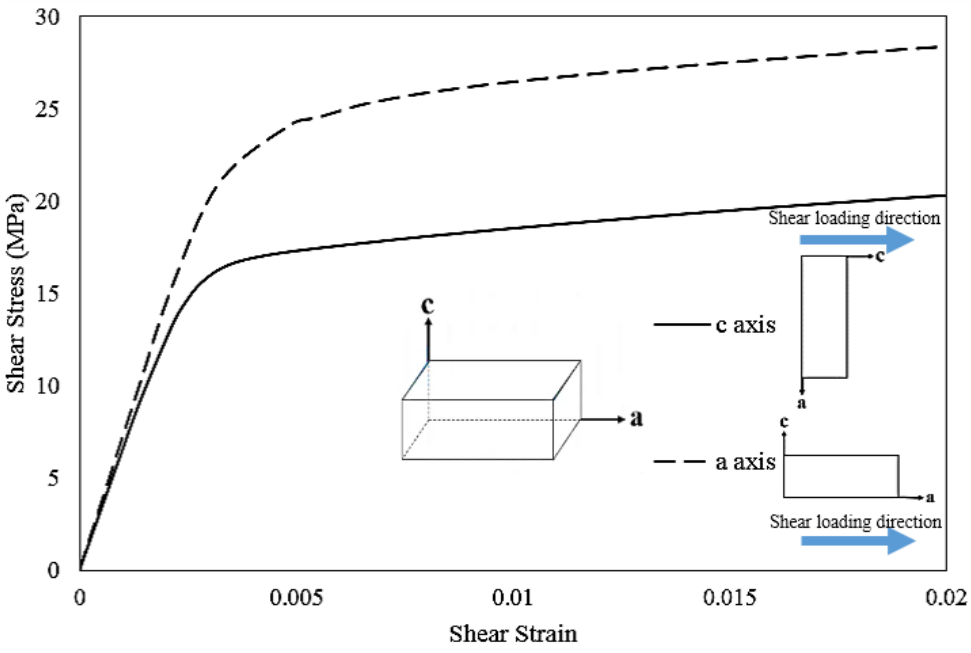

Figure 4-11 : Shear stress-strain response for solder joint with different orientation of Sn. The orientation schematic is provided in the inset.

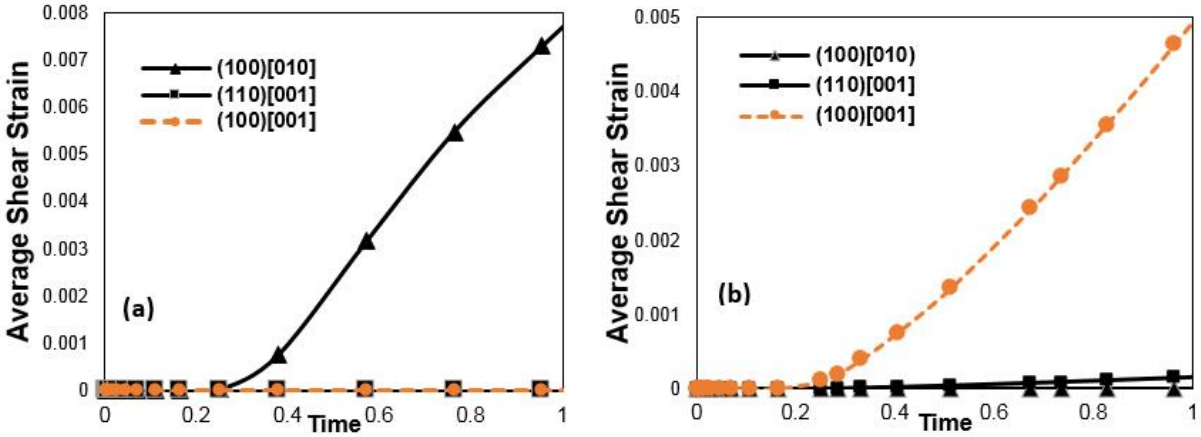

Figure 4-12 : Evaluation of average shear strain in slip systems of Sn in the solder joint, when (a) *a-axis* oriented along the loading direction, (b) *c-axis* is oriented along the loading direction.

4.6 Summary and Conclusions

Interconnect materials have the anisotropic effects due to their crystal structure and large grain microstructure. This anisotropy has a significant effect on the mechanical properties of micro-scale solder joints. Following are the findings observed during this study:

- It has been witnessed that CPFE model performs better than FEA to predict the mechanical behavior of small scale solder joints. CPFE model uses the crystal slip deformation information to predict how materials with few grains mechanically behave. On the other hand, traditional FE model takes bulk material properties into account that leads to an inaccurate prediction of plastic behavior or insufficient results of material behavior in micro scale. A single lap-shear test was selected to validate the CPFE model. The model was able to predict the elastic-plastic material behavior of the overall solder joint.
- Effects of IMC thickness on the shear deformation was also analyzed for solder joints with single and bicrystal Sn. With the increase in IMC thickness, the solder joint gives stiffer shear response while increasing the shear yield strength. When the solder joint has a larger volume of Cu_6Sn_5 IMC, shear deformation becomes harder due to the higher yielding properties of Cu_6Sn_5 IMC, thus giving overall higher shear yield strength.

CPFE model can predict the qualitative behavior of the material more accurately. The model can be utilized as a suitable tool for predicting the mechanical behavior of solder joints and may contribute towards developing solder interconnects with higher reliability.

CHAPTER 5 : Effects of IMC Thickness on the Local Shear Behavior of Micro-scale Solder Joints: *In situ* Single Lap-shear Test

5.1 Introduction

This study was focused on investigating the effects of different volume fraction of IMCs on the shear behavior of micro-scale solder joints with a 50μm stand-off height. A single lap-shear specimen was designed to conduct the study. Two Cu substrates were soldered together with Sn-3.5Ag solder foil and a thickness of 50 μm was achieved. The soldering temperature of 260°C and soldering time of 10, 30, and 60 minutes were utilized to achieve approximately 40%, 60%, and 80% IMCs of total joint thickness. The experiments were conducted using a micro-tensile tester which is integrated with an optical microscope for monitoring and observing deformation in the testing material. To investigate the local shear strain behavior, an optical technique along with a developed image processing computer program was used. The single lap-shear tests were conducted with a shear strain rate of $0.015s^{-1}$ and $0.15s^{-1}$ to observe their effects on shear stress-strain behavior.

5.2 Experiments

5.2.1 Experimental Parameters Selection

Reducing the variables that could affect the shear response was an important step during the experimental design. In general; variation in gap size [42], reflow profile [33], and cooling rate [141,142] tend to affect the shear response of the solder joint due to the change in solder microstructure, morphologies, and IMC growth. The experiment was designed in such a way that the IMC thickness variation would be the only variable that would control the shear response. For this reason, soldering temperature was kept constant to 260°C while soldering time was varied to achieve different rate of Cu dissolution and thus IMC thickness. Similar furnace cooling rate of ~2°C/min was used for all samples to minimize the variation in solder microstructure from sample to sample. The test and specimen design and fabrication process were implemented meticulously to minimize the solder joint thickness variations.

5.2.2 Experimental Procedures

5.2.2.1 Specimen Design and Fabrication

The dimensions of the single lap shear specimen are provided in Figure 5-1-c. Cu sheets were cut into 25.4 mm x 25.4 mm (1 inch x 1 inch) coupon and the selected surfaces for soldering were mechanically grinded using 400, 800, and Micro-cut 1200 (P2500) Grit SiC paper. Then, the surfaces were polished using 0.5µm of Alumina powder (Figure 5-1-a). Sn-3.5Ag solder foil with a thickness of 50.8 microns (.002 inch) was chosen to keep the joint thickness constant. Rosin mildly activated (RMA) flux that has a rosin combined with an activation agent, typically acid, was applied on the soldering area to increase the wettability of metals and removal of oxidation. The solder foil was cut into 3 mm x 25.4 mm coupon and was placed

on one Cu coupon, facing upward (Figure 5-1-a). Then, the other Cu coupon was placed on the top of the solder foil to form a lap solder joint. A spacer was kept under the top Cu coupon to keep it parallel, and a weight of 0.1N was applied on the top of the solder to achieve a uniform solder thickness. The weight was kept constant for all test samples. After that, the specimen was brought into a thermal chamber and soldered at 260°C. 10 mins, 30 mins and 60 mins of soldering time were selected to achieve different IMC thickness at different specimens. The soldered lap shear joint was kept in the chamber after soldering process to cool down slowly at ~2°C/min rate.

After soldering, all specimens were machined and cut into strips of 2 mm thickness using wire electron discharge machine (EDM) with the dimension shown in Figure 5-1-b,c. The sides of the stripped samples were grounded with 800 and Micro cut 1200 (P2500) Grit SiC paper and polished with 0.5 μm colloidal silica. Image of the final specimen is provided in Figure 5-1-d. Then, a solution of HNO_3 + H_2O (1:10) was used to etch the bulk solder to expose the interfacial IMCs.

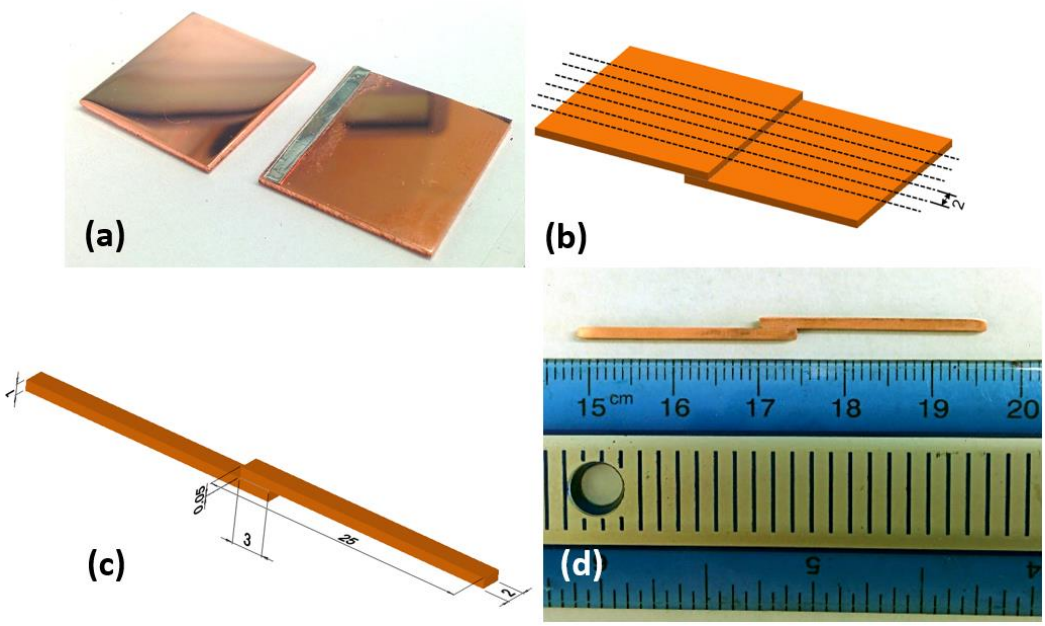

Figure 5-1: (a) Actual Cu coupon with solder foil on one side, (b) Fabricated specimens were stripped using wire EDM, (c) the dimensions and (d) figure of actual sample for single lap-shear test.

5.2.2.2 Single Lap-shear Test

The single lap-shear test was performed in an MTI 1000lb micro-tensile stage at room temperature. The micro-tensile tester has a maximum load capacity of 4500 N with a ±0.2% load cell accuracy and ±20nm linear scale resolution. Three samples for each case were tested. The tests were displacement controlled and to understand the effects of shear strain rates, two different constant displacement rate of 0.05 mm/min and 0.5 mm/min were used to perform the tests. The test speed was limited due to the low camera speed which is described later in this section. The displacement rates provided a far-field or nominal shear strain rate of about $0.015s^{-1}$ and $0.15s^{-1}$ respectively. When a sample is placed into the testing grips, it can be subjected to small compressive forces. The addition of a small preload in the test setup helps to eliminate those compressive forces. A preload of 5N was utilized, and the displacement was

reset to zero when 5N was reached. Load-displacement curves with respect to time were recorded where far-field displacement was obtained from the cross-head movement. The far-field strain was calculated by dividing the crosshead displacement with the joint thickness. Cross-head displacement is the sum of the axial displacement of the Cu and the local shear displacement of the solder. Therefore, the cross-head displacement does not represent the local shear displacement. It is essential to measure the strain locally at the joint area. However, it is not feasible to use strain gauge and extensometer in a joint of 50 µm thickness with a 3 mm x 2 mm region of interest. To observe the induced local displacements in the solder joint, an optical measuring technique was utilized. A straight line normal to the solder joint was scribed 1.5 mm far from the both joint edges covering the Cu substrates and solder joint with a scriber. The thickness of the scribed line was about 25µm. This line thickness is very small compared to the width of the joint (3 mm) and assumes to have an insignificant effect on the overall shear stress-strain behavior of the joint. An optical microscope was used to monitor and capture the video of the changes in displacements of the scribed line while the test was running. The optical camera had a 10fps (frames per second). The video was analyzed by an image processing program written in MATLAB to capture frames at 5-sec interval for $0.015s^{-1}$ tests and 1-sec interval for $0.15s^{-1}$ tests. With the help of MATLAB, the captured images were then converted to binary images, examined, and the axial displacements of the line were calculated for each frame and correlated with the test time (Figure 5-2). A detailed description of the developed technique is provided in **Appendix C.**

After the lap-shear test, the fracture surface characterization studies were conducted on a Scanning Electron Microscope (SEM) to investigate the failure modes and mechanism.

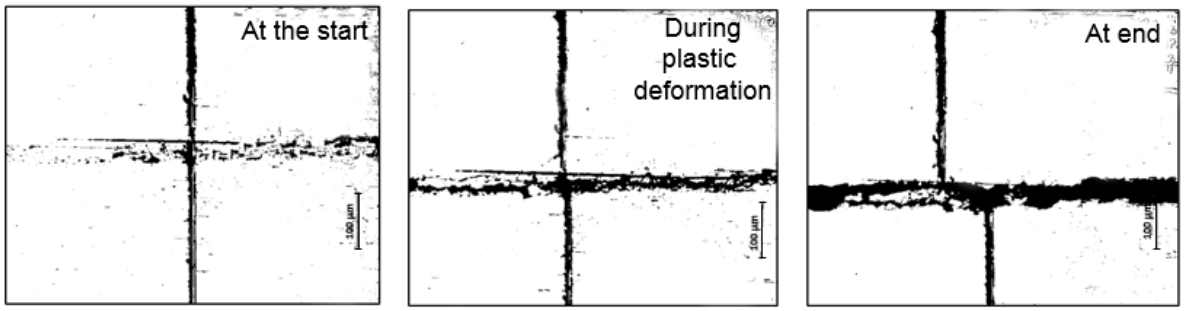

Figure 5-2: Representative binary images taken from the captured test video and these are used to calculate the shear displacements of the scribed line.

5.3 Experimental Results and Discussions

5.3.1 Microstructural Investigation of As-Fabricated Lap-Shear Solder Joints

Cross-sectional SEM micrographs of as-reflowed specimens after bulk solder etching are provided in Figure 5-3. The joint thickness for all specimens varied from 50-55 microns. The joints had three types of IMCs: Cu_3Sn, Cu_6Sn_5 and Ag_3Sn. A chemical analysis using energy dispersive X-ray spectroscopy (EDX) was performed to determine the presence of the IMCs (Figure 5-4). Differences among the contrast gray levels also revealed the presence of the IMCs. All as-reflowed specimens had a layer of Cu_3Sn IMC and Cu_6Sn_5 IMC in both interface sides of the joints. The symmetrical growth of IMCs was observed in both sides for all different soldering times. At a soldering time of 10 mins, a layer of Cu_6Sn_5 with a scalloped morphology was formed. However, at a 30 mins soldering time, the Cu_6Sn_5 layer thickness tends to grow, and the gaps between Cu_6Sn_5 scallops were blocked (Figure 5-3-b1, b2). With further increase in soldering time to 60 mins, the gaps between scallops were further blocked, and the morphology changed from scallop type to more smooth continuous layer type (Figure 5-3-c1, c2).

For 10 mins soldering time, thin layer of Cu_3Sn emerges in between Cu_6Sn_5/Cu interface. The morphology of Cu_3Sn was layer type from the beginning, and it got thickened with the increase in soldering time. The wavy interface of Cu_3Sn/Cu was uneven at 10 mins soldering time which mainly occurred due to different Cu dissolution rates at different sites. The gaps or valleys between the Cu_6Sn_5 scallops work as a fast diffusion path due to their shorter diffusion distance and Cu dissolute to bulk Sn at a higher rate through these scallop gaps to react with the remaining Sn [36,143,144]. Due to thicker IMC layers at higher soldering time, Cu dissolution rate becomes almost constant in all sites and the waviness of the Cu_3Sn/Cu interface vanishes.

A lot of Ag_3Sn particles were dispersed in the bulk solder during soldering. For a soldering time of 10 mins, Ag_3Sn particles were small in size. However, with the increase in soldering time, a noticeable coarsening of Ag_3Sn was observed. Ag_3Sn was formed as a needle-like and large sheet in the joint at the higher soldering times (Figure 5-3-b2, c2). Similar morphologies were observed for Ag_3Sn for furnace cooling in other studies [145,146]. Our fabrication process utilized slow cooling rate to achieve higher IMC thickness which also contributed to the formation of needle-like and large sheet-like Ag_3Sn IMC. The coarsened Ag_3Sn seems to be embedded into the Cu_6Sn_5 layers (Figure 5-5) and create a bridge between two opposite interfacial Cu_6Sn_5 IMC layers in some sites (Figure 5-3-b2, c2).

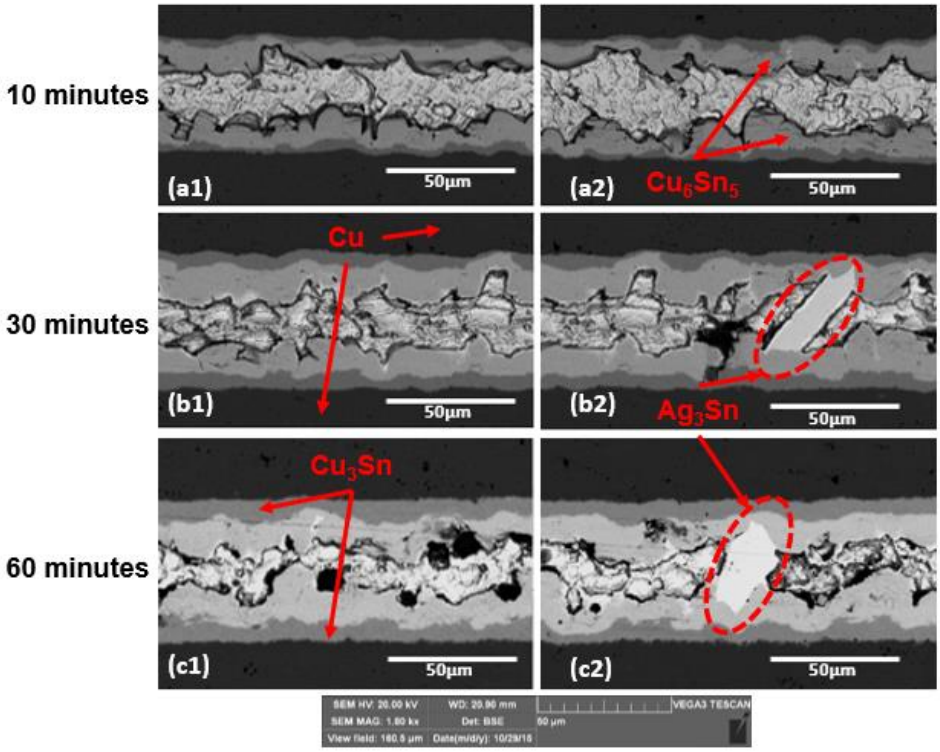

Figure 5-3: Cross sectional micrographs of the solder joints after soldering process at a temperature of 260°C and soldering time of (a) 10 minutes, (b) 30 minutes and (c) 60 minutes.

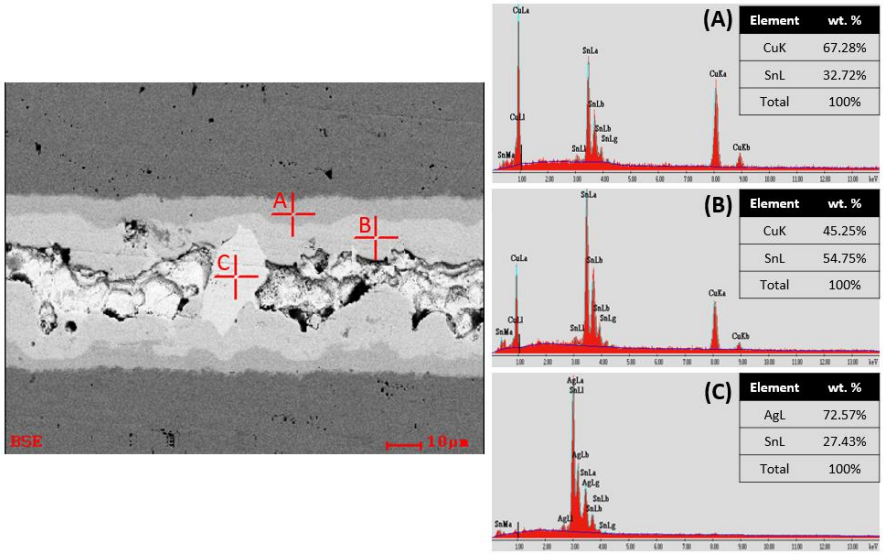

Figure 5-4: EDX analysis of the Sn-3.5Ag/Cu solder joints indicating the presence of (a) Cu_3Sn, (b) Cu_6Sn_5 and (c) Ag_3Sn IMC.

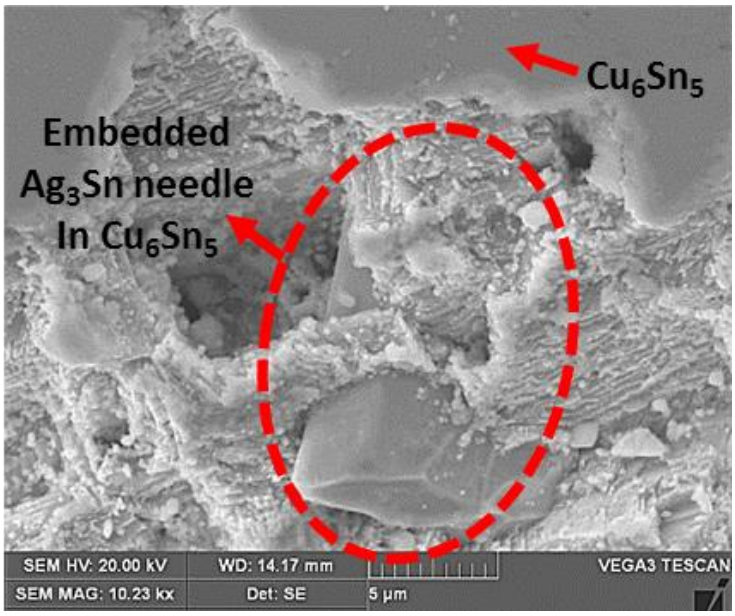

Figure 5-5: Representative SEM image of a needle like Ag_3Sn IMC embedded in Cu_6Sn_5 layer at soldering temperature of 260°C and soldering time at 30 minutes.

5.3.2 IMC Layer Growth Behavior

IMC growth kinetics during the solder reflow process has been studied by many researchers [32,44,147]. Generally, a parabolic equation of the following type is used to describe the growth kinetics of the IMCs:

$$l_i = k_i t^n \quad \textbf{(5.1)}$$

Here k_i is the IMC growth rate constant of *i* type IMC layer and *t* is the reaction time. Different time exponent, *n* values, were reported for molten solders (*n*=0.21-0.90) where a time exponent of 0.5 nicely fits with the solid-state IMC growth experimental results during the aging process. The growth during the aging process is due to volume diffusion mechanism. However, during the soldering reflow process, the growth of IMC layers is quite complex. Some researchers reported the IMC growth kinetics to be governed by grain boundary (GB) diffusion and volume

diffusion process [12,32,147–149]. It was found in the literature that if the *n* value is close to 0.33, then the IMC growth kinetics is governed by GB diffusion [148] ; while *n*=0.5 dictates that it is volume diffusion [149]. To understand the IMC growth kinetics in our case, IMC thicknesses were examined by SEM. Images were taken at four different areas in each solder joint, and each image covered an area of 160 µm x 120 µm. The capability of sub-setting a specific contrast gray level of an image in ImageJ software was utilized to select the individual IMC layers and calculated the average IMC cross-sectional surface area. This cross-sectional area was then divided by the linear length of the image, as shown in the following equation to calculate the average IMC layer thickness from SEM micrograph:

$$X = \frac{A}{L} \tag{5.2}$$

Here, *A* is the cross-sectional surface area of the IMC layer and *L* is the linear length. Three SEM images for each soldering time were processed, and the average IMC thickness with the standard deviations were documented. Figure 5-6 shows the changes in average log value of the thicknesses of Cu_6Sn_5, Cu_3Sn IMC and the total IMC of a single interfacial side of the joint with respect to the soldering time.

Table 5-1 provides the numerical values of total average IMC thickness in both interfacial sides. It was observed that for a soldering time of 10 mins, 30 mins, and 60 mins, an amount of about 40%, 60%, and 80% IMCs of total joint thickness were achieved respectively. Figure 5-6 was used to calculate the *n* values, and they were found to be 0.503, 0.334, and 0.36 for Cu_3Sn, Cu_6Sn_5, and total IMCs respectively. These values suggest that at higher soldering time, Cu_6Sn_5 IMC growth is controlled by GB diffusion while growth of Cu_3Sn is governed by

volume diffusion mechanism. Similar findings were reported by some other researchers [150–152]. According to Yu et al. [149], at the soldering time less than 60 sec, formation and growth of IMCs are controlled by chemical reaction diffusion, and the growth rate is very high. However, with the increase in soldering time, thick IMC layers develop which contribute to the delay in material diffusion to go through and react on the other side. This situation hinders chemical reaction diffusion, and volume diffusion becomes the driving mechanism.

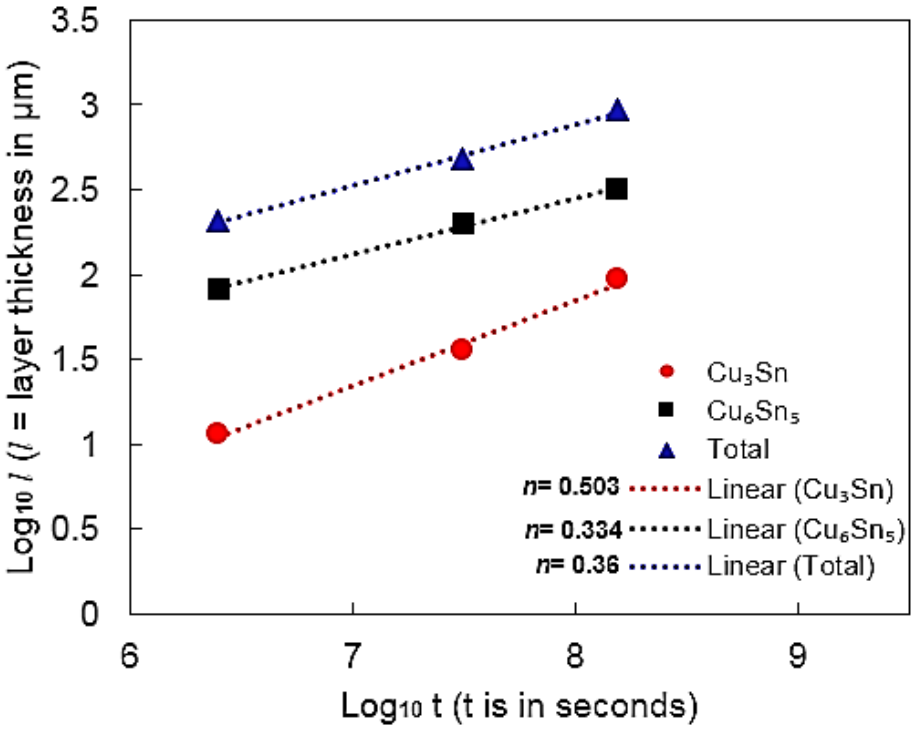

Figure 5-6: Log-Log plot of IMC layer thickness in one interfacial side vs. soldering time.

Table 5-1: IMC thickness values in the joint samples

Soldering time	Total Average IMC thickness in both interfacial sides (μm)	% of IMCs in the whole joint
10 minutes	20.50	~40
30 minutes	29.30	~60
60 minutes	38.45	~80

5.3.3 Shear Stress-Strain Properties and Effects of IMC Thickness

The shear stress vs. time curves obtained from the tests are shown in Figure 5-7. Shear stress is calculated dividing the load with the solder area. A detailed comparison among those graphs disclosed several interesting observations related to the effects of the volume fraction of IMCs on the mechanical behavior of solder joints.

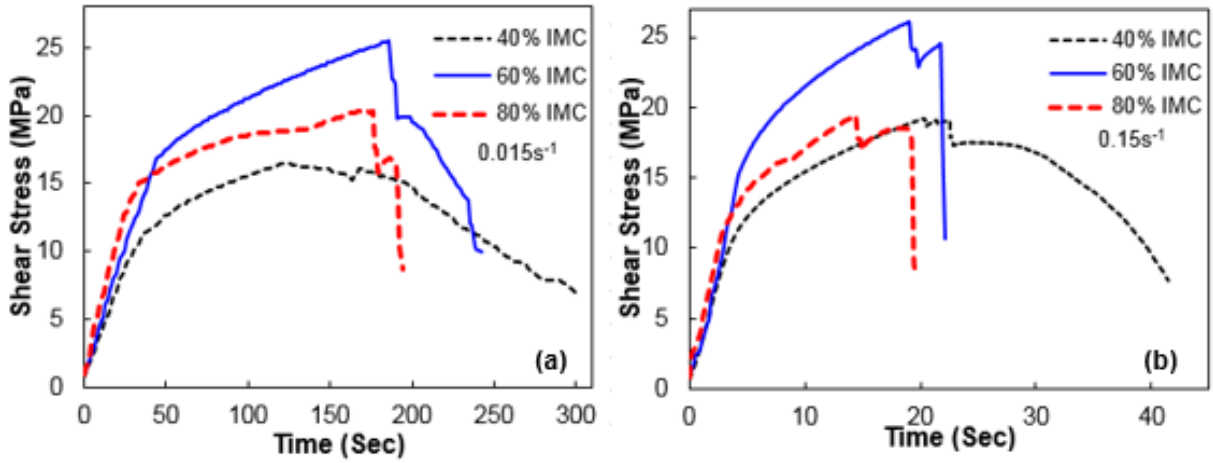

Figure 5-7: Shear Stress Vs. Time plot for solder joint samples at (a) $0.015s^{-1}$, and (b)$0.15s^{-1}$ shear strain rates.

The Volume fraction of IMCs tends to have an effect on the flow stress behavior of the joints. With the increase in IMCs from 40% to 60%, flow stress seems to increase and showed higher work hardening. Work hardening in SnAg solder is reported to be largely affected by the Ag_3Sn IMC particle size [153]. The Ag_3Sn particles have an impeding effect on the dislocation

motion. Due to their complex orthorhombic phase, dislocations that encounter these particles either bypass the obstacles by Orowan mechanism or climb over [153]. These mechanisms result in more work hardening. Therefore, joints that were fabricated at 30 mins soldering time had embedded needle-like Ag_3Sn particles (Figure 5-5) which more likely to increase the work hardening and thus flow stress. However, when IMC increases from 60% to 80%, flow stress decreases considerably. It may be due to the crack propagation path which went through the Cu_6Sn_5/Cu_3Sn interfacial layer without being affected by the Ag_3Sn particles. A more detailed explanation has been provided later in the article. Overall, a sensitive dependence of the flow stress on the IMC volume fraction was observed. A sudden drop in shear stress at the maximum load is an indication of sudden generation of a large crack in a brittle fracture which propagates easily due to the lower fracture toughness of brittle materials. For all test samples, with various IMC fractions showed sudden drop in the shear stress at the maximum load point during the tests. However, very small shear stress drops were observed in the shear stress vs. time curves for joint samples with 40% IMCs, and shear stress then gradually decreases beyond that maximum load point until it fails. Samples with 40% IMCs shows concurrent recovery, leading to nearly no hardening at all after the sudden drop. This scenario likely occurs due to the dominant ductile failure behavior. As, the samples contain a larger fraction of bulk ductile solder, the crack may initiates and transmits through the bulk solder mostly. Small drops of load were present in several points during the tests and these may be due to the easy crack propagation through the micro-voids or brittle Cu_6Sn_5 IMC. Fractography analysis was performed and discussed in the next section to clarify the failure modes. On the other hand, shear stress vs. time curves for solder joints with higher IMC thickness reveals brittle fracture

mode and the ductility diminishes substantially. Large drops in shear stress at maximum point are observed for samples with higher IMC thickness.

At higher strain rate of 0.15 s^{-1}, large shear stress drops at maximum point were apparent for all test samples. After the stress drop, samples with 40% IMCs still shows gradual decrease in shear stress while 60% and 80% IMCs samples fail almost immediately. Therefore, a sensitive dependence of the shear stress-strain behavior on the volume fraction of IMCs is more evident at higher strain rate.

Figure 5-8 shows the plots of shear strain vs. time for both $0.015s^{-1}$ and $0.15s^{-1}$ shear strain rates. The Far-field shear strain is constant with the time as it was prescribed during the experimental setup. However, local shear strain at the solder joint area seemed to deviate significantly from the far-field shear strain. It can be seen that, for all tests, initially at the same test time, the difference between the far-field shear strain and local shear strain is very high (Region 1 in Figure 5-8). This may indicate that at this period, elastic deformation of Cu and/or fixture tolerance and displacements contribute to the major portion of the far-field or crosshead displacement. After that, the local shear deformation in solder region develops with time, and local shear strain rate becomes similar to far-field shear strain rate (Similar slope of far-field and local shear strain curve in Region 2 in Figure 5-8). Similar observations were reported in some studies where local shear strain deformation was measured during the lap-shear test [47,65].

It can be observed in Figure 5-8-b that 60% and 80% IMC samples start to deform at a higher local shear strain rate earlier than 40% IMC samples when the tests were conducted at $0.15s^{-1}$ shear strain rate. At higher shear strain rate, the high volume fraction of hard and brittle IMCs

might induce higher local stresses in the bulk solder region which contributed to early local deformation. At lower shear strain rate, this effect might not be significant due to the available sufficient time for stress relaxation. Overall, the figures provide an idea on how the local shear strain evolves with time when solder joints have different IMC thicknesses.

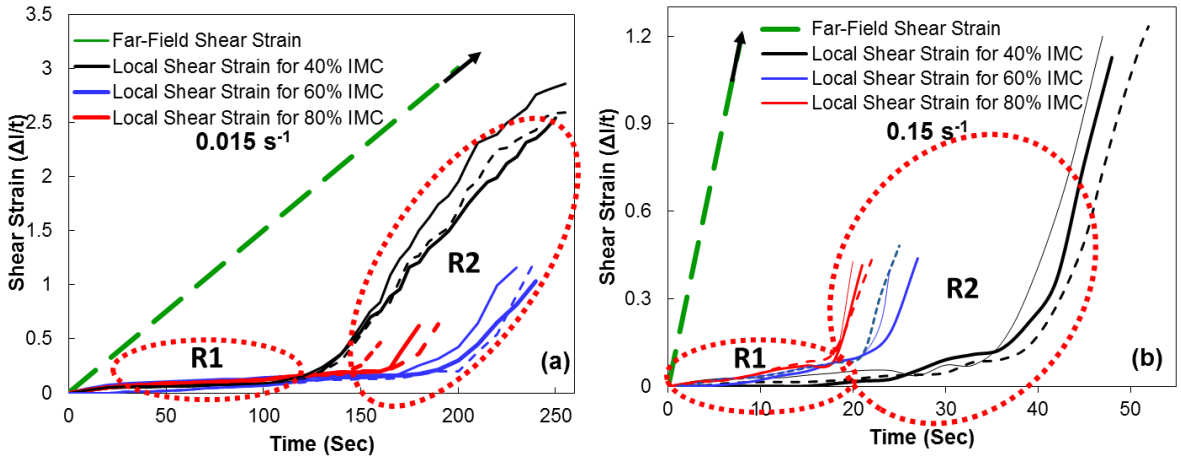

Figure 5-8: Changes in far-field and local shear strains with respect to time at (a) 0.015s-1, and (b) 0.15s-1. The local shear strains were calculated using the technique described in section 2.3. Far-field shear strain is calculated from the cross-head displacement divided by the joint thickness.

Experimental shear stresses vs. local shear strains for selected samples with different IMC thickness were plotted in Figure 5-9 to compare their shear behavior. Apparently, with the increasing volume fraction of IMCs, the solder exhibits a higher stiffness (Figure 5-9-a,b). This is true for both shear strain rate cases. It is established in the literature that shear modulus or stiffness is significantly different in bulk solder, Cu_6Sn_5, and Cu_3Sn [130,154,155]. Shear modulus of IMCs is higher than that of bulk solder. Therefore, as the volume fraction of IMCs increase from 40% to 60%, and 80%, solder tends to provide a stiffer response. On the other hand, ductility and gradual decrease in shear stress with shear strain were observed for samples

with 40% IMCs. Effects of IMC thickness on other shear properties such as the ultimate shear strength and strain to failure are discussed in the following paragraph.

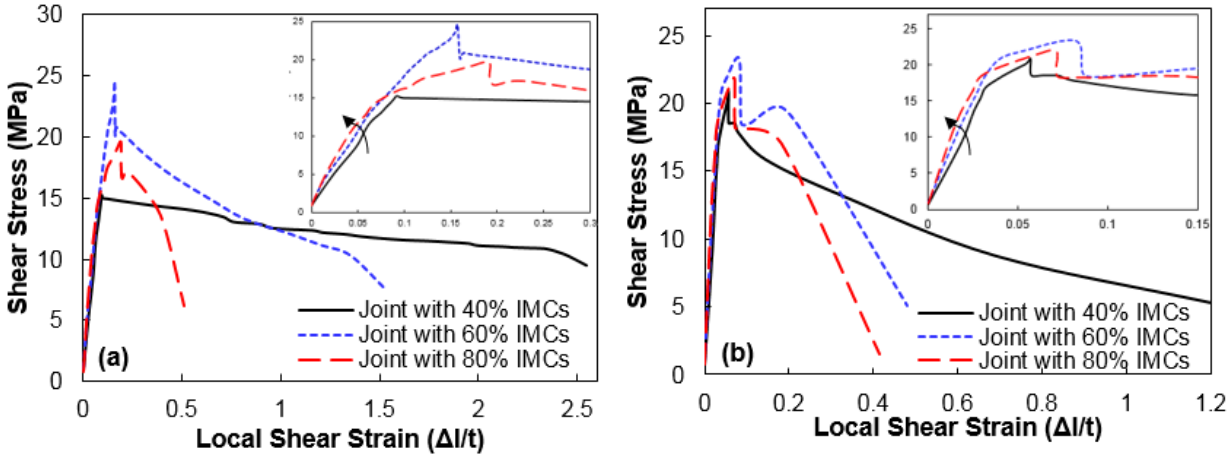

Figure 5-9: Shear stress- shear strain curve for test specimens tested at (a) $0.015s^{-1}$, and (b) $0.15s^{-1}$ shear strain rate. The figures have magnified view of elastic region in the inset

Figure 5-10 shows the effects of the variation in IMC volume fraction on the shear strength and strain to failure (fracture strain) at $0.015s^{-1}$ and $0.15\ s^{-1}$ strain rates. It can be seen that, with the increase in the volume fraction of IMCs from 40% to 60%, shear strength increases significantly (from 16 MPa to 24 MPa for $0.015\ s^{-1}$; 20 MPa to 25 MPa for $0.15\ s^{-1}$). Recently, several researchers reported similar observation while analyzing joints with various IMC thickness [44,156,157]. These hard and brittle IMCs resist shearing at the beginning of the plastic flow. So, with the higher IMC thickness, resistance to the initial shear deformation increases and shear stress increases considerably. Local images captured during the tests for 60% IMCs samples show that major portion of the cracks propagate through and partially broke Cu_6Sn_5 IMC (Figure 5-11-b). However, a decrease in shear strength was witnessed when 60% IMCs and 80% IMCs samples were compared although the shear strength values are still

higher than the shear strength of 40% IMCs joints. Similar trend in the correlation between shear strength and IMC layer thickness was reported recently by Xing et al. [158] for Zn-Sn-Cu-Bi/Cu solder joint. They observed an initial increase in shear strength when IMC layer thickness increased. However, shear strength was observed to deteriorate quickly with continuous increase in IMC thickness. In our study, it has been observed during the *in situ* test that cracks propagated through the Cu_6Sn_5/Cu_3Sn interface for 80% IMCs joint (Figure 5-11-c). With 60 mins soldering time, the joints developed a thicker planar Cu_3Sn/Cu_6Sn_5 interfacial layer (Figure 5-3-c1, c2). This interfacial Cu_3Sn/Cu_6Sn_5 planar layer tends to be an easy fracture path by delamination [159]. As, the interfacial layer of Cu_3Sn/Cu_6Sn_5 was wavy and thin for joints fabricated with 30 mins soldering time; it resisted the crack propagation and delamination of the interfacial Cu_3Sn/Cu_6Sn_5 layer (Figure 5-3-b1, b2). The above observation promotes the necessity of including Cu_3Sn/Cu_6Sn_5 interfacial delamination as a major failure mode criteria when a thicker planar interfacial layer is present in Cu_6Sn_5/Cu_3Sn interface in the joint after fabrication.

Strain to failure was measured from the final axial displacement of the scribed line after the test fails and dividing it by the total joint thickness. Strain to failure seemed to be affected by the volume fraction of IMCs. A significant reduction in failure strain was observed when the IMC thickness was increased. Also, 40% IMCs joints exhibited highest failure strain due to the ductility provided by bulk solder which controlled the failure mode. For higher IMC thickness joints, the failure mode was controlled by IMCs. As, it is known that hard and brittle materials assist crack propagation due to their lower fracture toughness. So, when cracks

initiate at high IMC thickness samples, it propagates through the IMCs which is a faster fracture path and fails at a lower shear strain.

Shear strain rate has a profound effect on the shear properties of solder joints [160,161]. To understand the effects of shear strain rates on the shear behavior of the joints with higher IMC volume fraction, the tests were conducted at 0.015 s^{-1}, and 0.15 s^{-1} shear strain rate that is ten times higher. At higher shear strain rate, shear strength increases for all test samples with different IMCs although the increase is noticeable for 40% IMC joint samples but the increase for 60% IMC and 80% IMC joint samples were insignificant (Figure 5-10-a). Overall, the shear strengths are not largely affected by the shear strain rates at this level. Experiments need to be conducted at higher shear strain rates to investigate their effects on shear strength.

For both 0.015 s^{-1} and 0.15 s^{-1} shear strain rate, the strain to failure decreases with the increase in the IMC volume fraction (Figure 5-10-b). Higher shear strain rate reduces the strain to failure significantly for 40% IMC joints. It has been observed while performing the fractography analysis that at 0.015s^{-1} shear strain rate, joints with 40% IMCs fail mostly in the solder region while fracture locations are changed to IMCs or solder/IMC interface at 0.15s^{-1} shear strain rate. Ductility of bulk solder contributes towards the higher failure strain whereas lower strain to failure is observed at higher shear strain rate due to the brittle failure of IMCs with lower fracture toughness. The effects of shear strain rates on the joints with 80% IMCs are not

significant as brittle failure mode is evident in both cases, providing almost similar strain to failure. Further detailed discussions are provided in the fractography analysis section.

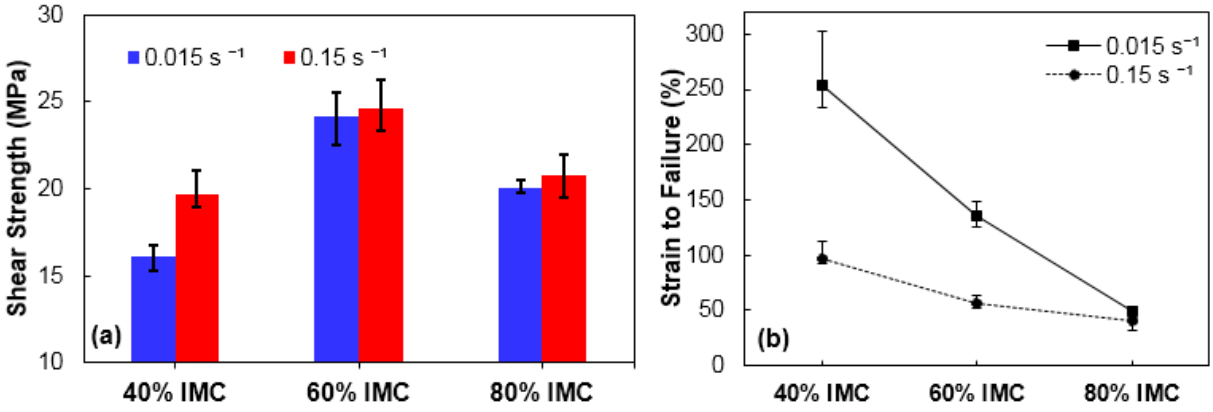

Figure 5-10: (a) Shear strength(MPa) and (b) shear strain (%) to failure with respect to volume fraction of IMCs at a shear strain rate of **0.015 s^{-1}** and **0.15 s^{-1}**.

5.4 Fractography Analysis of the Fracture Surfaces

There are five probable fracture paths that a primarily interfacial crack may follow to eventually cause the failure of the joint. These paths are: (a) through the solder, (b) along solder/Cu_6Sn_5 interface, (c) through Cu_6Sn_5 IMC, (d) along the Cu_6Sn_5/Cu_3Sn interface, and (e) through Cu_3Sn [162]. Cracks may also move in between these proposed paths. Crack propagation through the solder provides a ductile failure mode where propagation along the solder/Cu_6Sn_5 interface introduces a ductile-brittle mixed failure mode. If crack propagates through the Cu_6Sn_5, and/or Cu_3Sn, and/or along Cu_6Sn_5/Cu_3Sn interface, it shows a brittle failure mode. In thicker solder joints, the most common fracture modes are through the solder, along Cu_6Sn_5/solder interface or through Cu_6Sn_5 IMC [162]. The others are not prevalent. However, thinner joints also add the other mechanisms, especially when the joint has a high

volume fraction of IMCs [162]. Figure 5-11 shows the representative crack path propagation sites optically captured during *in situ* tests for samples with 40%, 60%, and 80% IMCs.

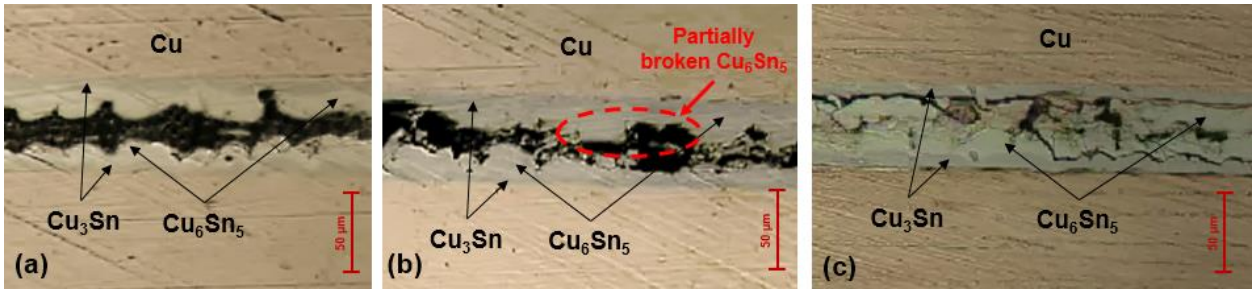

Figure 5-11: Representative optical microscopic image taken during the *in situ* lap-shear test of joint sample with (a) 40% IMC with intact Cu_6Sn_5, (b) 60% IMC with partially broken Cu_6Sn_5 IMC, and (c) 80% IMC with Cu3Sn/Cu_6Sn_5 delamination. Image quality is average due to the limitation in microscope resolution.

Fractography analysis was conducted after the single lap-shear tests to understand the failure mechanism for high IMC thickness joint samples. Figure 5-12 shows the failure surfaces of the joints at $0.015s^{-1}$, where Figure 5-13 has the failure surface images of the joints at $0.15s^{-1}$. At 40% IMCs joint with $0.015s^{-1}$ shear strain rate, fracture surface smearing along the loading direction was highly evident (Figure 5-12–a). A similar observation was reported by Deng et al. during lap-shear tests [40]. Moreover, exposed Cu_6Sn_5 IMC was observed in the smeared fracture surfaces. Lee et al. [39] have proposed the IMC exposure mechanism which is as follows. Cu_6Sn_5 nodule tips protrude on the fracture surface due to a combination of low fracture toughness of Cu_6Sn_5 and the local strain concentration on the Cu_6Sn_5/solder interfaces. Optical microscopic image provided at Figure 5-11-a also gives an impression of the crack propagation which was mostly along the soft solder region. These suggest that the solder joints failed with a ductile fracture mode and crack propagated through the bulk solder. For solder

joints with 60% IMCs at $0.015s^{-1}$, there still exists some fracture surface smearing along the shear direction, although the exposed Cu_6Sn_5 amount is higher in this case (Figure 5-12–b). There was some broken Cu_6Sn_5 IMCs observed at the fracture surface. Also, optical images taken during the tests showed crack propagation along solder/Cu_6Sn_5 interface with some broken Cu_6Sn_5 IMCs (Figure 5-11-b). This observation depicts that failure occurred mostly along solder/ Cu_6Sn_5 interface, providing a ductile-brittle mixed failure mode. On the other hand, SEM fractograph of fracture surfaces of solder joints with 80% IMCs at $0.015s^{-1}$ portray an interesting failure mode (Figure 5-12–c1, c2). EDX analysis provided a significantly higher Cu picks at the exposed area pointed at target 2 in Figure 5-12-c1. This suggests that the sampling region was possibly Cu_3Sn layer. Transition ridges at which the fracture shifted to the Cu_6Sn_5/Cu_3Sn interface, with exposed Cu_3Sn was observed (Figure 5-12–c1). There was few intact Cu_6Sn_5 near to the transitional ridge. A magnified image of fracture surface provided a view of micro cracks on the Cu_3Sn surface (Figure 5-12–c2). In these samples, the cracks tend to frequently transit between the two opposite Cu_6Sn_5/Cu_3Sn interfaces. Optical microscopic image of crack propagation provided at Figure 5-11–c also showed the transition of crack path between two opposite Cu_6Sn_5/Cu_3Sn interfaces. This crack transition between two interfaces may be largely activated by the brittle Ag_3Sn sheets which made a bridge between two interfacial sides (Figure 5-3-b2, c2). From Figure 5-3-c1, c2 it was seen that Cu_3Sn layer was mostly thicker and planar for joints fabricated at 60 minutes soldering time. In this case, apparently Cu_6Sn_5/Cu_3Sn interface delamination dominated the failure mechanism. It was reported by Hayes et al. [159] that when joints had higher percentage of Cu_3Sn, interfacial delamination between Cu_3Sn/Cu_6Sn_5 layer may dominate due to its relatively lower fracture toughness. Overall, although the joints had a very high percentage of

Cu_6Sn_5, thickness of Cu_3Sn and morphology of Cu_3Sn/Cu_6Sn_5 interfacial layer tend to control the failure site.

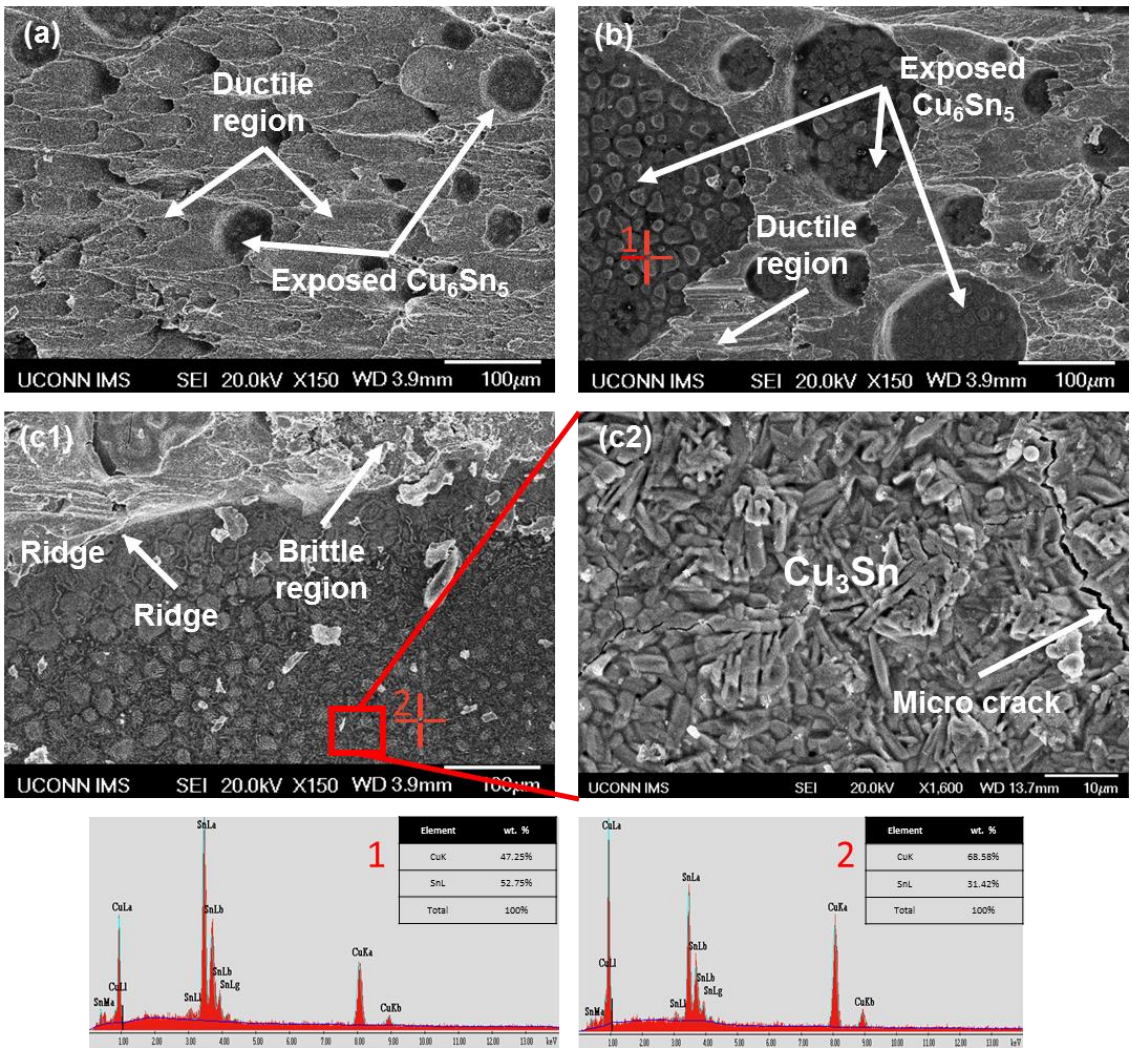

Figure 5-12: Representative SEM fractograph images of solder joints with (a) 40% IMCs, (b) 60% IMCs, (c1) 80% IMCs, and (c2) magnified view of exposed Cu_3Sn at 80% IMCs samples. These images were taken from samples tested at $0.015s^{-1}$ shear strain rate. EDX analysis indicating possible (1) Cu_6Sn_5,and (2) Cu_3Sn IMC.

SEM Fractograph images for samples investigated at $0.15s^{-1}$ shear strain rate is provided in Figure 5-13. Fractography analysis at samples with 40% IMCs showed the ductile region with

elongated dimples; although this time, the exposed Cu_6Sn_5 amount was higher and the dimples were either very small or very large (Figure 5-13-a). The amount of shear smearing at bulk solder was also less than samples with 40% IMCs tested at lower shear strain rate. Samples with 60% IMCs showed brittle fracture regions with transition ridges from solder to IMC (Figure 5-13-b). It had both exposed Cu_6Sn_5 and Cu_3Sn regions. Similarly, 80% IMCs joint samples showed almost identical fracture surfaces with brittle regions and exposed IMCs. Overall, at higher shear strain, joints with a higher volume fraction of IMCs showed brittle fracture mode.

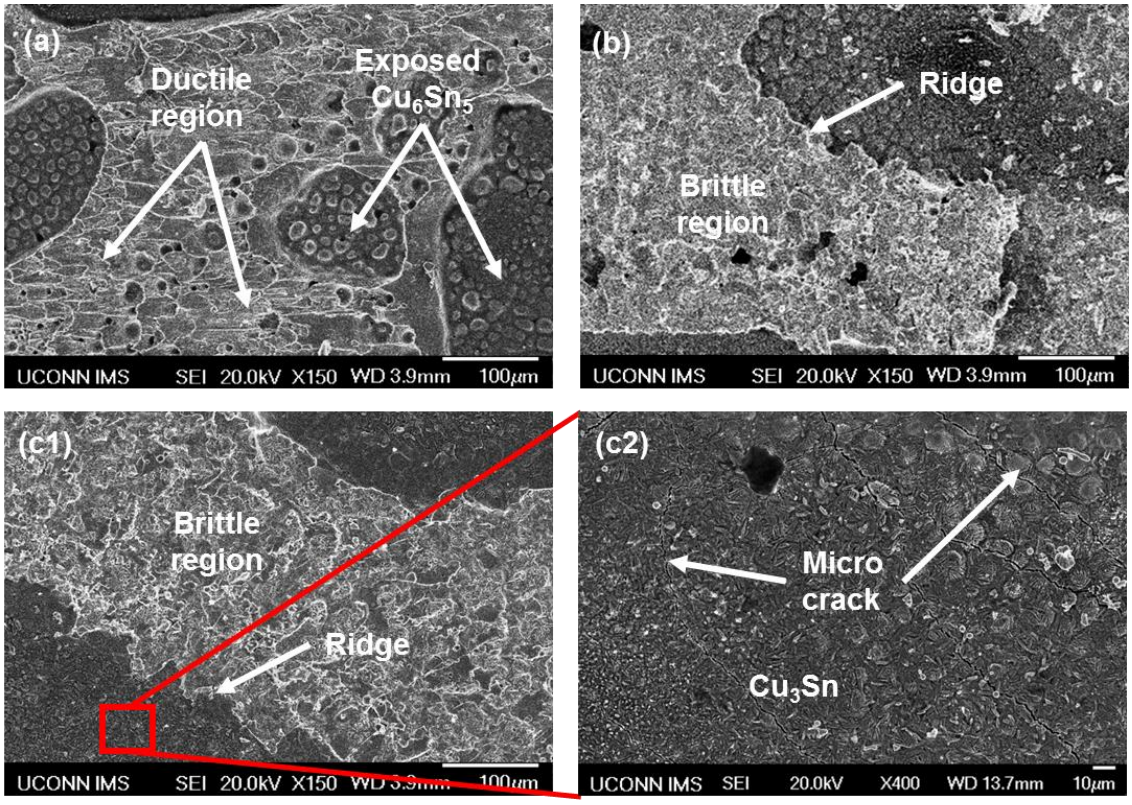

Figure 5-13: Representative SEM fractograph images of solder joints with (a) 40% IMCs, (b) 60% IMCs, (c1) 80% IMCs, and (c2) magnified view of exposed Cu_3Sn at 80% IMCs samples. These images were taken from samples tested at 0.15s-1 shear strain rate.

The trend observed from the shear stress-strain behavior, and fractography analysis suggests that fracture behavior of the joints largely dependent on the volume fraction of IMCs. A schematic diagram of possible fracture path is shown in Figure 5-14. Figure 5-14 shows that when IMC volume fraction is less than the bulk solder volume fraction, failure mode tends to be controlled by bulk solder region and ductile fracture is being dominated. However, when IMC volume fraction is larger than bulk solder volume fraction, the failure mode is largely dominated by the IMC presence and morphology. When a solder joint has a thick Cu_3Sn with planar Cu_3Sn/Cu_6Sn_5 interfacial layer, the joint tends to fail due to the Cu_3Sn/Cu_6Sn_5 interfacial delamination. In the next section, we have performed a crystal plasticity finite element simulation to understand how Cu_6Sn_5/Cu_3Sn interfacial morphology could affect the overall shear strength of solder joint with 80% volume fraction of IMCs.

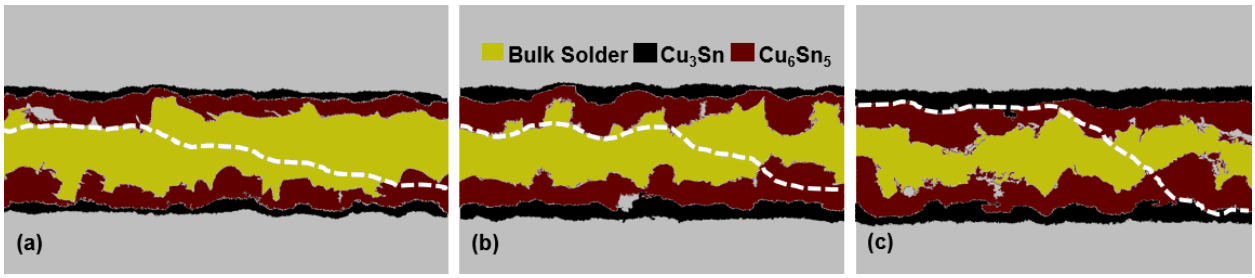

Figure 5-14: Proposed crack propagation and fracture path for solder joints with (a) 40% IMCs, (b) 60% IMCs, and (c) 80% IMCs. These images are not to scale

5.5 Crystal Plasticity Finite Element Simulation of Crack Propagation

To investigate the effect of interfacial morphology, we performed a computational study. Previously, crystal plasticity finite element (CPFE) analysis observed to be more effective than the traditional finite element (FE) simulation. CPFE method takes the mechanical anisotropy and micro-mechanical grain properties into account, and analyze the mechanical deformation

using crystallographic slip behavior of the materials. Previously, we have reported a complete CPFE model to analyze the shear behavior of micro-scale solder bonds [163].

5.5.1 Geometry Considered For This Study

Finite element software, Abaqus with extended user material subroutine (UMAT) has been used in this study to incorporate the crystal plasticity constitutive model. Meshing element C3D8R with enhanced hourglass stiffness was used. Stress based mesh sensitivity analysis was performed to achieve an optimum mesh size for the model. The computational geometry has been generated by including Cu substrates, Cu_6Sn_5 IMC, Cu_3Sn IMC, an interfacial layer in between Cu_6Sn_5 and Cu_3Sn and and another interfacial layer in between Sn and Cu_6Sn_5. Only a part of the whole solder joint was modeled for simplification. The solder joint had a thickness of 50 µm with a 50 µm x 50 µm pad area. The average thickness of the Cu_6Sn_5 and Cu_3Sn IMC layers were taken from the experimental microstructural investigation performed earlier. These material layers were assumed to be same through the joint. The interfacial element layers thickness assumed to be of 1 µm. The geometrical model, along with the boundary conditions are provided in Figure 5-15. Three types of Cu_3Sn/Cu_6Sn_5 interfacial layer morphologies have been used in this analysis where the waviness of the interfacial layer was changed from planar to wavy. The Cu_6Sn_5 morphology has been kept same in all three configurations. Figure 5-16

is showing the three variations of the morphology used in this analysis. Displacement loading condition has been considered for the study to assign a similar shear strain rate of $0.15s^{-1}$.

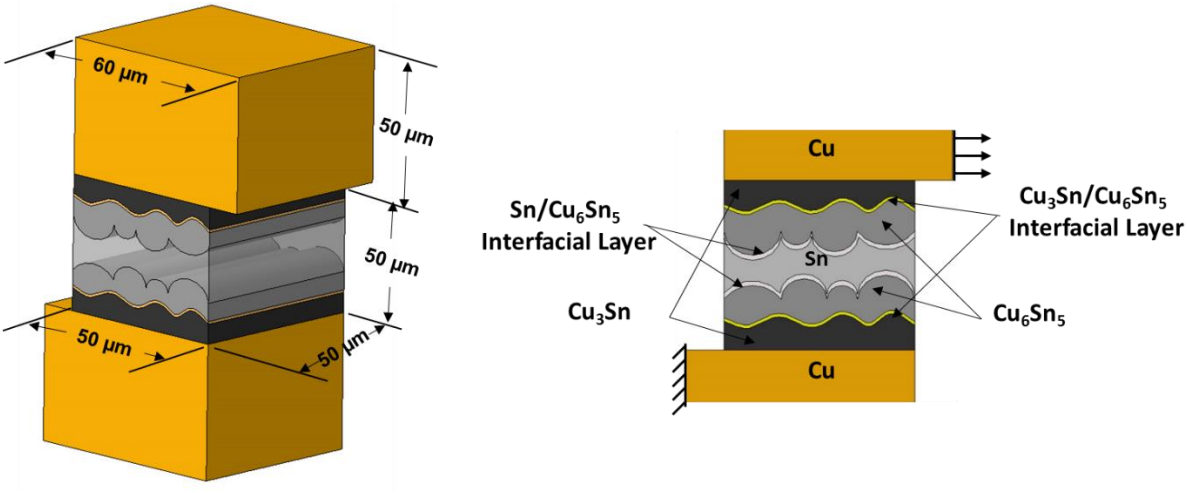

Figure 5-15: Computational geometry with dimensions, showing different materials considered in the study

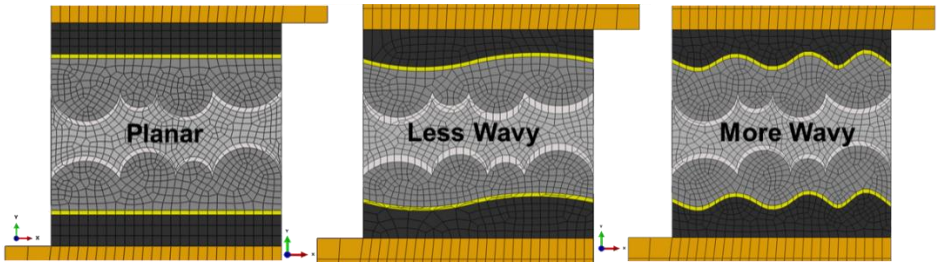

Figure 5-16: Different Cu_3Sn/ Cu_6Sn_5 interfacial morphology considered in the computational study

5.5.2 Material Properties

Cu substrate and Cu_3Sn have been modeled as isotropic elastic materials due to their polycrystalline microstructure. Their elastic properties used in this analysis are provided in Table 4-1. Most active slip systems for both Sn and Cu_6Sn_5 material were incorporated in this analysis (Table 4-2). The crystal plasticity slip parameters for Sn, Cu_6Sn_5 are provided in Table

4-4. The models have been considered to have one grain of Sn, and 4 grains of Cu_6Sn_5 IMC. The Cu_6Sn_5 properties were provided to the interfacial layer elements. As, the CPFE model was written in Abaqus UMAT subroutine, it was not possible for us to model the interfacial element layer with the cohesive zone modeling (CZM) as CZM needs Abaqus/Explicit where we would have to transform the UMAT subroutine to VUMAT subroutine. This task is very challenging and time consuming. For the sake of computational time and cost, we modeled the failure using a simplified approach based on von Mises yield criterion. Von Mises yield criterion is a reasonable approach when the model has complex loading conditions with different materials presence. When an element reaches to a certain von Mises stress, the stiffness of this element is transformed to almost zero so that it would not be able to take part in the further analysis. This method has been reported to be effective for crack propagation visualization and modeling in Abaqus/Standard [164,165]. Literature review suggests that generally, Cu_3Sn IMC region does not fail due to their higher fracture toughness compared to Cu_6Sn_5 IMC [159,166]. For our study, we have disregarded the failure of Cu_3Sn region. Failure criteria based on maximum shear strength for both Sn and Cu_6Sn_5 IMC are available in the literature [126,167,168]. Maximum shear strength value of 40 MPa and 670 MPa for Sn and Cu_6Sn_5 respectively have been assigned to the model, and when the respective elements exceed the mentioned value, the stiffness of the elements are transformed to almost zero value. According to the physical definition, the true value of the strength of interfacial layers found in solder joints are extremely difficult to measure experimentally at a micro-scale [157,169]. Thus, failure criteria for Cu_6Sn_5/Cu_3Sn and Sn/Cu_6Sn_5 interfacial layers are not available in the literature. However, some attempts have been made to utilize the strength values obtained in the solder ball pull and shear tests to computationally model the interfacial elements

[38,166,168,169]. Yang et al. [169] used a Xu-Needleman exponential traction-separation law to model the interfacial behavior of Cu_3Sn/Cu_6Sn_5 layer using CZM approach. In their study, they have performed solder ball pull and shear tests, and recorded the corresponding strength when the failure occurred at the Cu_3Sn/Cu_6Sn_5 interface. Then, they used the pull strength value as the maximum normal traction and shear strength value as the maximum tangential traction as the CZM parameters. On the other hand, similar approach has been taken by Yamin et al. [168] where they modeled the interfacial layer between Cu_6Sn_5 and Sn using a bilinear traction-separation law. They utilized solder ball pull and shear test strengths performed by Song et al. [170] and obtained the maximum normal traction and maximum tangential traction values from the pull strength and shear strength when the failure occurred at the Cu_6Sn_5/Sn interface. For Cu_3Sn/Cu_6Sn_5 interfacial elements, the maximum normal and tangential traction used by Yang et al. [169] was 97.49 MPa and 94.49 MPa respectively. Yamin et al. [168] used 43.66 MPa and 56.77 MPa as the maximum normal and tangential traction respectively for Sn/Cu_6Sn_5 interface. In our case, estimated average value of 96 MPa for Cu_3Sn/Cu_6Sn_5 interface and 50 MPa for Sn/ Cu_6Sn_5 interface were used as failure criteria. Due to the complex loading conditions in the interfacial elements, von Mises stress failure theory is assumed to be a reasonable approach. When the von Mises stress exceeded the prescribed strength value in an interfacial element, the stiffness of that element changed to a value near to zero. Table 5-2 shows the failure strength of different materials and interfacial layers used in the present study.

Table 5-2: Failure strengths of the regions considered in the study

Region	Failure Strength	Reference
Sn	Maximum shear stress: 40 MPa	[168]
Cu_6Sn_5	Maximum shear stress: 670 MPa	[126]
Cu_3Sn/ Cu_6Sn_5 interface	Maximum von Mises stress: 96 MPa	[169]
Sn/ Cu_6Sn_5 interface	Maximum von Mises stress: 50 MPa	[168]

5.5.3 Computational Results & Discussions

Crack initiation and propagation paths for all three interfacial morphologies are provided in Figure 5-17. A solution dependent variable (SDV) was used to track and differentiate in between the active and inactive elements in the model. At the beginning of the simulation, all elements were assigned a SDV of 0. An element when exceeded the failure criterion, the stiffness of that element was then changed to a value very close to zero. Then, the SDV was updated for that element and a value of 1 was assigned. In three considered cases, crack initiates at the Sn/Cu_6Sn_5 interfacial boundaries and propagates through bulk Sn. Results show that the variation in Cu_3Sn/Cu_6Sn_5 interfacial morphology does not have any effect on the crack initiation and propagation sites. Although the variation in morphology changes the stress distribution in the interfacial region, the generated stress in Sn region is consistent in all three cases, causing the crack to initiate and propagate through the same site.

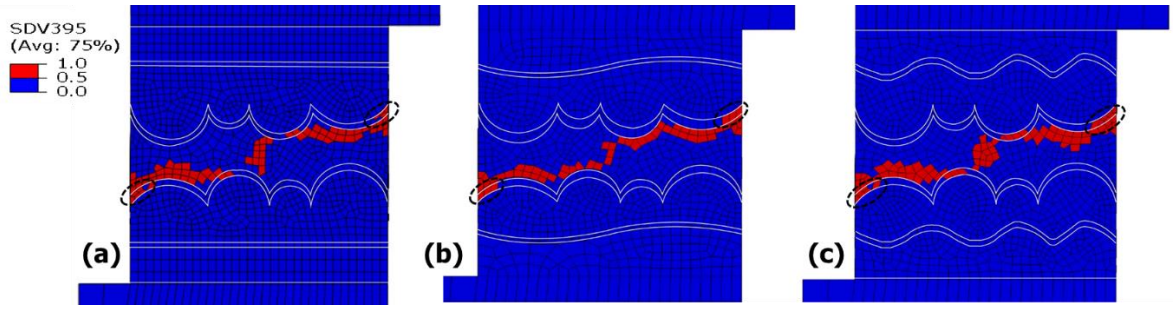

Figure 5-17: Contour plots showing crack propagation for (a) planar, (b) less wavy, and (c) wavy Cu_3Sn/Cu_6Sn_5 interfacial morphology. The black dotted circles showing crack in the Cu_6Sn_5/Sn interfacial layer region

Figure 5-18 provides the shear stress vs. shear strain curves for three different interfacial morphologies. Experimental shear stress-shear strain curve for 80% IMC samples recorded

during the single lap-shear test is also included in the figure for comparison purpose. Shear stress is calculated by dividing the total reaction force with the pad area of 0.050 mm x 0.050 mm. On the other hand, dividing the changes in displacement with the joint thickness of 50 µm provides the shear strain. The observed shear stress vs. shear strain curves for different interfacial morphology do not show any variation. This is due to the fact that the failure in this three cases is controlled by Sn region and the stress accumulation does not change noticeably in the Sn region. Thus, the simulations provide identical shear stress-shear strain response. Ultimate shear strength observed in all three cases were similar to the experimental ultimate shear strength obtained at the single lap-shear test (Figure 5-18). During simulation, ultimate shear stress was achieved at a shear strain of ~0.065 where it was ~0.08 in the experimental case. The developed model can efficiently predict the ultimate shear strength and shear strain at the maximum shear stress. After reaching at the maximum shear stress, crack develops immediately and the model fails. The conducted simulation approach is not able to predict the failure strain accurately. In conclusion, an extended cohesive zone modeling of the interfacial layers, along with the conversion of UMAT crystal plasticity to VUMAT crystal plasticity modeling is necessary to achieve more accurate results.

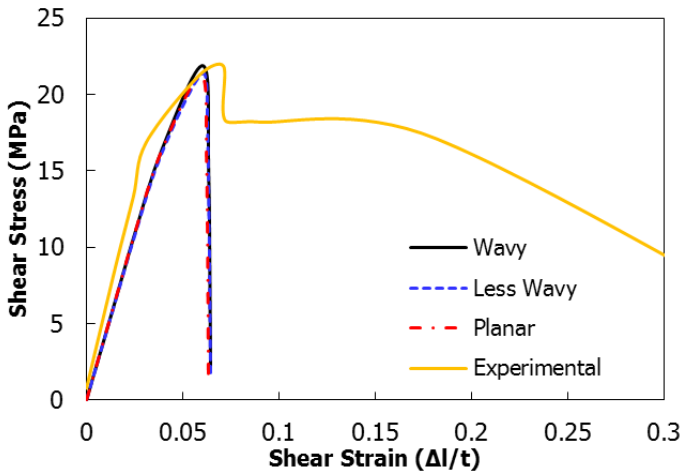

Figure 5-18: Shear stress vs. shear strain curves for models with different Cu_3Sn/Cu_6Sn_5 interfacial morphology. Experimental curve obtained during the single lap-shear test is also included for the comparison purpose

5.6 Summary and Conclusions

The shear stress-strain and fracture behavior of Sn-3.5Ag/Cu solder joints with 50µm thickness were investigated in this study. Different volume fractions of IMCs were achieved by fabricating samples with different soldering time at 260°C soldering temperature. The effects of IMC volume fraction on the shear behavior of the solder joints was then investigated using a single lap-shear test with two different shear strain rates. An optical measurement technique, along with developed image processing computer program was used to investigate the local shear strain behavior at solder region. Cross-sectional observations of the joint samples revealed different IMC thicknesses and morphologies at different soldering times. The study and findings are summarized here:

- With the increase in volume fraction of Cu_3Sn and Cu_6Sn_5 IMCs from 40% to 60%, a large increase in shear strength was observed. On the other hand, when the volume fraction of

IMCs was 80% with a thick layer of Cu_3Sn, a decrease in shear strength was observed although it was still higher than the shear strength of 40% IMCs joints.

- Local shear strain behavior was completely different than far-field shear strain behavior due to the role of elastic deformation of Cu substrate, and/or the fixture tolerance and displacements. Therefore, care should be taken during the shear behavior analysis to investigate the micro-scale solder joints.
- With increasing volume fraction of IMCs in the solder joints, an apparent stiffer shear response was observed. This may be due to the higher shear modulus of IMCs compared to the bulk solder.
- Strain to failure is greatly affected by the presence of IMCs in the solder joint. With the increase of IMC thickness, strain to failure tends to decrease consistently. The rate of decrease was higher for low shear strain rate compared to the decrease rate for higher shear strain rate.
- Fractography analysis shows that when a solder joint had a higher volume fraction of bulk solder, fracture behavior was dominated by solder with the ductile failure mode. However, when joint had a higher volume fraction of IMCs, brittle fracture mode was evident and largely controlled by IMC morphology.
- An extended cohesive zone modeling of the Cu_3Sn/Cu_6Sn_5 and Sn/Cu_6Sn_5 interfacial layers along with the conversion of UMAT crystal plasticity to VUMAT crystal plasticity is recommended to capture the interfacial crack propagation in higher volume fraction of IMC solder joint samples.

CHAPTER 6 : Effects of IMC Thickness on the Thermo-mechanical Fatigue Behavior of Micro-scale Solder Joints: Computational Study

6.1 Introduction

The large volume fraction of IMCs may affect the mechanical behavior, thermo-mechanical and mechanical fatigue life and reliability of the solder interconnects due to the very brittle nature compared to solder material. The question that this study is seeking to answer is how degrading IMCs are to the thermo-mechanical reliability of the micro-bumps used in 3-D ICs where the micro solder bumps have only a few microns of bond thicknesses. Several factors such as 'squeezed-out' solder geometry and IMC thickness are studied through a numerical experiment. Fatigue life is calculated using Coffin-Manson model.

6.2 Package and Bond Structure Considered in the Study

The 3D electronic package, modeled in this study is of 10.371 x 5.276mm. The package contains two similar thickness silicon substrate stacked on one another and attached using only one row of 114 solid-liquid inter diffusion (SLID) bumps in the middle of the package with a pitch of 0.085mm. (Figure 6-1). The DNP (distance from the neutral point) of the furthest

micro-bump is 4.845mm. The bonds contain electroplated Cu pillars of 40µm diameter with Sn3.9Ag0.6Cu solder in between the pillars. Underfill was injected between the silicon layers to improve the mechanical performance. The package was assembled on a Bismaleimide Triazine (BT) substrate and die attach material was used as adhesive in between the silicon layer and the substrate. After the SLID process, about 10µm thick bond height was achieved in the bumps. Total standoff height of micro-bumps in this package was found to be about 35µm.

To investigate the micro solder bump structure and composition, the package was cross-sectioned and scanning electron microscope (SEM) was utilized to image the micro solder bumps. SEM imaging shows that the solder has squeezed out of the bonding area. This is due to the excess pressure on the package while bonding process was conducted. This a common and expected phenomenon due to the size of the bumps and volume of the solder [45]. This effect may reduce the standoff height of the solder that if substantial, may affect the thermos-mechanical reliability of the joints [171]. Elemental mapping of the bump reveals no Cu in the squeezed out region, indicating that there is no IMCs formed there. SEM and an elemental map of the bond area are shown in Figure 6-1.

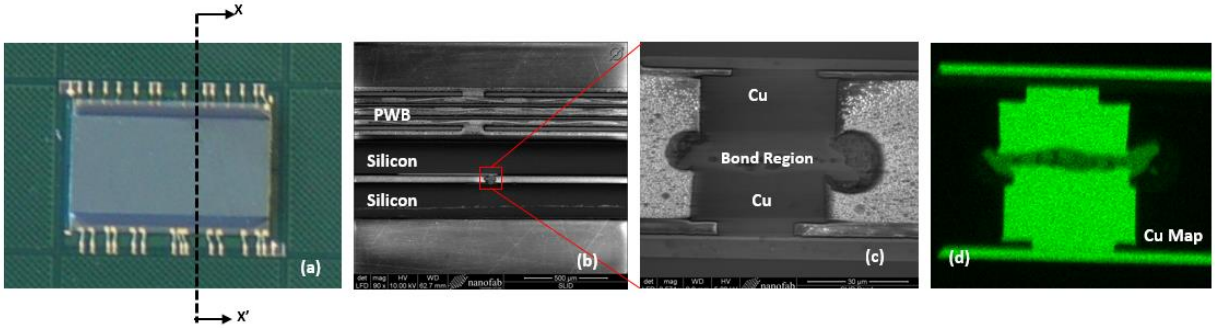

Figure 6-1 : (a) Microelectronic package, showing the cross section line, (b) SEM image of the cross sectioned area, (c) SEM image of the micro solder bump, revealing the bond structure, (d) shows Cu material mapping of the bond area.

6.3 Material Properties

Materials that were used in the finite element analysis are listed in Table 6-1 with their properties. IMC layer was assumed to be an isotropic elastic material as the yield strength of the materials are very high compared to bulk solder [106]. Considering different IMCs (Cu_3Sn, Cu_6Sn_5, $NiSn_4$) are reported to have a similar effect on the fatigue behavior of the bond [57] although Cu_3Sn provides marginally less fatigue life due to its stiffer elastic behavior. Mechanical properties of Cu_3Sn was used in the analysis to be more conservative.

In the analysis, all materials were assumed to be completely elastic except solder and Cu. We disregarded the viscoelastic behavior of underfill material, although it has been observed recently that viscoelastic model for the temperature dependent material behavior of underfill might affect the overall package performance [172]. Bilinear isotropic hardening behavior is used to describe the plasticity of Cu, and yield strength, and tangent modulus are given in Table 6-2. The FE analysis in this study assumed an elastic-plastic-creep material property for the micro-bump solder material that can be presented as:

$$\varepsilon = \varepsilon_e + \varepsilon_p + \varepsilon_{cr} \quad \textbf{(6.1)}$$

Here, ε is the total strain, ε_e is the elastic strain, ε_p is the rate-independent inelastic strain, and ε_{cr} is the rate-dependent inelastic or creep strain. The rate independent constitutive model can be formulated as:

$$\sigma = C_p \varepsilon_p^{n_p} \tag{6.2}$$

Where C_p and n_p are temperature dependent material constants that are summarized at Table 6-2. We have used equivalent strains; thus, these two values are used in scalar version. Constitutive modeling of creep deformation has been a heavily researched area due to its importance in the prediction of fatigue life of electronic packages. Transient primary creep strains are neglected in this study as they cause negligible damage in thermal cycling. A secondary implicit creep model called General Garofalo (hyperbolic sine) law was utilized to describe the creep behavior of the solder material (Eq. 6.3).

$$\dot{\varepsilon_{creep}} = C_1[Sinh(C_2\sigma)]^{C_3}\exp(-\frac{C_4}{T}) \tag{6.3}$$

Here, C_1, C_2, C_3, and C_4 are the material constants, and σ and T are equivalent stress and absolute temperature respectively. Creep constants, used in the analysis are listed in Table 6-2.

Table 6-1 : Materials properties used in the finite element study [173]

Material	Elastic Modulus (GPa)	Poisson's ratio	Coefficient of Thermal Expansion (ppm/°C)
BT Material	26	0.39	15
Cu	172.90	0.35	14.3
Molding Material	15.79	0.30	9
Solder alloy	43.7-0.0223*T (°K)	0.31	18.3
Silicon	191	0.30	2.33
Underfill	3	0.30	6
Die Attach [174]	1.24	0.40	80
IMCs [24]	132	0.31	18

Table 6-2 : Nonlinear constitutive properties of solder and Cu.

Material	**Plastic Constants** [175]		**Creep Constants** [176]			
Solder alloy	C_p 121.6-0.4*T (°C)	n_p 0.29-0.00046*T (°C)	C_1 (sec^{-1}) 441000	C_2 (MPa^{-1}) 0.005	C_3 4.2	C_4 (°K) 5400
Cu	Yield Stress (σ_y) 172.3 MPa	Tangent Modulus 517.1 MPa				

6.4 Finite Element Analysis

A three-dimensional global-local finite element modeling approach [177,178] is used to reduce the model size without affecting the response of critical joints. This global-local modeling technique was also employed to reduce computational cost and time. The local model helps to investigate the stress/strain responses of the critical part of a model correctly with higher mesh density. Global finite element model was developed in ANSYS 14.5 using ANSYS parametric design language (APDL) programming to identify the critical micro-bump in the package and also to record the boundary conditions for the local modeling. The local model was then used to conduct the numerical experiment by varying local parameters such as geometry, and IMC thickness. The global-local modeling approach is described in detail in the next sections.

6.4.1 Global Modeling

Symmetry in bond position and package geometry was utilized to reduce the size of the model to a quarter size of the package. The considered quarter package contains a single row of 57 micro-bumps with a 0.085µm pitch along the longer side. To further reduce the size, only the slice that contained the micro-bumps was modeled. (Figure 6-2). At the symmetry planes, the displacements were constrained along the perpendicular direction. Also, the geometrically central point was fixed in all DOFs to avoid free body motion. The meshing of the global model was done using SOLID185 element that has the capability of modeling plasticity, creep, large

deflection and large strain. Mesh density sensitivity is a critical issue in the finite element simulation of dissimilar materials due to the singularity [62]. Stress based mesh sensitivity analysis was conducted by refining the mesh and selected mesh density (99510 elements with 121716 nodes) was found to be sufficient. The global model contained the molding material, silicon, underfill, half-sectioned Cu pillar, solder, die attach material, and the substrate. Perfect adhesion is assumed at all material interfaces. The micro bumps were designed as cross-sectioned cylinder, containing solder in between two Cu pillars. Due to the small size of the IMC thickness compared to the other package dimensions and to reduce the number of degrees of freedom, IMC layers were not modeled in the global model.

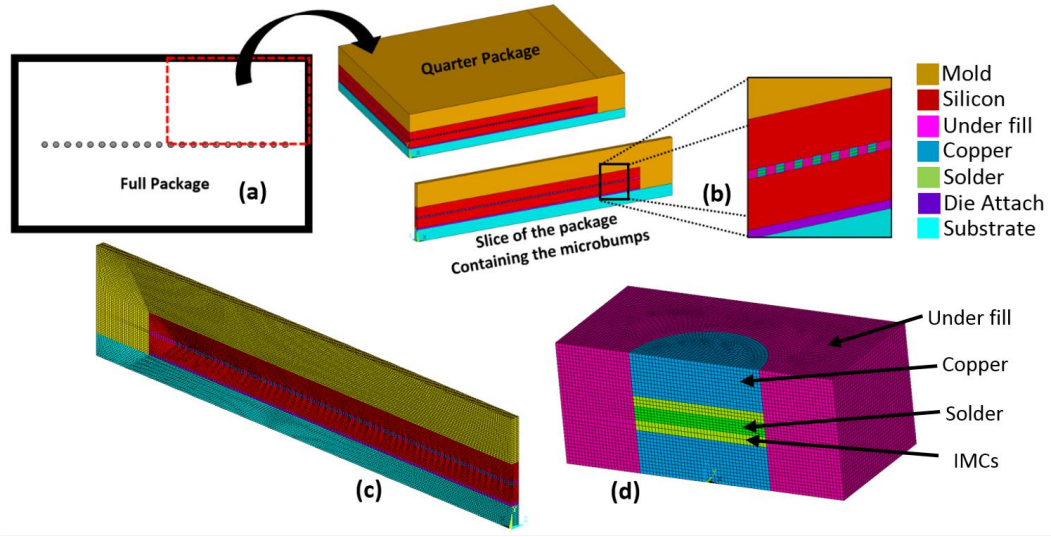

Figure 6-2 : (a) Schematic top view of the package, (b) Quarter model, showing the materials used in the model, (c) shows the global meshed model, and (d) shows local meshed model with the materials considered in the analysis.

The package was investigated under thermal cyclic loading condition from -40°C to +125°C (Figure 6-3). Three thermal cycles are enough to predict the inelastic strain accumulation per

cycle [179]. Thermal loading began at room temperature (298°K) and was selected as the initial stress-free condition for the model. One thermal cycle completes in 60 minutes where ramp time and dwell time was taken to be 15 minutes, with a temperature loading/unloading rate of 11°K/min. The dwell time was kept longer to observe the creep characteristics completely. Stress-strain histories were monitored in all the solder bumps and after three thermal cycles, the critical joint was found at the end of the joint row/edge of the die. The end micro bump showed maximum accumulation of plastic strain after three thermal cycles. Figure 6-4 shows the von Mises stress at 125°C and equivalent plastic strain accumulation after three thermal cycles. All the displacements components at the nodes surrounding this joint were recorded to be used as boundary conditions in the local model.

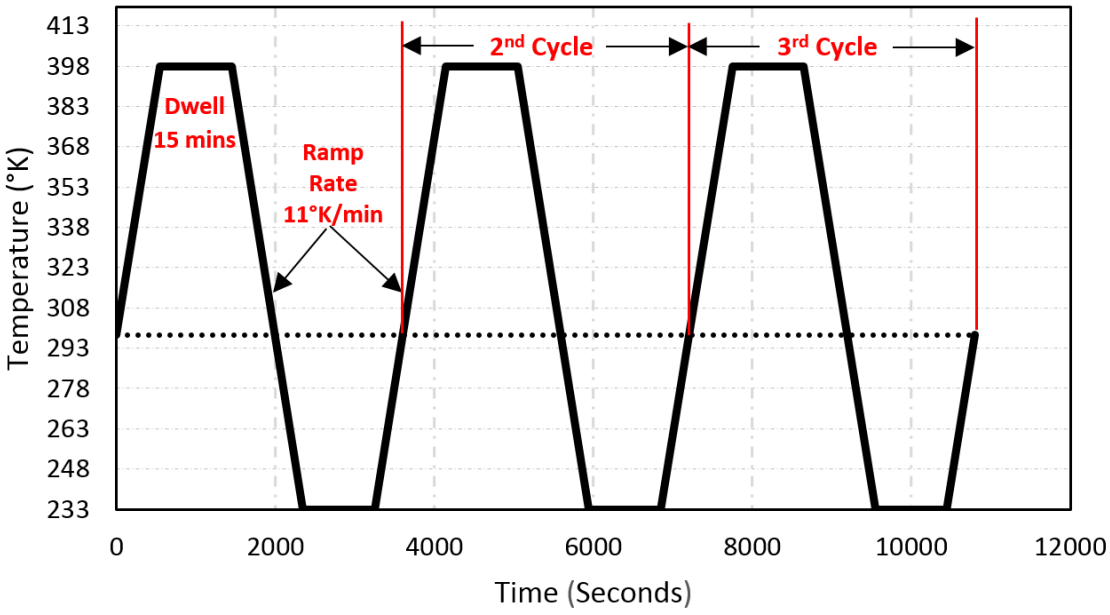

Figure 6-3 : Temperature cycle used in the FE analysis.

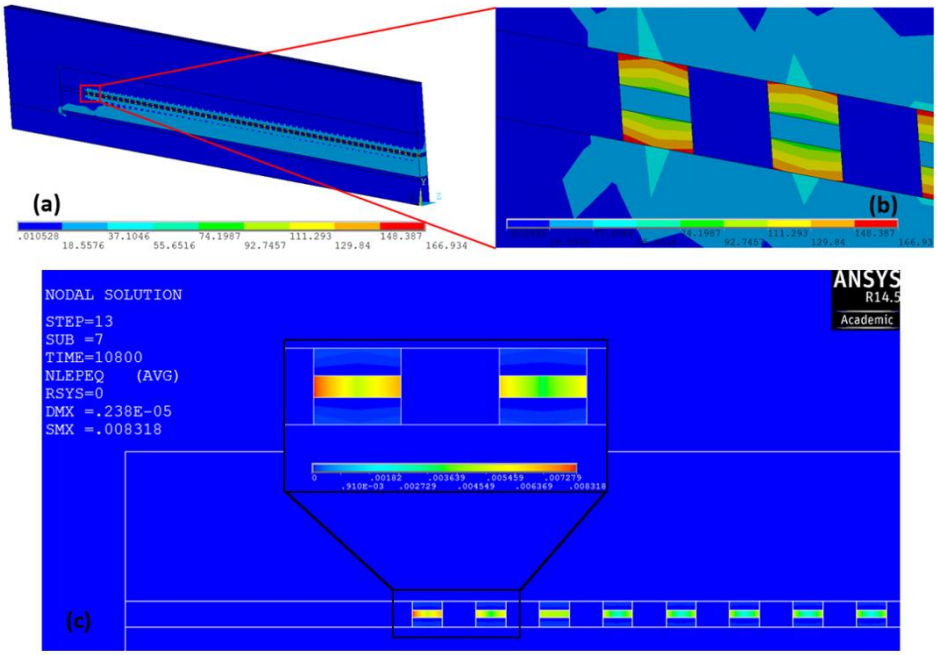

Figure 6-4 : von Mises Stress contour plot (in MPa) at 125°C of (a) Global slice model, (b) In the solder bump area. Figure (c) is showing the equivalent plastic strain contour plots at critical region after three thermal cycles.

6.4.2 Local Modeling

In the SEM image, it was observed that due to high bonding pressure, solder was squeezed out. It is hypothesized that the changes in solder geometry may affect the stress/strain accumulation in the micro-bump. An analysis was conducted to compare the results of using 'perfect solder' and 'squeezed out solder' for the local fatigue life prediction model. The Surface evolver [180] software was used to simulate the formation of the squeezed out solder (Figure 6-5) by defining the proper boundary conditions and minimizing the surface energy. Solder volume in the bonding was calculated from the SEM image by assuming that the squeezed out solder produces a perfect torus that surrounds the bond area. All other dimensions were utilized, and an initial cylindrical model was created. Surface tension and density of the solder were taken from literature [181]. Bonding pressure was applied at the top Cu pad area. After the

simulation, surface evolver provides the stable structure of the bonding region. It can be understood by comparing Figure 6-1 and Figure 6-5 that surface evolver was successful to predict the micro solder bump dimensions for the squeezed out solder bump. The dimensions were then used to model the 'squeezed out' solder geometry in ANSYS.

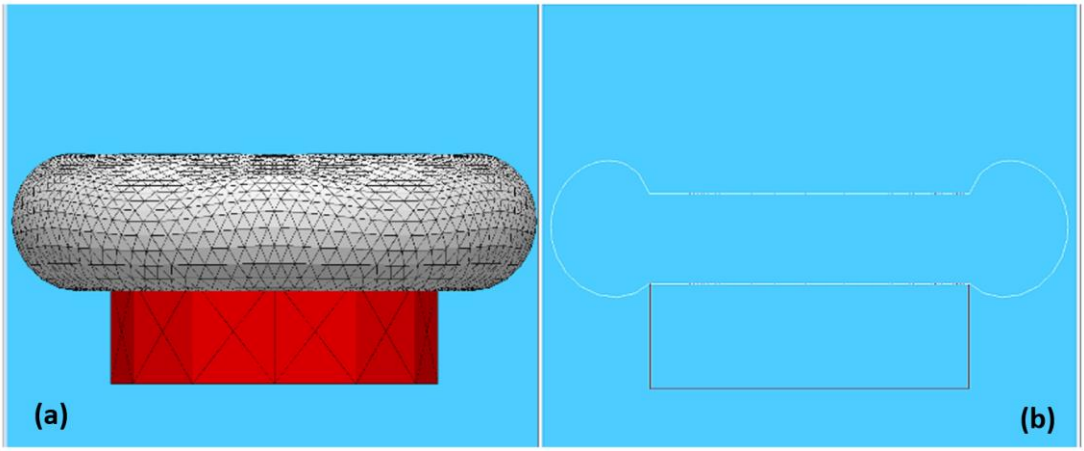

Figure 6-5 : (a) Surface evolver plot of the predicted bump structure after pressure application, (b) figure showing the cross section of the bump structure at the center.

Two local models were created, and both micro solder bumps were assumed to be IMCs free for this analysis. The boundary conditions were implemented, and stress-strain development in the micro solder bump were monitored. The stress and inelastic strain observations were utilized to predict the effect of solder geometry on the fatigue life prediction.

To investigate the effects of material properties and thickness of the IMCs, an IMC layer with the elastic properties was included at the top and bottom of the solder/pad interfaces. Moreover, the thickness of the IMC layers were assumed to be uniform along the interfaces and perfectly joined with the adjacent materials. The materials in the bump area were considered void and porosity free. Usually, IMC materials show exponential growth during the thermal cycling due

to aging [12]. However, as the joints are cycled and IMC growth is occurring, due to fatigue damage softening of solder material is occurring at the same time [182,183]. To be realistic both effects must be considered. This two phenomenon are counteracting (softening of joint due to damage and hardening caused by the IMC growth) and their results may be canceling each other. An extensive analysis must be conducted to include both effects through damage evolution that is beyond the scope of this study [178]. Therefore, for this study, the growth is not modeled. However, the phase growth due to aging cannot be considered during the FE analysis. In this study, the IMC layer thicknesses were assumed to be constant in every model. A numerical design of experiment (NDoE) was developed to capture and investigate the effects of IMC layer thickness on the mechanical behavior of the perfect micro-bump (Table 6-3). Total standoff height of the micro-bump was taken to be 35μm found in the SEM images, and micro solder bond thickness was taken as 10μm, and the layer thickness was stated as a percentage of the bond thickness. IMC layer thickness was varied from 'no IMCs' to '80% IMC' thickness. 'No IMCs' model was considered to observe the effects of not including IMC properties during fatigue life estimation. FE simulations were performed for every test set and the simulated stress/strain results in the third cycle were further used for the fatigue life estimation.

Table 6-3 : Numerical Design of Experiment (NDoE) for the FE analysis of the perfect micro-bump.

Test Set number	**% thickness of bulk solder alloy**	**% thickness of IMC layer**
1 (Base model)	100 (Only solder)	0 (No IMCs)
2	80	20
3	60	40
4	40	60
5	20	80

6.4.2.1 Fatigue Life Prediction Model

The concept of the fatigue life models is to determine the number of cycles that can be endured by the solder bumps and more specifically the solder material before failure occurs. Several fatigue models based on stress, strains, damage, and energy were proposed for solder joints. The energy-partitioning and Coffin-Manson approach integrated with finite element analysis are suggested to predict the mean failure time of micro bumps [184,185]. FE simulated strain results for each test set were taken into consideration to predict the fatigue life of the critical micro-bump. Inelastic strain range model proposed by Coffin-Manson was used to predict the fatigue life of the critical micro-bump for each test set due to its simplicity and reliability in predicting the solder fatigue life [59,173,186]. According to this method, the total number of cycles to failure can be defined by total inelastic strain range per cycle through the following equation:

$$N_f = C_1(\Delta\varepsilon_{acc,eqv}^{in})^{C_2} \quad \textbf{(6.4)}$$

Where C_1 and C_2 are material constants. A value of 27.63 and -1.08 was used for C_1 and C_2 respectively [179]. $\Delta\varepsilon_{acc,eqv}^{in}$ is the total equivalent inelastic strain accumulated at the third stable cycle. For each test, total equivalent inelastic strains increment was obtained by summing the equivalent plastic and creep strain part for the third stable cycle using the following equation:

$$\Delta\varepsilon_{acc,eqv}^{in} = \Delta\varepsilon_{acc,eqv}^{pl} + \Delta\varepsilon_{acc,eqv}^{cr} \quad \textbf{(6.5)}$$

To observe the effects of IMC thickness on fatigue life of Cu pillar consequently, Coffin-Manson model was used which has the following form [187]:

$$N_f = C_4\left(\Delta\varepsilon_{acc,eqv}^{pl}\right)^{C_3} \quad \textbf{(6.6)}$$

In the above equation, C_3 is fatigue ductility exponent which is taken as -1.66 for electroplated Cu [187] and C_4 is 0.22 for electroplated Cu [188]. $\Delta\varepsilon_{acc,eqv}^{pl}$ is the plastic strain range per cycle accumulated in Cu region.

After calculating fatigue life for each model, the effects of the IMC thickness on the fatigue life of the micro solder bump and Cu pillar are discussed.

6.5 Results and Discussions

6.5.1 Effects of Solder Joint Geometry

von Mises stress is a scalar measure often used to understand how a material behaves at a complex loading condition. The equation of von Mises stress has many forms, however the most common form is given here that is used in the finite element software [127]:

$$\sigma_{VM} = \sqrt{\frac{1}{2}\left[\left(\sigma_{xx} - \sigma_{yy}\right)^2 + \left(\sigma_{yy} - \sigma_{zz}\right)^2 + (\sigma_{zz} - \sigma_{xx})\text{^}2\right] + 3\left(\tau_{xy}^2 + \tau_{yz}^2 + \tau_{zx}^2\right)} \quad (\mathbf{6.7})$$

Here, σ's are the widely known stress components.

Equivalent plastic strain is a scalar measure of the effective plastic strain defined through time integration of the equivalent plastic strain rate. Equivalent plastic strain rate is calculated by the finite element software using the following equation [127]:

$$\dot{\varepsilon^{eqv,pl}} = \sqrt[\frac{2}{2}]{\varepsilon_{ij}^{pl} : \varepsilon_{ij}^{pl}} \quad \textbf{(6.8)}$$

Here, ε_{ij}^{pl} is the strain tensor components. Figure 6-6 shows the von Misses stress and equivalent plastic strain contour plots for two models. Average equivalent plastic and creep strain increment over the thermal cycling time are plotted for both perfect and squeezed out solder model in Figure 6-7. Possible failure regions were identified where the total accumulated inelastic strains are higher, and the strains were averaged over a limited number of elements belonging to the damage volumes to avoid singularity (Figure 6-6-c, d). It is evident that squeezed out micro solder bump shows less plastic and creep accumulation after three thermal cycles. It transmits stresses and strains to the squeezed-out portion of the solder thus accruing smaller stress, plastic, and creep strain compared to perfect solder model. Due to low inelastic strain accumulation per cycle, squeezed out solder provides higher fatigue life. It can be concluded that using perfect micro solder bump model would predict lower fatigue life of the critical bump. Therefore, to be more conservative, the remaining analysis and investigation of the effects of IMC thickness are conducted on a perfect model.

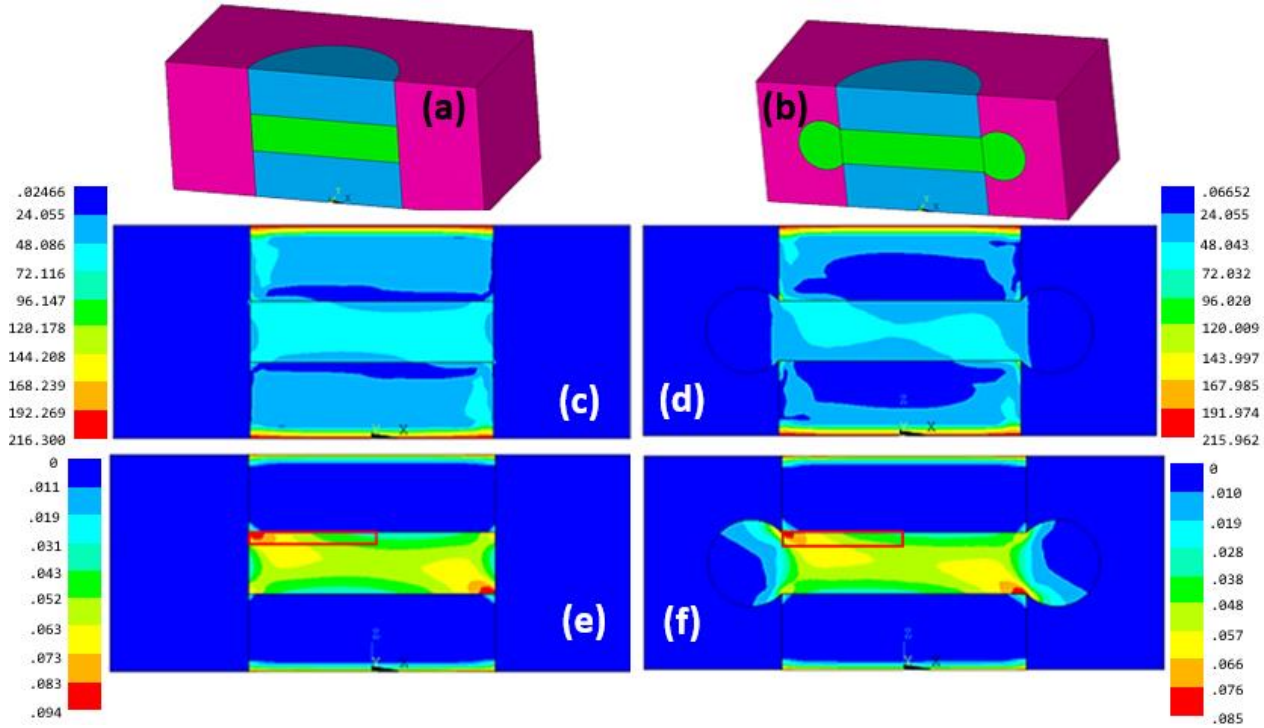

Figure 6-6 :(a) Perfect micro solder bump model, (b) squeezed out micro solder bump model, (c) & (d) are the von Mises stress contour plot (in MPa), (e) & (f) are the equivalent plastic strain contour plots showing the critical regions used to extract results. All plots are at the end of three thermal cycles.

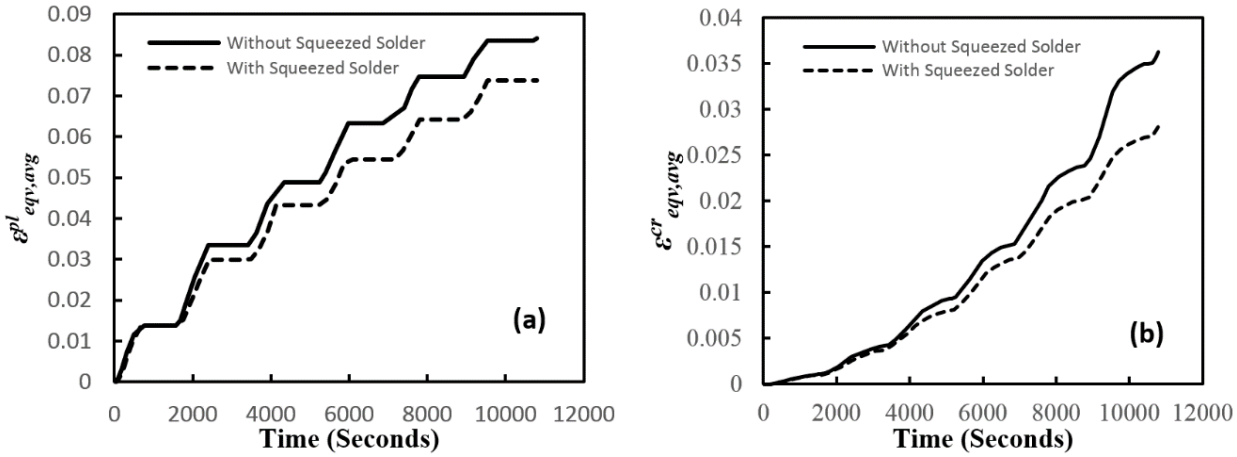

Figure 6-7: Comparison of (a) equivalent plastic strains and (b) equivalent creep strains accumulation in both 'perfect' and 'squeezed out' micro solder bump model.

6.5.2 Effects of IMC Thickness on Accumulated Stress-Strain

Figure 6-8 shows the developed average shear stress in the center of the solder with respect to time for different thicknesses of IMCs. The shear stress history of all test models follows the imposed thermal cycling condition [189]. It can be seen that with the increase of IMC thickness, bulk solder tends to carry higher shear stresses during the beginning of the ramp step from +125°C to -40°C. The shear stress amplitude is larger for larger IMC thickness. Higher shear stress incorporates higher shear strain in the bump that degrades the fatigue life.

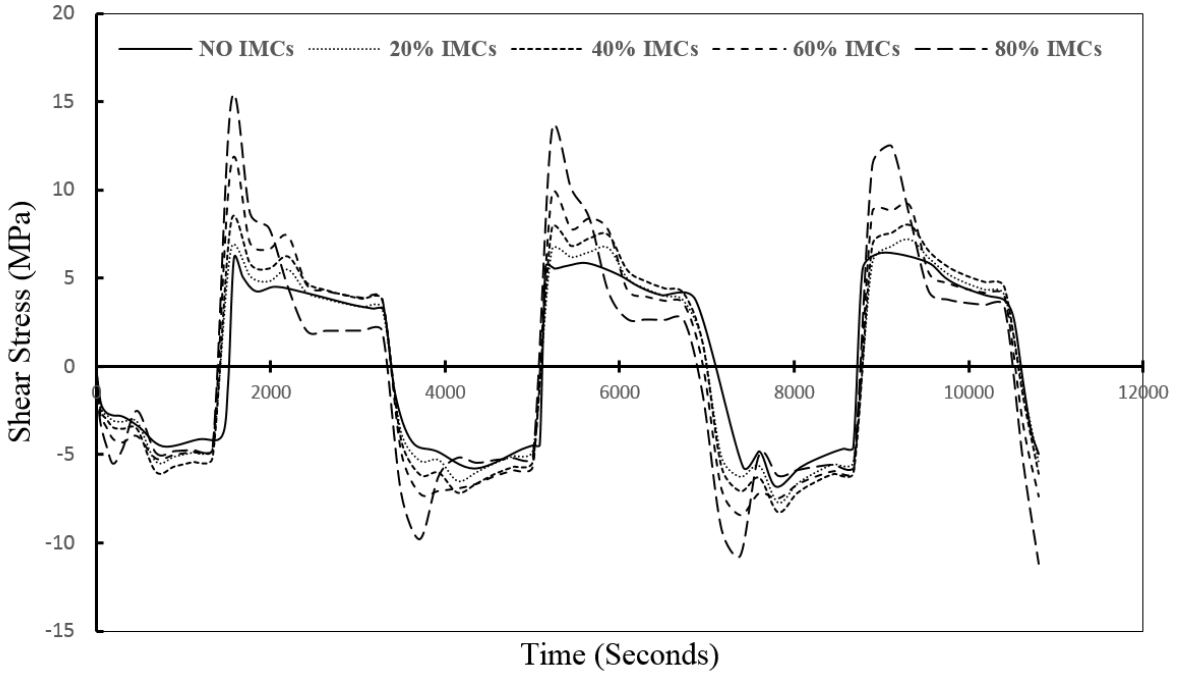

Figure 6-8 : Average shear stress Vs. Time in the middle of the micro solder bump.

Based on the accumulated inelastic strain criteria, critical location in the micro-bump found to be the corner of the bulk solder region at the solder/IMC interfaces due to the highest inelastic strain accumulation after three thermal cycles. Figure 6-9 contains the history of accumulated equivalent plastic strains ($\varepsilon_{eqv,avg}^{pl}$) and equivalent creep strains ($\varepsilon_{eqv,avg}^{cr}$) at the critical

location over the time. To avoid the effect of singularity, the strains are averaged over a limited number of elements belonging to a damage volume. Notably, $\varepsilon_{eqv,avg}^{pl}$ increases highly when IMC was considered in the model compared to 'No IMCs' model. Similar observation has been reported in the literature [59]. Moreover, $\varepsilon_{eqv,avg}^{pl}$ continues to increase with the increase in IMC thickness but the increase seems to decline when higher IMC thickness is considered. For instance, $\varepsilon_{eqv,avg}^{pl}$ increases 17% when 20% IMC thickness is considered and compared to 'No IMCs' model at the end of the third thermal cycle. However, only 4.5% increase in $\varepsilon_{eqv,avg}^{pl}$ is observed when IMC thickness changes from 60% to 80%. $\varepsilon_{eqv,avg}^{cr}$ displays the similar behavior shown in Figure 6-9b. The increase in $\varepsilon_{eqv,avg}^{cr}$ is very high when 20% IMC considered and compared to No IMCs model. An increase in the $\varepsilon_{eqv,avg}^{cr}$ is also observed with the increase in IMC thickness. Maximum equivalent creep strain does not show any noticeable changes in the first cycle with the increase in IMC thickness. However, the effects of IMC thickness on the strain become evident at the next cycles (Figure 6-9c, Figure 6-9d). Several researchers found similar behavior in their findings [56,59]. In their cases, they considered small IMC thickness with the large volume fraction of bulk solder alloy in the solder ball. The effect of IMC inclusion was minimal in their study as the volume fraction of IMC was still small compared to the volume fraction of bulk solder. However, in micro solder bumps, due to larger volume fraction of the IMCs compared to bulk solder, IMC presence tends to significantly affect the micro solder bump strain accumulation in comparison to solder balls. In other words, the effect seems to be much more profound when smaller micro solder bump is considered.

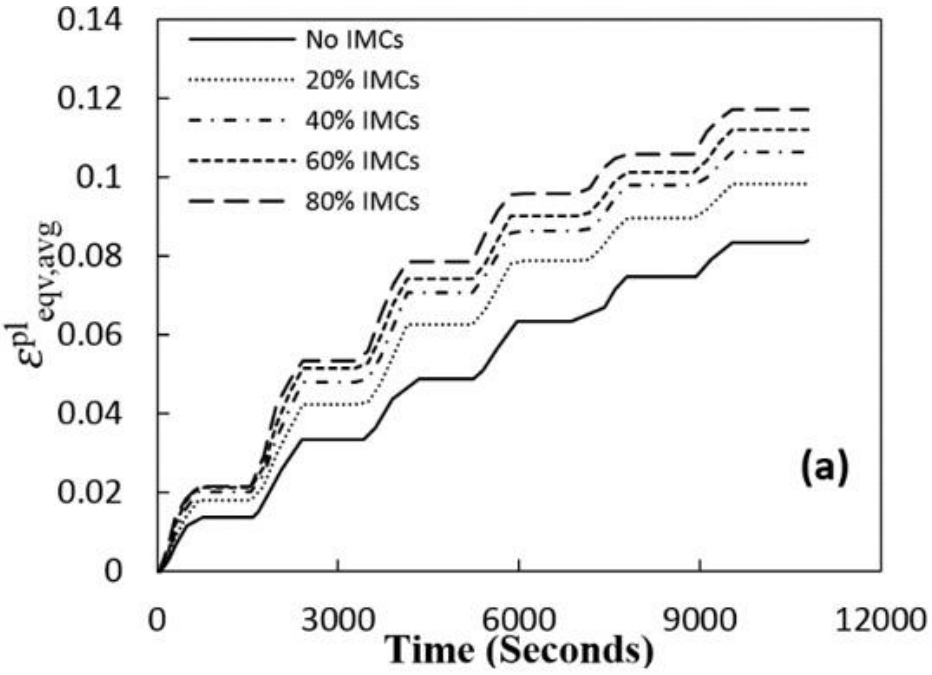
0.14
0.12
0.1
0.08
0.06
0.04
0.02
0
$\varepsilon^{pl}_{eqv,avg}$
No IMCs
20% IMCs
40% IMCs
60% IMCs
80% IMCs
(a)
0
3000
6000
9000
12000
Time (Seconds)

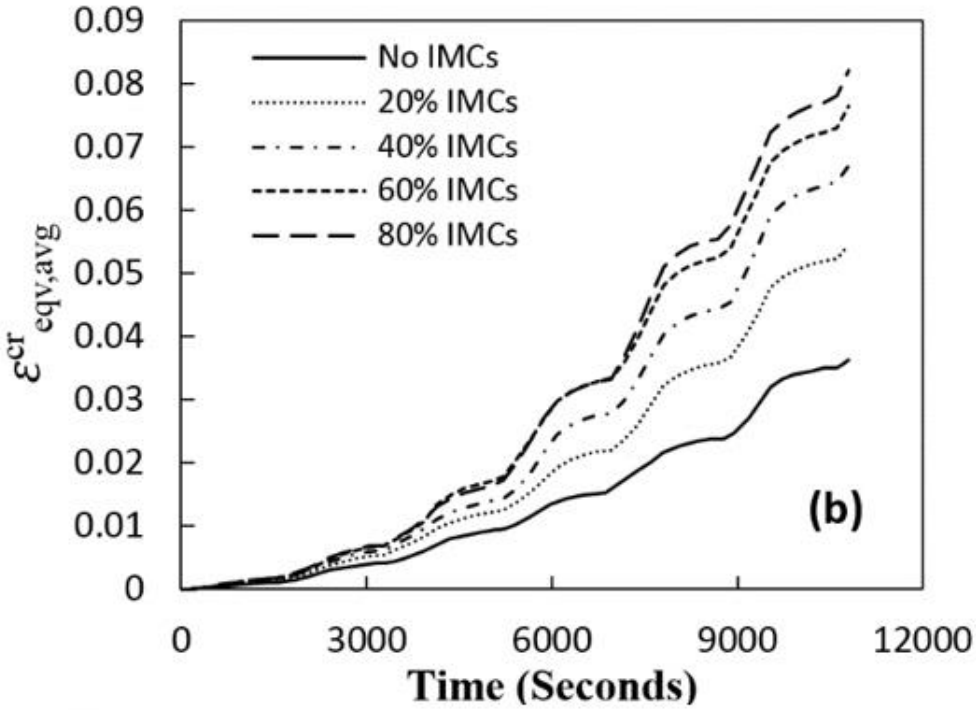
0.09
0.08
0.07
0.06
0.05
0.04
0.03
0.02
0.01
0
$\varepsilon^{cr}_{eqv,avg}$
No IMCs
20% IMCs
40% IMCs
60% IMCs
80% IMCs
(b)
0
3000
6000
9000
12000
Time (Seconds)

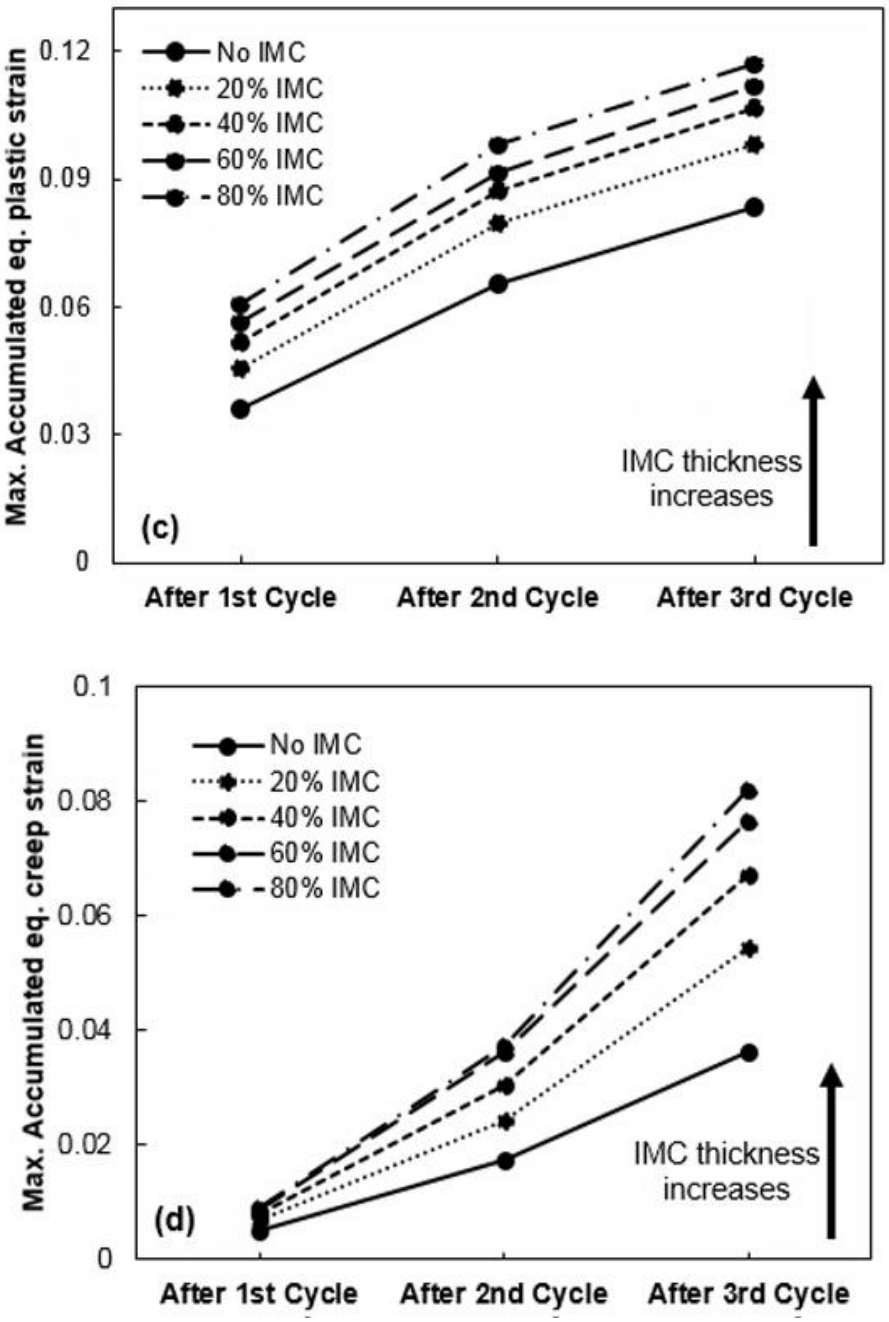

Figure 6-9: History of (a) accumulative equivalent plastic strains, and (b) accumulative equivalent creep strains at the critical corners of the micro-bump in solder region for three thermal cycles. Figure (c) and (d) shows maximum accumulated equivalent plastic and creep strain respectively after each cycle.

However, the linear increase in IMC thickness imposes a nonlinear increase in plastic and creep strain accumulation. The equivalent inelastic strain range per cycle increases rapidly during the initial increase in IMC thickness but tends to reach an asymptotic value at the higher IMC thickness. Due to the hard and brittle nature of the IMCs, stresses and strains tend to redistribute more at the Cu region when a higher IMC volume fraction is present in the bump. This is evident in the Figure 6-10 and contour plot of equivalent plastic strain in Figure 6-11. Total equivalent inelastic strain range per cycle tends to increase for both Cu and solder but it increases rapidly for Cu than solder when higher IMC thickness is considered. It can be hypothesized that when the bond has a high volume fraction of IMCs or completely transforms into IMCs, Cu most likely will experience plastic deformation and crack may initiate at Cu pillar region.

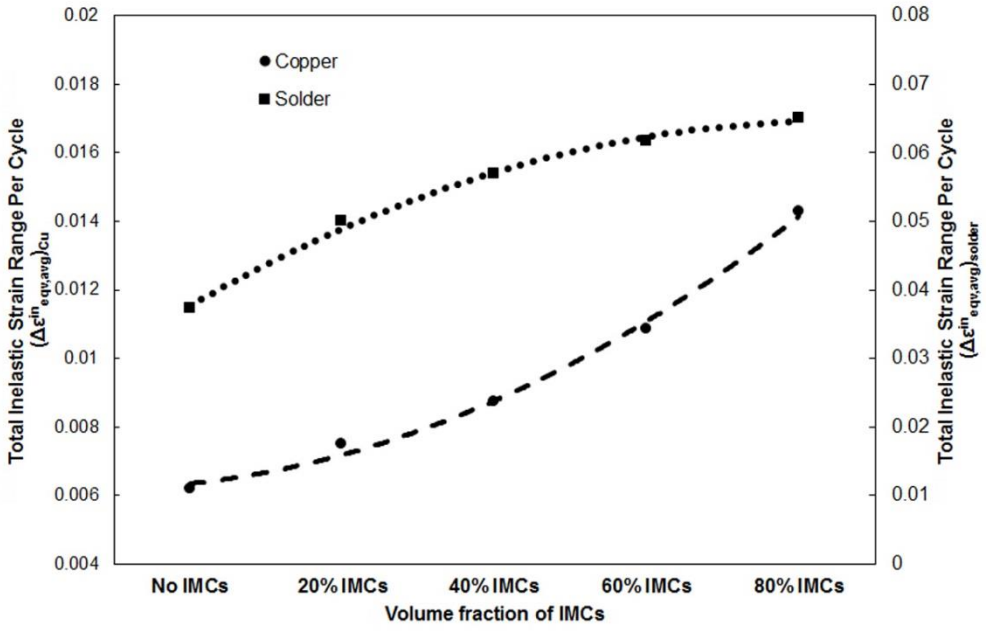

Figure 6-10 : Total equivalent inelastic strain range per cycle after 3 thermal cycles for solder and Cu region.

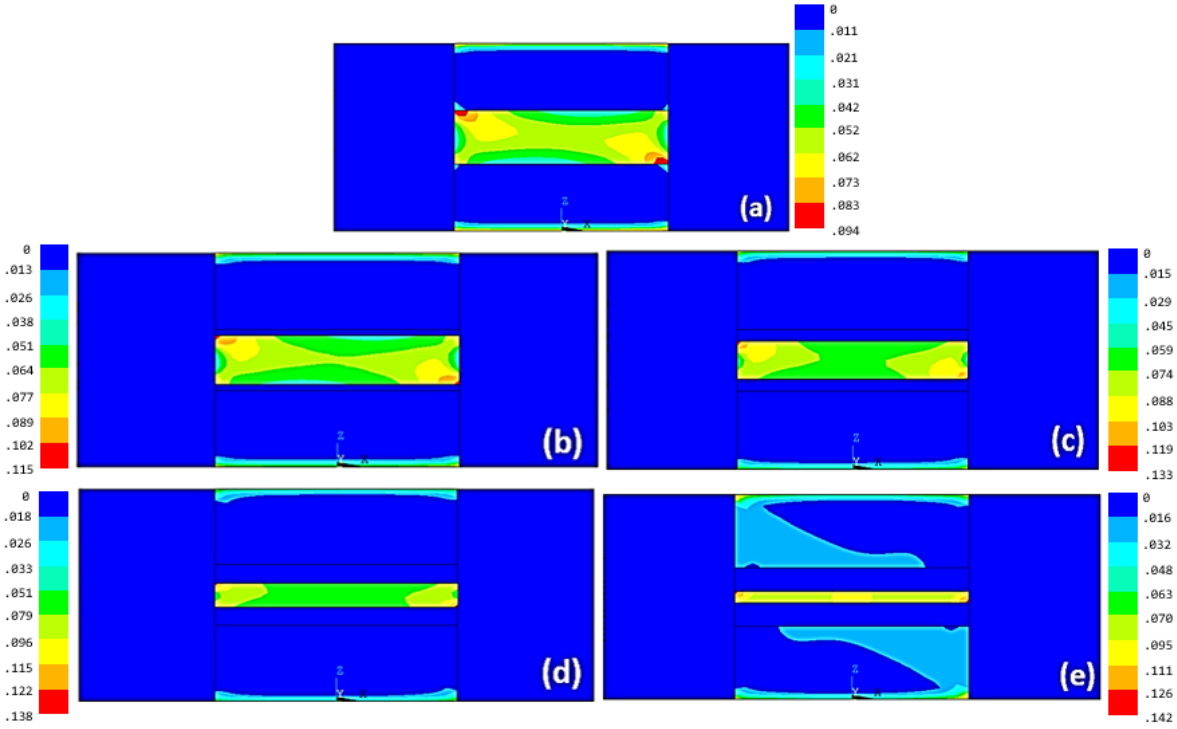

Figure 6-11 : Contour plot of equivalent plastic strain distribution after three thermal cycles for (a) No IMCs, (b) 20% IMCs, (c) 40% IMCs, (d) 60% IMCs, and (e) 80% IMCs model.

6.5.3 Effects of IMC Thickness on Fatigue Life

Figure 6-12 plots the comparison of the fatigue life cycles for 5 test sets in both Cu and solder. The fatigue life for solder was calculated using Eq. 6.4 and 6.5 using the inelastic strain based approach. Coffin- Manson model with constant parameters described by Eq. 6.6 was used to calculate the electroplated Cu fatigue life. It is clear that IMC thickness would have a greater impact on the fatigue life of micro bumps. Overall, thicker IMC layers result in a lower micro-solder bump fatigue life, which is consistent with the results published in literature [56,59]. However, Chen et al. [57] predicted the opposite behavior. Cu fatigue life was also observed to be decreasing with the increase in IMC thickness in our study. Our analysis show that adding 20% IMC in the model reduces the solder fatigue life prediction to about 27% compared to the case of No IMCs. Lu and his group [45] have investigated the effects of different IMC layer

thickness on the fatigue life of fine-pitch Cu/Ni/SnAg micro-bump with 5 μm total thickness. They varied the IMC layer thickness from 1.25 μm to 2 μm by varying the bonding temperature from 250°C to 300°C. Thermal cyclic tests (TCT), and High Temperature Storage (HTS) tests revealed that micro-bumps fabricated with bonding temperature of 300°C failed within 1250 cycles where specimens fabricated with bond temperature of 250°C did not fail after 2000 cycles. The effects may be even worse when major portion of the volume fraction of IMCs will be present. Solder fatigue life computed for 80% IMC gives about 45% less life cycles than No IMCs model. This decrease in fatigue life seems to follow an exponential decay path. This may be due to the increase in plastic strain accumulation at Cu pillar with the increase in IMC volume fraction. Cu tends to deform more when higher IMC thickness is observed. It is observed that Cu fatigue life decreases rapidly when thicker IMCs are considered in the model. It can be hypothesized that crack may initiate in Cu rather than the bond region when bulk solder turns completely into IMCs. When IMC thickness, greater than 40% is considered in the model, Cu tends to provide lower fatigue life in cycles than solder. In that case, we may need to consider the fatigue life prediction model of Cu with the solder to design and predict the fatigue life of micro-bump more accurately. Further experimental investigations are needed to explain the fatigue life behavior of micro solder bumps with higher volume fraction of IMCs and complete IMC bonds.

Analyzing the simulation results, it is obvious that the presence of IMCs must be considered in the FE simulation of micro solder bump for fatigue life prediction to generate more reasonable and correct results. Also, it is necessary to control the IMC layer thickness during

bump fabrication process in order to design or estimate the fatigue life of micro-bump quantitatively.

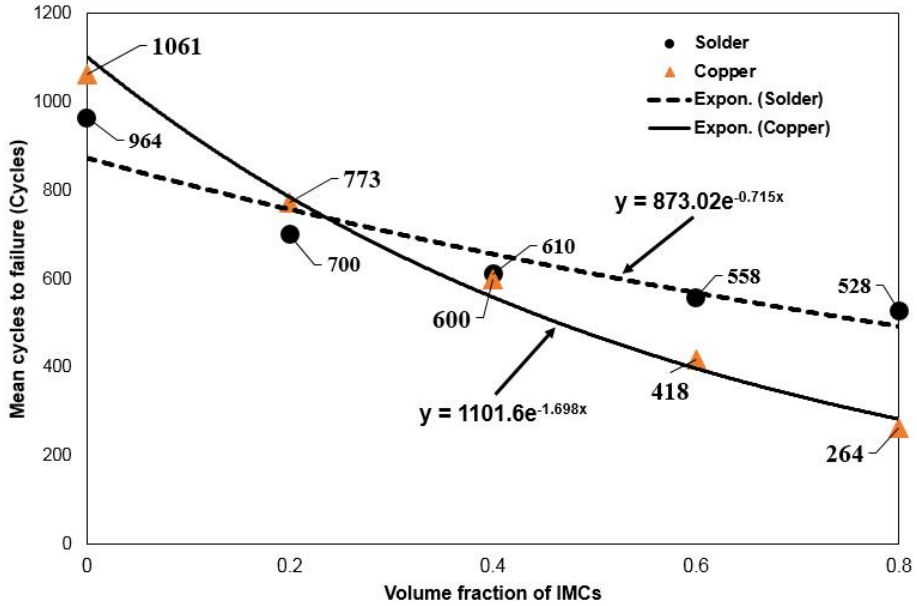

Figure 6-12 : Predicted mean cycles to failure due to fatigue for Cu and solder with different volume fraction of IMCs in the model.

6.6 Summary and Conclusions

This study investigates the effects of micro solder bump geometry and IMC thickness on the thermo-mechanical fatigue life of microelectronic interconnects through FE analysis. Due to the different mechanical properties of IMCs, it is hypothesized that the presence of IMCs may alter the thermo-mechanical fatigue behavior during the thermal cycling loading. The analysis reveals that it has a large effect on the fatigue life prediction of micro solder bumps with smaller bond thickness. The findings of the work are summarized below:

- A stress/strain relaxation is evident when a squeezed-out micro solder bump model is considered and compared to a perfect micro solder bump. Due to lower plastic and creep

strain accumulation, this geometry appears to deliver higher fatigue life. However, large volumes squeezing out of the solder is not desired as it may create short circuits in fine pitch bumps.

- IMC thickness has a significant impact on the plastic and creep strain accumulation in solder. The strains accumulation are observed to be increasing with the increase in IMC thickness in the models.
- Fatigue life cycles are clearly over estimated when no IMCs are considered in the FE analysis. The increase in IMC layer thickness appears to introduce an exponential decay of solder and Cu fatigue life for the considered micro-bump. On the other hand, during thicker IMC model test, Cu provided lower fatigue life in cycles than solder. It can be hypothesized that when there is a high volume fraction of IMCs or the bond completely transforms into IMCs, Cu most likely will experience plastic deformation and crack may initiate at Cu pillar region. Therefore, fatigue life prediction model for Cu along with solder may need to take into consideration when a very high volume fraction of IMCs or complete IMCs in the bond region is observed.
- It is very important to control the thickness of the IMC layer during the fabrication process to design or estimate the fatigue life of micro-bump in microelectronic packages.

From the study, it has been observed that the effect of IMCs thickness is more pronounced when a solder bump has a higher volume fraction of IMCs. Further experimental investigation should be conducted to ensure the influences of IMCs on the reliability of microelectronic packaging interconnects.

CHAPTER 7 : Summary, Contributions & Future Works

7.1 Summary

Solder joints are the most common interconnects found in microelectronic packages. Currently, research and development are going on to increase the reliability of interconnects. Many reliability issues are arising due to the down-scaling of the micro-scale solder joints. On the other hand, these small-scale solder joints have higher volume fractions of hard and brittle IMCs. Moreover, small joints comprise of only a few grains of Sn and Cu_6Sn_5 IMCs. Crystal structure of Sn and Cu_6Sn_5, as well as their large grain microstructure introduce anisotropy. This anisotropic behavior incorporates complexities in designing and predicting the mechanical behavior of solder joints. Anisotropy of Sn has been studied significantly in literature. However, very few studies were conducted to understand the anisotropy of Cu_6Sn_5 IMC. This Ph.D. research was aimed to characterize the anisotropy of Cu_6Sn_5 IMC and study the effects of IMCs on the overall mechanical behavior of microscale solder joints by both simulations and experiments. The most important observations of this study are provided below:

Cu_6Sn_5 is the main IMC compound observed in all fabrication processes of Sn-based solder interconnects. A miniaturized solder joint has a few Cu_6Sn_5 grains. Due to their scale differences, bulk properties of Cu_6Sn_5 cannot portray the actual behavior at grain level. Some of the grain scale mechanical properties and slip parameters of single grain Cu_6Sn_5 were not available in literature which necessitated a grain-level mechanical characterization. A combined nanoindentation and EBSD analysis technique were utilized to determine the microscopic mechanical properties. A preferred grain growth direction along *c-axis* was observed during EBSD analysis. Five grains with different orientations along normal to the *c-axis* were selected to perform the nanoindentation tests. Nanoindentation load vs. depth curves were recorded for each grain, and Young's modulus and hardness were calculated. A reverse analysis proposed by Dao et al. [74] was employed to predict the yield strength and strain hardening exponent. Experimental results indicate that the hardness values of the grains were not affected by the variation in crystallographic orientation along normal to the *c-axis*. A relatively lower yield strength was found when indentation was along (0001) basal plane.

Literature review suggests that at small scale, traditional FE analysis is not capable of predicting the micro-mechanical behavior of the solder joint accurately. CPFE analysis provides more accurate prediction at micro-scale as it takes crystallographic slip properties of the crystal into account. There are a few studies based on CPFE method where Sn anisotropy was taken into consideration, though the effects of IMCs were ignored. It is obvious that inclusion of IMCs are necessary for efficient modeling when the solder joint has a high volume fraction of IMCs. However, information regarding Cu_6Sn_5 IMC's crystallographic slip parameters such as critical resolved shear stress, initial hardening modulus, and saturation

stress are not available in the literature. These parameters are needed to model the crystal plasticity behavior of Cu_6Sn_5 IMC using CPFE analysis. A combined strategy based upon nanoindentation experiments, CPFE modeling, and comparative analysis was proposed to predict the crystallographic slip parameters. Critical resolved shear stress was calculated using Schmid's law. The nanoindentation experiment performed in the single crystal was mimicked in ABAQUS software. Several computational analyses were performed to predict the initial hardening modulus and saturation stress by fitting the computational results with the experimental results. Thus, a complete set of crystallographic slip parameters were proposed to predict the actual behavior of Cu_6Sn_5 single crystal by CPFE analysis.

The slip parameters extracted in the previous step were then used to develop a CPFE model of the Cu_6Sn_5 IMC compound. A complete CPFE computational model of a joint was developed by incorporating the crystal plasticity behavior of Sn, Cu_6Sn_5 IMC, and the isotropic behavior of Cu substrate. The developed model was validated by the published single lap-shear experimental results. The study illustrates that CPFE model is more capable in predicting the shear behavior of the solder joints than the traditional FE model. The CPFE model of the joint was then utilized to understand how different IMC thicknesses affect the overall shear behavior of the solder joints. A computational design of experiment was established where the Cu_6Sn_5 IMC thicknesses were varied from no IMC to 80% IMCs. Numerical shear tests were performed at the same shear strain rate for all models. The computational analysis shows that with the increase in IMC thickness, the shear responses change from "low stiffness- low strain hardening" to "higher stiffness-high strain hardening". This phenomenon may be due to the increase in the volume fraction of the hard and brittle Cu_6Sn_5 IMC, which limits the

deformation greatly and contributes to higher shear yield strength along with higher shear modulus. The simulation results introduce the necessity of the experimental research to understand the effects of different IMC thicknesses on the shear behavior of solder joints.

Inspired by the simulation results, a lap-shear experiment has been designed and conducted to investigate the effects of different volume fraction of IMCs on the shear behavior of micro-scale solder joints with a 50μm stand-off height. To investigate the local shear strain behavior, an optical technique along with an image processing computer program was utilized. The study shows that the ultimate shear strength and strain to failure are largely dependent on the volume fraction of IMCs. Experimental results confirms the simulation observations where solder joints with higher IMC thickness show a stiffer response and increase in shear strength. Fractography analysis showed failure mode changing from ductile to brittle. Crack propagation path been modulated by the different volume fraction of IMCs.

Effects of IMC volume fraction on the thermo-mechanical fatigue behavior of solder bonds were also studied through finite element analysis. Outcomes show that high volume fraction of IMCs could degrade the fatigue life of the solder bonds. Overall, it is obvious that the presence of IMCs must be considered for micro solder bump with a smaller bond thickness in fatigue life prediction model to generate more reasonable and correct results.

7.2 Contributions

This dissertation provides a clear idea of how IMCs can be degrading to the mechanical reliability of micro scale solder bonds. New information regarding the reliability of solder bonds has been delivered to the microelectronic research community.

1. Effects of the anisotropy of Sn is well established, however, the microstructural and anisotropic mechanical behavior of Cu_6Sn_5 IMC is not well studied. The first contribution of the dissertation is the complete characterization of mechanical anisotropy of Cu_6Sn_5 IMC at the grain level. On the other hand, a preferred grain growth direction for Cu_6Sn_5 IMC along *c-axis* was observed on polycrystalline Cu substrate using EBSD technique and reported to the community. These observations will surely serve in the investigation on reducing the anisotropy and increasing the overall reliability of the solder joints.
2. Crystallographic slip parameters such as critical resolved shear stress, initial hardening modulus, and saturation stress are necessary to model the single crystal plasticity behavior of a material. These information was not available in the literature for Cu_6Sn_5 IMC. This study reports the slip system parameters for three most active slip systems of Cu_6Sn_5 which were obtained by implying combined strategy based on nanoindentation experiments, modeling, and comparative analysis.
3. A complete CPFE model was developed to predict the micro-mechanical behavior of the solder interconnects. The model takes the anisotropic behavior of Sn and Cu_6Sn_5 grains into account and is thus able to give insights on how the anisotropy could affect the overall mechanical behavior of the solder interconnects. Moreover, the effects of the increase in IMC thickness were also investigated, and the study showed a major influence of IMC volume fraction on the determination of overall mechanical behavior. Overall, the developed CPFE model can be a useful computational tool for studying the anisotropy and overall mechanical behavior more precisely.
4. A semi-DIC technique was developed to observe the local shear displacements in solder joints during single lap-shear tests. This low-cost technique was able to predict the local

shear behavior of micro scale solder joints at the micro scale. And it was observed that the far-field or nominal shear strain measured from the crosshead displacements was significantly different than the local shear strain.

5. This research work reports how high volume fraction of IMCs could affect the shear behavior of solder bonds. The study showed that the ultimate shear strength and strain to failure are largely dependent on the volume fraction of IMCs. Fractography analysis indicated a ductile to brittle fracture mode transition along with the dominant interfacial delamination that was witnessed when the solder joints had a higher volume fraction of IMCs than bulk solder.
6. The dissertation contributes towards understanding how degrading IMCs are to the thermo-mechanical fatigue reliability of the micro solder bumps found in 3-D ICs where the micro solder bumps have only a few microns of bond thicknesses. A computational modeling approach was utilized to investigate the effects of IMC thickness on thermos-mechanical fatigue reliability, and it was observed that fatigue life decreases with the increase in IMC thickness.
7. The developed semi-DIC technique can be further utilized to measure the local shear displacement in determining adhesion strength of adhesives, epoxy resins, coating, etc.
8. The CPFE model developed for HCP crystal in this Ph.D. study can be used for other HCP crystals such as Titanium, Magnesium, etc.

7.3 Suggestions for Future Works

Based on the insights obtained by this work, future research and developments are suggested to improve the experiments and modeling procedures accomplished in this dissertation.

1. The CPFE model developed a base model for micro-mechanical behavior study that is based on crystallographic slip behavior. This model does not take dislocations, defects, grain boundary sliding, and other microstructural properties into account. The model can thus be further developed to become more versatile and accurate by including other microstructural properties.
2. CPFE model that is developed in this study can predict the mechanical behavior of solder joints at the room temperature. Investigation of different thermal loading conditions using the CPFE modeling technique is not conducted and could be an important area for future investigation.
3. The lap-shear tests were performed at room temperature to observe the effects of IMC thickness on the local shear behavior of solder joints. The shear behavior may change drastically with the influence of high temperature. Similar experiments at higher temperature are needed to be conducted to investigate the effects of IMC presence on shorter stand-off height solder joints. It could be a key interest for future studies.
4. The single lap-shear experiment can be further utilized to observe the shear behavior of solder bonds at higher shear strain rates ($1s^{-1}$~$100s^{-1}$). Higher shear strain rates could show how the solder bond is going to perform at drop or shock load when it has a very high volume fraction of IMCs.
5. In the single lap-shear test, the utilized semi-DIC technique could be further developed by using more powerful imaging technique such as SEM. Performing the *in situ* test inside an SEM chamber would provide further microscopic information regarding local strain development. Tests at a smaller scale with more powerful strain measurement technique are suggested to be performed in future.

6. Effects of higher volume fraction of IMCs on the tensile behavior of micro-scale solder bond also needs to be investigated although tensile failure is very rare in microelectronic packaging interconnects. However, it may provide an interesting insight on how ductility of the solder bond could be affected by the large volume fraction of IMCs.
7. During the FE analysis, the effects of IMC thickness on the thermo-mechanical fatigue behavior were observed to be critical for designing and predicting the fatigue life of solder interconnects. Further experiments should be conducted in future to establish a reliable fatigue life model that includes the effects of IMC thickness.
8. IMCs tend to grow due to electromigration that occurs under continuous high current flow through the solder interconnects. Under this condition, electromigration can lead to the electrical failure of solder interconnects in a relatively short period. Electromigration study on the solder bonds with high volume fraction of IMCs has not been studied yet. This could be a major contribution to the reliability study of solder interconnects in microelectronic packaging.

APPENDIX A

Plastic properties (Yield strength, σ_y and Strain Hardening Exponent, n) Extraction from Nanoindentation Load-Depth Curve Properties

Elastic properties such as Young's modulus and hardness can be directly extracted from the nanoindentation tests using the empirical equations. However, plastic properties cannot be determined directly from the test. A reverse analysis procedure proposed by Dao et al. [74] is a very well-known technique to extract the plastic properties from the indentation data. The values of σ_y and n can be determined for the majority of cases by this reverse analysis, provided that the assumption of power law hardening sufficiently represents the full uniaxial stress–strain response.

Dao's model proposed two dimensionless function developed by using Buckingham π theorem. The details can be found in the article published by Dao et al. [74]. First dimensionless function, $\boldsymbol{\pi_1}$ is obtained by correlating the load with the indentation data and can be expressed as:

$$\boldsymbol{\pi_1 = \sigma_r h^2 \mathrm{f}\left(\frac{E_r}{\sigma_r}, n\right) = P} \qquad \textbf{(A.1)}$$

The P value at the loading curve can be described as: $P = Ch^2$ where C is the loading curvature and can be directly obtained from the load-depth curve. Equation A.1 can thus be written as:

$$\boldsymbol{\pi_1 = \sigma_r f\left(\frac{E_r}{\sigma_r}, n\right) = \frac{P}{h^2} = C} \quad \textbf{(A.2)}$$

A representative strain, ε_r = 0.033 was identified so that the corresponding dimensionless function $\boldsymbol{\pi_1}$, normalized with respect to $\sigma_{0.033}$ was found to be independent of the strain hardening exponent *n*. This simplifies the equation for the dimensionless function to:

$$\boldsymbol{\pi_1 = f\left(\frac{E_r}{\sigma_{0.033}}\right) = \frac{C}{\sigma_{0.033}}} \quad \textbf{(A.3)}$$

Complete listing of the function, $\boldsymbol{\pi_1}$ is given in the end of the Appendix. The equation A.3 then solved to determine the representative stress, $\boldsymbol{\sigma_{0.033}}$.

After determining $\boldsymbol{\sigma_{0.033}}$, a second dimensionless function, $\boldsymbol{\pi_2}$ was derived by correlating the unloading slope or stiffness, $\frac{dP_u}{dh} = S$ with the indentation data and can be express as:

$$\boldsymbol{\pi_2 = E_r h_m f\left(\frac{E_r}{\sigma_r}, n\right) = S} \quad \textbf{(A.4)}$$

This equation can be written as:

$$\boldsymbol{\pi_2 = f\left(\frac{E_r}{\sigma_{0.033}}, n\right) = \frac{S}{E_r h_m}} \quad \textbf{(A.5)}$$

This equation can be utilized to determine the strain hardening exponent, *n.* Complete listing of the function, $\boldsymbol{\pi_2}$ is given in the end of the Appendix.

Yield strength, $\boldsymbol{\sigma_y}$ at zero offset strain can then be calculated after finding $\boldsymbol{\sigma_{0.033}}$ and *n* using the following equation:

$$\boldsymbol{\sigma_{0.033} = \sigma_y\left(1 + \frac{E}{\sigma_y}\varepsilon_{0.033}\right)^n} \quad \textbf{(A.6)}$$

This equation is based on the assumption that the material follows power hardening law. A more detailed process flow is given below which explains the steps related in calculating the plastic properties.

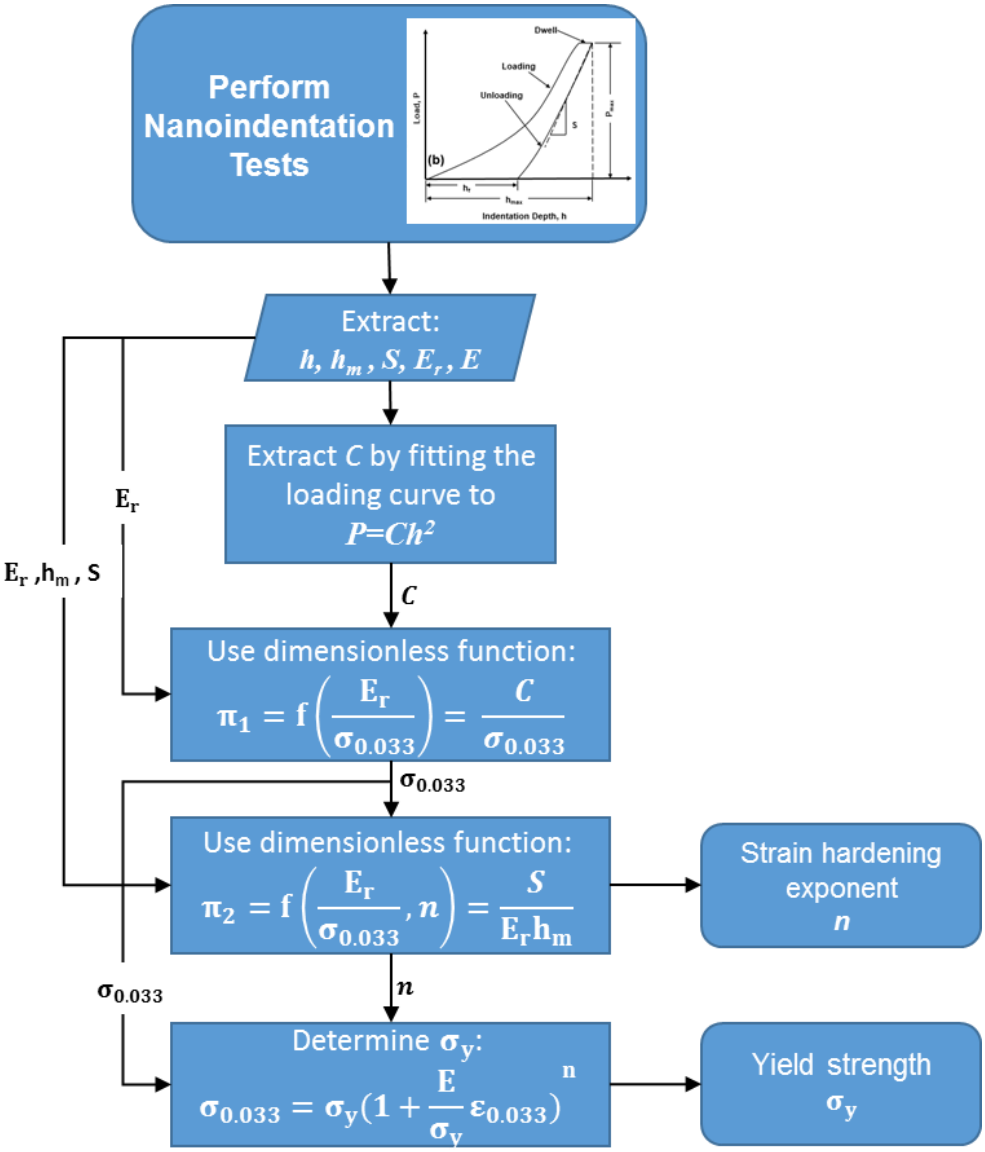

Figure A: Process flow of determining plastic properties using Dao reverse analysis

Dimensionless function, π_1

$$\pi_1 = \frac{C}{\sigma_{0.033}} = -1.131\left[\ln\left(\frac{E_r}{\sigma_{0.033}}\right)\right]^3 + 13.635\left[\ln\left(\frac{E_r}{\sigma_{0.033}}\right)\right]^2 - 30.594\left[\ln\left(\frac{E_r}{\sigma_{0.033}}\right)\right] + 29.267$$

Dimensionless function, π_2

$$\pi_2 = \left(\frac{E_r}{\sigma_{0.033}}, n\right) = \frac{1}{E_r h_m}\frac{dP}{dh} = (-1.40557n^3 + 0.77526n^2 + 0.15830n - 0.06831)\left[\ln\left(\frac{E_r}{\sigma_{0.033}}\right)\right]^3$$
$$+ (17.93006n^3 - 9.22091n^2 - 2.37733n + 0.86295)\left[\ln\left(\frac{E_r}{\sigma_{0.033}}\right)\right]^2$$
$$+ (-79.99715n^3 + 40.55620n^2 + 9.00157n - 2.54543)\left[\ln\left(\frac{E_r}{\sigma_{0.033}}\right)\right]$$
$$+ (122.65069n^3 - 63.88418n^2 - 9.58936n + 6.20045)$$

APPENDIX B

Procedure to Prepare Computer Workstation to Work with User Material (UMAT) Subroutine

Setting up the system to work with User material (UMAT) subroutine is a challenging task. Following procedure needs to be followed sequentially to prepare the computer workstation and Abaqus software to work with User material subroutine. This procedure is prepared for Abaqus 6.12-1 version, along with Intel Fortran compiler 11.1 and Microsoft visual studio 2009 and for a computer with xp-64 bit processor. Compatibility of FORTRAN compiler and visual studio needs to be verified from *http://www.3ds.com/support/certified-hardware/simulia-system-information/*

Description

To setup the system, the sequence of performing setup needs to be consistent as it will set the environment path variables properly. First, we need to install the following programs in the following order:

1. Install Visual Studio 2009 (Full version)
2. Install Intel Fortran Compiler -11.1 (Full version)
3. Install Abaqus 6.12-1

After installing all programs, we can verify if everything is properly installed or not. To do that, go to:

Start -> Programs -> Abaqus 6.12-1 -> Right click on Abaqus Verification -> Click on Properties

This should pop-up a window like the following:

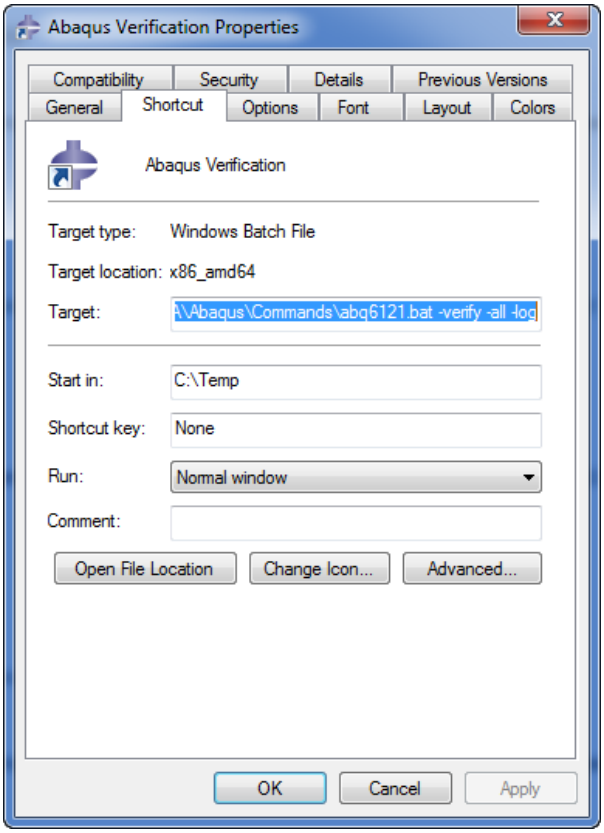

Figure B: Screenshot of the properties window

The target needs to be changed with:

"C:\Program Files (x86)\Microsoft Visual Studio 9.0\VC\bin\x86_amd64\vcvarsx86_amd64.bat" &
"C:\Program Files (x86)\Intel\Compiler\11.0\072\fortran\Bin\intel64\ifortvars_intel64.bat" &&
C:\Simulia\Abaqus\Commands\abq6121.bat -verify -all –log

Click Ok. Click on the Abaqus verification to verify the installation. We have to make sure that there is no FAIL messages related to three installed programs.

Next step is to set Abaqus/CAE to run the subroutine from CAE. To do that, we have to go to:

Start -> Programs -> Abaqus -> Right click on Abaqus CAE -> Click on Properties

We have to change the target to the following:

"C:\Program Files (x86)\Microsoft Visual Studio 9.0\VC\bin\x86_amd64\vcvarsx86_amd64.bat" && "C:\Program Files (x86)\Intel\Compiler\11.0\072\fortran\Bin\intel64\ifortvars_intel64.bat" && C:\Simulia\Abaqus\Commands\abq6121.bat cae || pause

Click OK.

Then, we will set the Abaqus command Prompt to run the subroutine. To do that:

Go to Start -> Programs -> Abaqus -> Right click on Abaqus Command Click on Properties

"C:\Program Files (x86)\Microsoft Visual Studio 9.0\VC\bin\x86_amd64\vcvarsx86_amd64.bat" & "C:\Program Files (x86)\Intel\Compiler\11.1\072\Bin\intel64\ifortvars_intel64.bat" && C:\Windows\SysWOW64\cmd.exe /k

To enable debugging of user subroutine, we have to open abaqus_v6.env file saved in C:\SIMULIA\Abaqus\6.12-1\SMA\site\ and under “compile_fortran”, we have to add ‘/Od’. This will enable debugging of user subroutine.

After everything is setup correctly, we can open Abaqus CAE and use the UMAT feature with Fortran written subroutines.

APPENDIX C

Method to Measure the Local Shear Displacement at Micro-scale by Optical-Computational Method

A method has been developed to measure the *in situ* local shear displacement at micro-scale during single lap-shear test of solder joints. The developed system consists of:

- Sharp scriber (scalpel blade #11)
- Optical microscope (20x) with a live-view computer program
- Software to capture the live test screen as a video format
- MATLAB image toolbox plugin

At first, a very thin line (~25µm) was scribed with the scalpel blade at the exposed joint side and the line covered both Cu substrate and solder joint area. Then, the microscope was placed at the top of the tensile stage. The lap shear specimen was mounted at the tensile stage in such a way that the scribed region remained under the microscope. After achieving the best focus, microscope image software with live-view option was turned on. A screen capturing software with capability of saving the live-view screen as a video format was setup to record the test. The lap-shear test was conducted and the *in situ* test was recorded at 30 fps. MATLAB programing software was utilized to post-process the recorded video.

A program package has been develop to assist in further post-processing process in measuring the local shear displacement. The package consists of three MATLAB script files called: (a)

GetImage.m, (b) PixelValue.m, and (c) CalDistance.m. A brief description of each script is given below:

(a) GetImage.m: This MATLAB program loads the video file and split it into images at a suggested second interval. The captured images are then saved in .png format in a prescribed folder. At the same time, this program converts the RGB images to binary images and save them as .png format. Binary images have good scribed line visibility.

(b) PixelValue.m: Pixel value in μm is necessary to calculate the distance between two points in the image. The pixel value is calculated by this program where it takes a base image into account and user needs to place the popped-up measuring bar on the top of the embedded calibration scale in the image. This calculates the dimension of each pixel in μm and save it as a parameter. This parameter can be called in the next program to measure the distance.

(c) CalDistance.m: This written MATLAB program takes each image at a time and user needs to place the popped-up measuring bar at the two opposite edges of the scribed line (one should be at the top/bottom Cu substrate and another at the bottom/top Cu substrate). The distance is then calculated by diving the number of pixels between the two points with the pixel value calculated at the previous program. The program continuously takes each images on by one and saves the calculated distances in an array.

These MATLAB scripts are used to measure the local displacements of the separated lines which approximately provide the local shear displacements. These shear displacements correspond to the displacement at specific test times. The test time can then be correlated with the load-time data recorded during the lap-shear test. Local shear strains are calculated by dividing the shear displacements with the joint thickness.

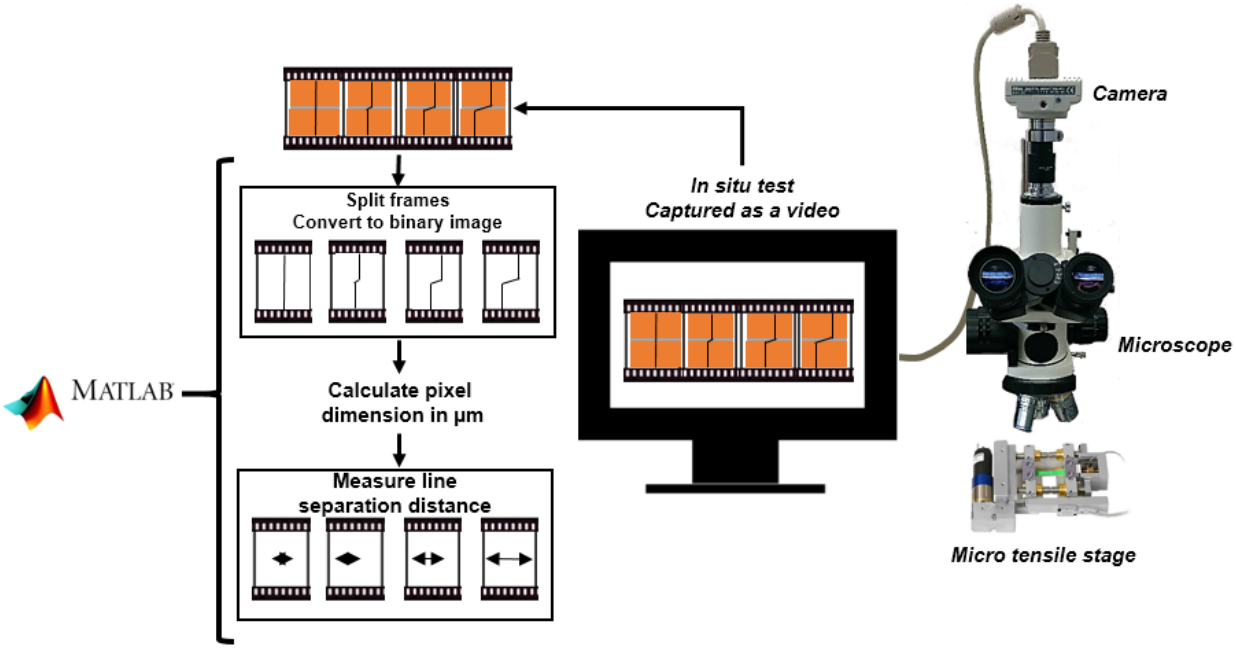

Figure C: Process flow showing major steps of developed optical-computer program technique to measure the local shear displacements.

REFERENCES

[1] K.. Tu, K. Zeng, Mater. Sci. Eng. R Reports 34 (2001) 1.

[2] Y. Qi, H.R. Ghorbani, J.K. Spelt, IEEE Trans. Adv. Packag. 29 (2006) 690.

[3] P. Vianco, in:, Proc. Tech. Progr. Surf. Mt. Int., San Jose, CA, 1993.

[4] K.J. Puttlitz, K.A. Stalter, Handbook of Lead-Free Solder Technology for Microelectronic Assemblies, CRC Press, 2004.

[5] P. Vianco, J. Rejent, R. Grant, Mater. Trans. 45 (2004) 765.

[6] F.X. Che, W.H. Zhu, E.S.W. Poh, X.W. Zhang, X.R. Zhang, J. Alloys Compd. 507 (2010) 215.

[7] C.M.L. Wu, D.Q. Yu, C.M.T. Law, L. Wang, Mater. Sci. Eng. R Reports 44 (2004) 1.

[8] L. Zhang, S. Xue, L. Gao, G. Zeng, Z. Sheng, Y. Chen, S. Yu, J. Mater. Sci. Mater. Electron. 20 (2009) 685.

[9] Https://www.ameslab.gov/files/LeadFreeSolder_Foundation.pdf, (2010).

[10] K.-W. Moon, W.J. Boettinger, U.R. Kattner, F.S. Biancaniello, C.A. Handwerker, J. Electron. Mater. 29 (2000) 1122.

[11] M.N. Islam, A. Sharif, Y.C. Chan, J. Electron. Mater. 34 (2005) 143.

[12] O.M. Abdelhadi, L. Ladani, J. Alloys Compd. 537 (2012) 87.

[13] N. Chawla, Int. Mater. Rev. 54 (2009) 368.

[14] K.E. Yazzie, J.J. Williams, N.C. Phillips, F. De Carlo, N. Chawla, Mater. Charact. 70 (2012) 33.

[15] A. Larsson, L. Stenberg, S. Lidin, Acta Crystallogr. B 50 (1994) 636.

[16] J.-M. Song, B.-R. Huang, C.-Y. Liu, Y.-S. Lai, Y.-T. Chiu, T.-W. Huang, Mater. Sci. Eng. A 534 (2012) 53.

[17] T. Laurila, V. Vuorinen, J.K. Kivilahti, Mater. Sci. Eng. R Reports 49 (2005) 1.

[18] D. Mu, H. Huang, K. Nogita, Mater. Lett. 86 (2012) 46.

[19] M.H. Yoo, Metall. Trans. A 12 (1981) 409.

[20] V. Hasija, S. Ghosh, M.J. Mills, D.S. Joseph, Acta Mater. 51 (2003) 4533.

[21] K. Nogita, C.M. Gourlay, T. Nishimura, JOM 61 (2009) 45.

[22] L. Jiang, H. Jiang, N. Chawla, J. Electron. Mater. 41 (2012) 2083.

[23] W. Zhou, L. Liu, P. Wu, Intermetallics 18 (2010) 922.

[24] P.-F. Yang, Y.-S. Lai, S.-R. Jian, J. Chen, R.-S. Chen, Mater. Sci. Eng. A 485 (2008) 305.

[25] D.R. Frear, JOM 48 (1996) 49.

[26] G.-Y. Jang, J.-W. Lee, J.-G. Duh, J. Electron. Mater. 33 (2004) 1103.

[27] R.R. Chromik, R.P. Vinci, S.L. Allen, M.R. Notis, Jom 55 (2003) 66.

[28] X. Deng, N. Chawla, K.K. Chawla, M. Koopman, Acta Mater. 52 (2004) 4291.

[29] X. Li, F. Li, F. Guo, Y. Shi, J. Electron. Mater. 40 (2010) 51.

[30] T.Y. Lee, W.J. Choi, K.N. Tu, J.W. Jang, S.M. Kuo, J.K. Lin, D.R. Frear, K. Zeng, J.K. Kivilahti, J. Mater. Res. 17 (2002) 291.

[31] B.L. Chen, G.Y. Li, Thin Solid Films 462-463 (2004) 395.

[32] P. Liu, P. Yao, J. Liu, J. Alloys Compd. 470 (2009) 188.

[33] M. Sona, K.N. Prabhu, J. Mater. Sci. Mater. Electron. 25 (2014) 1446.

[34] O.M. Abdelhadi, L. Ladani, J. Electron. Packag. 135 (2013) 021004.

[35] J. Amistoso, A.V. Amorsolo, IEEE Trans. Components Packag. Technol. 32 (2009) 405.

[36] X. Hu, Y. Li, Y.Y. Liu, Y.Y. Liu, Z. Min, Microelectron. Reliab. 54 (2014) 1575.

[37] L. Yang, Z.F. Zhang, J. Electron. Mater. 44 (2014) 590.

[38] T. An, F. Qin, Microelectron. Reliab. 54 (2014) 932.

[39] H.-T. Lee, M.-H. Chen, H.-M. Jao, T.-L. Liao, Mater. Sci. Eng. A 358 (2003) 134.

[40] X. Deng, R.S. Sidhu, P. Johnson, N. Chawla, Matallurgical Mater. Trans. A 36 (2005) 55.

[41] Y.J. Chen, C.K. Chung, C.R. Yang, C.R. Kao, Microelectron. Reliab. 53 (2013) 47.

[42] C. Chen, L. Zhang, J. Zhao, L. Cao, J.K. Shang, J. Electron. Mater. 41 (2012) 2487.

[43] Y.-H. Lee, H.-T. Lee, Mater. Sci. Eng. A 444 (2007) 75.

[44] K.N. Bhat, K.N. Prabhu, Satyanarayan, J. Mater. Sci. Mater. Electron. 25 (2014) 864.

[45] S.-T. Lu, J.-Y. Juang, H.-C. Cheng, Y.-M. Tsai, T.-H. Chen, W.-H. Chen, S. Lu et al., IEEE Trans. Device Mater. Reliab. 12 (2012) 296.

[46] Y. Liu, F. Sun, L. Luo, C.A. Yuan, G. Zhang, J. Electron. Mater. 44 (2015) 2450.

[47] N. Chawla, Y.-L. Shen, X. Deng, E.S. Ege, J. Electron. Mater. 33 (2004) 1589.

[48] F. Ochoa, X. Deng, N. Chawla, J. Electron. Mater. 33 (2004) 1596.

[49] X. Zhang, E.H. Wong, C. Lee, T.-C. Chai, Y. Ma, P.-S. Teo, D. Pinjala, S. Sampath, Microelectron. Reliab. 44 (2004) 611.

[50] X. Li, Z. Wang, J. Mater. Process. Technol. 183 (2007) 6.

[51] P. Lall, M. Hande, C. Bhat, N. Islam, J. Suhling, J. Lee, Microelectron. Reliab. 47 (2007) 1907.

[52] Y. Tian, X. Liu, J. Chow, Y.P. Wu, S.K. Sitaraman, Microelectron. Reliab. 54 (2014) 939.

[53] T.-Y. Hung, C.-J. Huang, C.-C. Lee, C.-C. Wang, K.-C. Lu, K.-N. Chiang, Microelectron. Eng. 107 (2013) 125.

[54] D. Yu, H. Lee, S. Park, J. Electron. Packag. 134 (2012) 041008.

[55] I. Panchenko, J. Grafe, M. Mueller, K.-J. Wolter, 2013 IEEE 15th Electron. Packag. Technol. Conf. (EPTC 2013) (2013) 318.

[56] F.X. Che, J.H.L. Pang, J. Alloys Compd. 541 (2012) 6.

[57] W.-H. Chen, C.-F. Yu, H.-C. Cheng, Y. Tsai, S.-T. Lu, Microelectron. Reliab. 53 (2013) 30.

[58] H.-C. Cheng, K.-Y. Hsieh, K.-M. Chen, Microelectron. Reliab. 51 (2011) 826.

[59] Y.-C. Chiou, Y.-M. Jen, S.-H. Huang, Microelectron. Reliab. 51 (2011) 2319.

[60] C.-C. Lee, T.-F. Yang, C.-S. Wu, K.-S. Kao, R.-C. Cheng, T.-H. Chen, Microelectron. Eng. 107 (2013) 107.

[61] C.-C. Lee, P.T. Lin, J. Electron. Packag. 136 (2014) 031006.

[62] P.K. Bhatti, in:, 56th Electron. Components Technol. Conf. 2006, IEEE, 2006, pp. 972–980.

[63] S. Park, R. Dhakal, J. Gao, J. Electron. Mater. 37 (2008) 1139.

[64] E. Suhir, Microelectron. Reliab. 53 (2013) 925.

[65] Y.-L. Shen, N. Chawla, E.S. Ege, X. Deng, Acta Mater. 53 (2005) 2633.

[66] J. Gong, Comput. Mater. Sci. 43 (2008) 199.

[67] S. Dumoulin, O. Engler, O.S. Hopperstad, O.G. Lademo, Model. Simul. Mater. Sci. Eng. 20 (2012) 055008.

[68] Y.S. Choi, M.A. Groeber, P.A. Shade, T.J. Turner, J.C. Schuren, D.M. Dimiduk, M.D. Uchic, A.D. Rollett, Metall. Mater. Trans. A 45 (2014) 6352.

[69] F.P.E. Dunne, R. Kiwanuka, A.J. Wilkinson, Proc. R. Soc. A Math. Phys. Eng. Sci. 468 (2012) 2509.

[70] L. Li, L. Shen, G. Proust, C.K.S. Moy, G. Ranzi, Mater. Sci. Eng. A 579 (2013) 41.

[71] P. Darbandi, T. Lee, T.R. Bieler, F. Pourboghrat, Comput. Mater. Sci. 85 (2014) 236.

[72] P. Darbandi, T.R. Bieler, F. Pourboghrat, T. Lee, J. Electron. Mater. 42 (2013) 201.

[73] A. Zamiri, T.R. Bieler, F. Pourboghrat, J. Electron. Mater. 38 (2009) 231.

[74] M. Dao, N. Chollacoop, K.J. Van Vliet, T. a. Venkatesh, S. Suresh, Acta Mater. 49 (2001) 3899.

[75] Http://urus-28.deviantart.com/journal/Electronic-Microscopy-462654632, 2013 (n.d.).

[76] S. Nishikawa, S. Kikuchi, Nature 121 (1928) 1019.

[77] W.H. Bragg, Science (80-.). 40 (1914) 795.

[78] (n.d.).

[79] S.I. Wright, B.L. Adams, Metall. Trans. A 23 (1992) 759.

[80] N.C.K. LASSEN, D.J. JENSEN, K. CONRADSEN, Scanning Microsc. 6 (n.d.) 115.

[81] K.. Tu, Acta Metall. 21 (1973) 347.

[82] O.M. Abdelhadi, A.C. Magee, L. Ladani, J. Adv. Microsc. Res. 8 (2013) 10.

[83] Powder Diffraction File, JCPDS, Newton Square, PA, n.d.

[84] J.O. Suh, K.N. Tu, N. Tamura, Appl. Phys. Lett. 91 (2007) 051907.

[85] W.C. Oliver, G.M. Pharr, J. Mater. Res. 7 (1992) 1564.

[86] J.J. Vlassak, W.D. Nix, J. Mech. Phys. Solids 42 (1994) 1223.

[87] H. Hertz, J. Reine Angew. Math 92 (1881) 110.

[88] A.E.H. Love, Q. J. Math. 10 (1939) 161.

[89] I.N. Sneddon, Int. J. Eng. Sci. 3 (1965) 47.

[90] T. Chudoba, F. Richter, Surf. Coatings Technol. 148 (2001) 191.

[91] G.M. Pharr, a. Bolshakov, J. Mater. Res. 17 (2011) 2660.

[92] J.-M. Song, Y.-L. Shen, C.-W. Su, Y.-S. Lai, Y.-T. Chiu, Mater. Trans. 50 (2009) 1231.

[93] R.J. Asaro, A. Needleman, Acta Metall. 33 (1985) 923.

[94] E.W. Schmid, W. Boas, Plasticity of Crystals, 1950.

[95] R. Hill, J.R. Rice, J. Mech. Phys. Solids 20 (1972) 401.

[96] J.R. Rice, J. Mech. Phys. Solids 19 (1971) 433.

[97] Y. Huang, Harvard Univ. Cambridge, MA Mech. Repo (1991).

[98] E.H. Lee, J. Appl. Mech. 36 (1969) 1.

[99] J. Pan, J.R. Rice, Int. J. Solids Struct. 19 (1983) 973.

[100] U.F. Kocks, Metall. Mater. Trans. 1 (1970) 1121.

[101] D. Peirce, R.J. Asaro, A. Needleman, Acta Metall. 30 (1982) 1087.

[102] P. Kratochvíl, P. Lukáč, B. Sprušil, Czechoslov. J. Phys. 23 (1973) 621.

[103] H.E. Friedrich, B.L. Mordike, Magnesium Technology: Metallurgy, Design Data, Applications, Springer, 2006.

[104] Y. Yang, L. Wang, C. Zambaldi, P. Eisenlohr, R. Barabash, W. Liu, M.R. Stoudt, M. a. Crimp, T.R. Bieler, JOM 63 (2011) 66.

[105] P.A. Sabnis, S. Forest, N.K. Arakere, V.A. Yastrebov, Int. J. Plast. 51 (2013) 200.

[106] S.F. Choudhury, L. Ladani, J. Electron. Mater. 43 (2014) 996.

[107] C. Zambaldi, Y. Yang, T.R. Bieler, D. Raabe, J. Mater. Res. 27 (2011) 356.

[108] J. Gong, A.J. Wilkinson, Acta Mater. 57 (2009) 5693.

[109] M.H. Yoo, S.R. Agnew, J.R. Morris, K.M. Ho, Mater. Sci. Eng. A 321 (2001) 87.

[110] K. Ito, V. Vitek, Philos. Mag. A 81 (2001) 1387.

[111] X.-L. Nan, H.-Y. Wang, L. Zhang, J.-B. Li, Q.-C. Jiang, Scr. Mater. 67 (2012) 443.

[112] A. Chapuis, J.H. Driver, Acta Mater. 59 (2011) 1986.

[113] Y.B. Chun, C.H.J. Davies, Mater. Sci. Eng. A 528 (2011) 3489.

[114] Y.N. Wang, J.C. Huang, Acta Mater. 55 (2007) 897.

[115] A. Gangulee, G.C. Das, M.B. Bever, Metall. Trans. 4 (1973) 2063.

[116] A.K. Bhattacharya, W.D. Nix, Int. J. Solids Struct. 24 (1988) 881.

[117] N.T.S. Lee, V.B.C. Tan, K.M. Lim, Appl. Phys. Lett. 88 (2006) 031913.

[118] U. Borg, J.W. Kysar, Int. J. Solids Struct. 44 (2007) 6382.

[119] F. Roters, P. Eisenlohr, L. Hantcherli, D.D. Tjahjanto, T.R. Bieler, D. Raabe, Acta Mater. 58 (2010) 1152.

[120] M. Liu, C. Lu, K.A. Tieu, TMS2014 Annu. Meet. Suppl. Proc. (2014) 317.

[121] O. Casals, J. Ocenasek, J. Alcala, Acta Mater. 55 (2007) 55.

[122] K.L. Johnson, K.L. Johnson, Contact Mechanics, Cambridge University Press, 1987.

[123] Y. Liu, S. Varghese, J. Ma, M. Yoshino, H. Lu, R. Komanduri, Int. J. Plast. 24 (2008) 1990.

[124] W.G. Mao, Y.G. Shen, C. Lu, J. Eur. Ceram. Soc. 31 (2011) 1865.

[125] G. Ghosh, M. Asta, J. Mater. Res. 20 (2005) 3102.

[126] Q.K. Zhang, J. Tan, Z.F. Zhang, J. Appl. Phys. 110 (2011) 014502.

[127] ABAQUS Manual, (2013).

[128] F. Ochoa, J.J. Williams, N. Chawla, J. Electron. Mater. 32 (2003) 1414.

[129] L. Jiang, N. Muthegowda, M.A. Bhatia, A. Migliori, K.N. Solanki, N. Chawla, Scr. Mater. 107 (2015) 26.

[130] S.F. Choudhury, L. Ladani, Metall. Mater. Trans. A 46 (2014) 1108.

[131] H. Chen, B. Yan, M. Yang, X. Ma, M. Li, Mater. Charact. 85 (2013) 64.

[132] P. Liu, A. Overson, D. Goyal, in:, 2015 IEEE 65th Electron. Components Technol. Conf., IEEE, 2015, pp. 99–105.

[133] B. Arfaei, N. Kim, E.J. Cotts, J. Electron. Mater. 41 (2012) 362.

[134] P. Liu, A. Overson, D. Goyal, in:, 2015 IEEE 65th Electron. Components Technol. Conf., IEEE, 2015, pp. 99–105.

[135] H.-T. Lee, S.-Y. Hu, T.-F. Hong, Y.-F. Chen, J. Electron. Mater. 37 (2008) 867.

[136] S. Choudhury, L. Ladani, J. Alloys Compd. In review (n.d.).

[137] F. Song, S.W.R. Lee, in:, 56th Electron. Components Technol. Conf. 2006, IEEE, 2006, pp. 1196–1203.

[138] J.-M. Kim, M.-H. Jeong, S. Yoo, C.-W. Lee, Y.-B. Park, Microelectron. Eng. 89 (2012) 55.

[139] T.R. Bieler, H. Jiang, L.P. Lehman, T. Kirkpatrick, E.J. Cotts, in:, 56th Electron. Components Technol. Conf. 2006, IEEE, 2006, pp. 1462–1467.

[140] S. Choudhury, L. Ladani, J. Alloys Compd. In review (n.d.).

[141] Q.K. Zhang, W.M. Long, Z.F. Zhang, J. Alloys Compd. 646 (2015) 405.

[142] S.W.O.N. Jeong, J.H. Kim, H.M.O. Lee, J. Electron. Mater. 33 (2004) 1530.

[143] X. Deng, G. Piotrowski, J.J. Williams, N. Chawla, J. Electron. Mater. 32 (2003) 1403.

[144] W.-L. Chiu, C.-M. Liu, Y.-S. Haung, C. Chen, Mater. Lett. 164 (2016) 5.

[145] L.C. Tsao, J. Alloys Compd. 509 (2011) 2326.

[146] L. Qu, H. Ma, H. Zhao, N. Zhao, A. Kunwar, M. Huang, in:, 2013 14th Int. Conf. Electron. Packag. Technol., IEEE, 2013, pp. 377–381.

[147] S.M.L. Nai, J. Wei, M. Gupta, J. Alloys Compd. 473 (2009) 100.

[148] M. Schaefer, R.A. Fournelle, J. Liang, J. Electron. Mater. 27 (1998) 1167.

[149] D.Q. Yu, L. Wang, J. Alloys Compd. 458 (2008) 542.

[150] R.A. Gagliano, M.E. Fine, J. Electron. Mater. 32 (2003) 1441.

[151] M.S. Park, M.K. Stephenson, C. Shannon, L.A. Cáceres Díaz, K.A. Hudspeth, S.L. Gibbons, J. Muñoz-Saldaña, R. Arróyave, Acta Mater. 60 (2012) 5125.

[152] J. Görlich, G. Schmitz, K.N. Tu, Appl. Phys. Lett. 86 (2005) 053106.

[153] T.-K. Lee, T.R. Bieler, C.-U. Kim, H. Ma, Fundamentals of Lead-Free Solder Interconnect Technology: From Microstructures to Reliability, Springer, 2014.

[154] G. Ghosh, J. Mater. Res. 19 (2004) 1439.

[155] Wen-Hwa Chen, Hsien-Chie Cheng, Ching-Feng Yu, in:, 2010 11th Int. Therm. Mech. Multi-Physics Simulation, Exp. Microelectron. Microsystems, IEEE, 2010, pp. 1–7.

[156] Y. Goh, A.S.M.A. Haseeb, H.L. Liew, M.F.M. Sabri, J. Mater. Sci. 50 (2015) 4258.

[157] C. Yang, F. Song, S.W.R. Lee, in:, 2011 IEEE 61st Electron. Components Technol. Conf., IEEE, 2011, pp. 971–978.

[158] F. Xing, J. Yao, J. Liang, X. Qiu, J. Alloys Compd. 649 (2015) 1053.

[159] S.M. Hayes, N. Chawla, D.R. Frear, Microelectron. Reliab. 49 (2009) 269.

[160] J.H.L. Pang, T.H. Low, B.S. Xiong, X. Luhua, C.C. Neo, Thin Solid Films 462-463 (2004) 370.

[161] H. Rhee, K.N. Subramanian, A. Lee, J.G. Lee, Solder. Surf. Mt. Technol. 15 (2003) 4.

[162] B. Talebanpour, Z. Huang, Z. Chen, I. Dutta, J. Electron. Mater. (2015).

[163] S.F. Choudhury, L. Ladani, J. Electron. Mater. Accepted (n.d.).

[164] P.J. McAllen, P. Phelan, J. Mater. Process. Technol. 155-156 (2004) 1214.

[165] D. Xie, S.B. Biggers, Finite Elem. Anal. Des. 42 (2006) 977.

[166] Y. Yao, L.M. Keer, M.E. Fine, Intermetallics 18 (2010) 1603.

[167] K.E. Yazzie, H.E. Fei, H. Jiang, N. Chawla, Acta Mater. 60 (2012) 4336.

[168] A.F.M. Yamin, N.M. Shaffiar, W.K. Loh, M.N. Tamin, in:, 35th Int. Electron. Manuf. Technol. Conf. Int. Electron. Manuf. Technol. Conf., 2012.

[169] C. Yang, S.W.R. Lee, in:, 2015 IEEE 65th Electron. Components Technol. Conf., IEEE, 2015, pp. 1029–1037.

[170] F. Song, S.W.R. Lee, K. Newman, B. Sykes, S. Clark, in:, 2007 Proc. 57th Electron. Components Technol. Conf., IEEE, 2007, pp. 1504–1513.

[171] L.J. Ladani, J. Razmi, IEEE Trans. Device Mater. Reliab. 9 (2009) 348.

[172] N.J. Chhanda, J.C. Suhling, P. Lall, in:, 13th Intersoc. Conf. Therm. Thermomechanical Phenom. Electron. Syst., IEEE, 2012, pp. 269–281.

[173] L.J. Ladani, Microelectron. Eng. 87 (2010) 208.

[174] S. Yi, P.D. Daharwal, Y.J. Lee, B.R. Harkness, I. Corporation, D. Corning, in:, Electron. Components Technol. Conf. IEEE, 2006, pp. 939–945.

[175] E. Vandevelde, B., Okoro, C., Gonzalez, M., Swinnen, B., Beyne, in:, Ninth Int. Conf. Therm. Mech. Multiphysics Simul. Exp. Micro-Electronics Micro-Systems, EuroSimE, Germany, 2008.

[176] H. Ma, J. Mater. Sci. 44 (2009) 3841.

[177] L.J. Ladani, A. Dasgupta, in:, Electron. Photonic Packag. Electr. Syst. Des. Photonics, Nanotechnol., ASME, 2005, pp. 57–63.

[178] L.J. Ladani, A. Dasgupta, J. Electron. Packag. 130 (2008) 011008.

[179] J.H.L. Pang, A. Yeo, T.H. Low, F.X. Che, in:, Ninth Intersoc. Conf. Therm. Thermomechanical Phenom. Electron. Syst. (IEEE Cat. No.04CH37543), IEEE, 2004, pp. 160–164.

[180] K.A. Brakke, Exp. Math. 1 (1992) 141.

[181] I. Kaban, S. Mhiaoui, W. Hoyer, J.-G. Gasser, J. Phys. Condens. Matter 17 (2005) 7867.

[182] L.J. Ladani, A. Dasgupta, in:, 7th. Int. Conf. Therm. Mech. Multiphysics Simul. Exp. Micro-Electronics Micro-Systems, IEEE, 2006, pp. 1–6.

[183] L.J. Ladani, J. Electron. Packag. 132 (2010) 041011.

[184] C.-C. Lee, K.-S. Kao, R.-S. Cheng, C.-J. Zhan, T.-C. Chang, Microelectron. Eng. 120 (2014) 138.

[185] L.J. Ladani, Microelectron. Eng. 87 (2010) 1852.

[186] S. Ridout, C. Bailey, Fatigue Fract. Eng. Mater. Struct. 30 (2007) 400.

[187] R.R. Tummala, P.M. Raj, A. Aggarwal, G. Mehrotra, S. Bansal, C.K. Ong, J. Chew, K. Vaidyanathan, in:, 56th Electron. Components Technol. Conf. 2006, IEEE, 2006, pp. 102–111.

[188] M. Prabhu, A., Barkar, D., Pecht, ASME Adv. Electron. Packag. 10 (1995) 187.

[189] S.H. Lau, John H., Pan, Int. J. Microcircuits Electron. Packag. 24 (2001) 11.